UNIVERSITAT POLITÈCNICA DE CATALUNYA BARCELONATECH

Fast simulation : assisted shape correction after machining

by

Ramiro Francisco Mena Andrade

École Centrale de Nantes
Nantes, France

Universitat Politècnica de Catalunya
Barcelona, Spain

P H D T H E S I S

Fast Simulation – Assisted Shape Correction after Machining

Dissertation presented in partial fulfilment of the requirements for the degree of

PhD of the Universitat Politècnica de Catalunya
Doctor de la Universitat Politècnica de Catalunya

PhD of the École Centrale de Nantes
Docteur de l'École Centrale de Nantes

by
Ramiro Francisco MENA ANDRADE

February 2021

President:	Pedro DIEZ	Universitat Politècnica de Catalunya
Jury members:	Elías CUETO	Universidad de Zaragoza
	Philippe CRESTA	Airbus SAS
	Pierre JOYOT	Université de Bordeaux
	Katia MOCELLIN	Mines ParisTech-PSL
Main Advisor:	Antonio HUERTA	Universitat Politècnica de Catalunya Co-
Co-Advisor:	José Vicente AGUADO	École Centrale de Nantes
Industrial Advisor:	Stéphane GUINARD	Airbus SAS

The man who cannot occasionally imagine events and conditions of existence that are contrary to the casual principle as he knows it will never enrich his science by the addition of a new idea. -Max Plank

To my parents, Rosita and Manuel.

Contents

Abstract 1

Résumé 3

1 Distortions in Large Aluminum Forgings: state-of-the-art 5

1.1 Introduction . . . 6
1.2 Distortion in the aeronautical industry: an open problem . . . 7
1.3 Residual Stresses, Distortion and Reshaping . . . 9
1.4 Post-machining distortion mitigation techniques . . . 10
1.5 Reshaping simulation: challenges and perspectives . . . 13
1.6 Conclusions . . . 16

2 Residual stresses: selected numerical models 17

2.1 Introduction . . . 18
2.2 Numerical models description and validation . . . 19
2.2.1 Quenching simulation for residual stress prediction . . . 19
2.2.1.1 Thermo-plasticity modelling . . . 20
2.2.1.2 Application to a rolled plate . . . 20
2.2.1.3 Validation of the residual stress prediction . . . 22
2.2.2 Bending straightening simulation . . . 24
2.2.2.1 Elasto-plasticity modelling . . . 24
2.2.2.2 Application to a four-point bending setup . . . 25
2.2.2.3 Validation of the bending straightening model . . . 27
2.3 Conclusions . . . 27

3 Reshaping diagrams for bending straightening **29**
3.1 Introduction . . . 31
3.2 Numerical study of forged parts . . . 32
3.2.1 Residual stress after quenching . . . 33
3.2.2 Residual stresses after machining . . . 34
3.2.3 Reshaping diagrams for bending straightening . . . 37
3.2.4 Parametric study of the reshaping diagram . . . 39
3.3 Residual stress free diagrams for simulation-assisted reshaping . . . 41
3.3.1 Linear unloading path in the force-displacement diagram . . . 43
3.3.2 Reshaping offset calibration . . . 46
3.4 Conclusions . . . 48

4 Bending straightening: a multiparametric ROM study **51**
4.1 Introduction . . . 53
4.2 A brief state-of-the-art on model order reduction . . . 54
4.2.1 The need of model order reduction . . . 54
4.2.2 Fundamentals of model order reduction . . . 55
4.2.2.1 Classification of MOR . . . 57
4.2.3 Selected MOR techniques . . . 59
4.2.3.1 Proper Orthogonal Decomposition . . . 59
4.2.3.2 Reduced Basis . . . 60
4.2.3.3 Proper Generalized Decomposition . . . 63
4.2.3.4 Discrete Empirical Interpolation Method . . . 66
4.2.3.5 Sparse Subspace Learning (SSL) . . . 67
4.2.4 MOR applied to manufacturing problems . . . 69
4.3 Multi-parametric bending straightening . . . 71
4.3.1 Process model and parameters . . . 72
4.3.2 Reshaping under the SSL formulation . . . 74
4.3.3 Problem setup . . . 74
4.4 Results and discussion . . . 76
4.5 Conclusions . . . 80

5 Evaluation of multiple reshaping operations via MOR **83**
5.1 Introduction . . . 85
5.2 Multiple bending straightening operations . . . 85

5.2.1 Problem setup . . . 85
5.3 Reference solution: RS for multiple operations . . . 87
5.3.1 First step . . . 87
5.3.2 Second step . . . 88
5.4 Proposed approach: RSF hypothesis for multiple operations . . . 89
5.4.1 First step . . . 90
5.4.2 Second step . . . 90
5.5 Reshaping as a root-finding problem . . . 95
5.5.1 First step: Error estimation . . . 96
5.5.2 Second step: Error estimation . . . 96
5.6 Process signature . . . 98
5.7 Conclusions . . . 100

Conclusions and perspectives **103**

Bibliography **107**

A Publications **121**
A.1 Journals articles . . . 121
A.2 Books chapters . . . 121
A.3 Conference proceedings . . . 122
A.4 Technical reports . . . 122
A.5 Outreach activities . . . 122

Table of figures

1.1 Example of aluminium forgings subjected to distortion: cruciform beams of the Airbus' A320 wing box, highlighted in red. 7
1.2 Interaction between Residual Stresses, Distortion and Reshaping. . . 8
1.3 Principal types of distortion after machining in a simplified version of the Airbus' A320 cruciform beam. Adapted from [65]. 9
1.4 Reshaping operations used at Airbus: (a) Bending, (b) Torsion, (c) Roller burnishing and (d) Ultrasonic needle peening. 11
1.5 Residual stress process signature after unloading: (a) Bending, (b) Torsion, (c) Roller burnishing and (d) Ultrasonic needle peening. Adapted from [3, 43] 13
1.6 Reshaping simulation workflow diagram 14
1.7 Example of distortion in a cruciform. (a) Geometry before and after machining. (b) Simulation vs measurements results. Adapted from [19]. 15

2.1 Residual stresses simulation by using the sequential approach (*not included and **included but not simulated). 19
2.2 Left: plate geometry with indication of the modelled portion. Center: in red, boundaries to which a mixed-type boundary condition is applied (adiabatic conditions applied on the symmetry planes). Right: detail of the mesh. 22
2.3 Quenching simulation results at the center of the plate ($x = L/2$, $y = LT/2$): (a) Temperature evolution as a function of time; (b) Longitudinal residual stresses σ_{11} along the thickness (short transverse direction) and validated against results from [78]. 23

2.4 Simulation results: 3D residual stress field in a rolled plate after quenching. 24
2.5 Four-point bending experiment for the validation of the bending straightening model 26
2.6 Validation of the bending straightening simulation model via strain versus force measures: comparison of the simulation results (dashed line) and the experimental measures (solid line) for two specimens labelled L1 and L2. (a) Comparison for strain gauge J1 (located at top) and (b) Comparison for strain gauge J2 (located at bottom). . . 28

3.1 Reshaping simulation: sequential vs proposed approach (*not included and **included but not simulated). 32
3.2 Reference geometry for the simulation of bending straightening of forged parts: a beam with T-shaped cross section 33
3.3 Temperature evolution in the T-shaped beam (bulk) during the first 10 seconds of simulation at the (1) wing, (2) rib and (3) fillet. The cross section corresponds to the symmetry plane $z = 0$ and the subscripts s and i refer to the surface and internal points. 34
3.4 Residual stress distribution in the T-shaped beam: (a) after quenching (bulk), (b) after machining with $M_o = 10$ mm (case A) and (c) after machining with $M_o = 5$ mm (case B). All the snapshots are taken in the symmetry plane $z = 0$ and presented in the undeformed configuration. 35
3.5 T shaped beam model. (a) Distortion after machining as a function of machining offset M_o. (b) Distorted shape for case A ($M_o = 10$ mm) and case B ($M_o = 5$ mm). 37
3.6 Reshaping diagram (scheme). (a) The three characteristic regions of the reshaping diagram: elastic area of no repair (A), repairing area (B) and inversion area (C). (b) Shape after reshaping for values of the stroke in each reshaping region. 38
3.7 Parametric study of the reshaping diagrams for six combinations of machining offset and the rollers positioning (values given in Figure 3.2b): (a) $M_o = 10$ mm (case A) and three rollers positioning. (b) $M_o = 5$ mm (case B) and three rollers positioning. 40

3.8 Residual stress free reshaping diagrams (dashed line) against *true* reshaping diagrams that account for full 3D residual stress field (solid line), for six different reshaping configurations. 42

3.9 Testing the linear unloading hypothesis. Force versus displacement diagram for the rectangular rolled plate (specimen L2). Experimental curves (solid lines) vs linear unloading path (dashed lines). (a) At midspan $L = 100$ mm and (b) At the section where the load is applied $L = 70$ mm (see Figure 2.5a). 44

3.10 T shaped beam. Force vs displacement diagram: numerical curves (solid lines) vs linear unloading path (grey dashed lines). (a) Reshaping configuration P1 (RS) and (b) Reshaping configuration P5 (RS). 45

3.11 T shaped beam. Remaining distortion vs Stroke diagram: Offset calculation. (a) Reshaping configuration P1 and (b) Reshaping configuration P5. 47

3.12 T shaped beam. Reshaping diagram: optimal final distortion $\delta(y_s^{opt,RS})$ vs obtained final distortion $\delta(y_s^{opt})$. (a) Reshaping configuration P1 and (b) Reshaping configuration P5. 49

4.1 Computational cost comparison between FOM and ROM. Adapted from [49, 92] 58

4.2 Projection based Model Order Reduction applied to linear (a) and non-linear (b) problems. Adapted from [13] 61

4.3 The Proper Generalized Decomposition: (a) Original problem, (b) Separated representation and (c) Fixed-point algorithm scheme. . . . 64

4.4 Bending straightening. a) Process model and b) process simulation. Adapted from [50]. 73

4.5 T shaped beam. a) Geometry definition and b) Parameters representation for three-point bending straightening. 75

4.6 Parametrization of initial distortion δ_0 as a function of fictitious moment M. 76

4.7 Exploration of the parametric space for a hierarchy level $k = 3$. a) Full sampling ($9^3 = 729$ points) vs b) Sparse sampling (123 points). . 78

4.8 First 8 shapshots of the displacement field $\boldsymbol{u}(\boldsymbol{x};\boldsymbol{\mu})$. From left to right $\delta_0 = [-15, 0]$. From top to bottom the pair (y_s, r_e) are (5, 100), (5, 485), (30, 100) and (30, 485), respectively. 79
4.9 Response surface: Remaining distortion δ. Solution selection as a function of r_e. a) $r_e = 200$(mm) and b) $r_e = 485$(mm). 81
4.10 GUI for results' visualization: 1) Parameters selection, 2) Beam's geometry after unloading, 3) Reshaping diagram generation, 4) Page selection of the solution dictionary, 5) Reset button 82

5.1 T shaped beam. a) Cross section geometry and b) Reshaping set-up 86
5.2 Multiple bending straightening operations: first step. Left) Reconstruction of the displacement field u_2. Right) Reshaping diagram for different criteria. 91
5.3 Multiple bending straightening operations: second step (symmetric configuration). Left) Reconstruction of the displacement field u_2. Right) Reshaping diagram for different criteria. 92
5.4 Multiple bending straightening operations: second step (non-symmetric configuration). Left) Reconstruction of the displacement field u_2. Right) Reshaping diagram for different criteria. 93
5.5 Reshaping diagram for consecutive reshaping steps: comparison between the curves with RS and under the RSF hypothesis. 94
5.6 Multiple bending straightening operations: error estimation. 97
5.7 Process signature's scheme for bending straightening: comparison between a generic distorted geometry against the available imposed displacement. 99
5.8 Theoretical process signature for bending straightening applied to two complete reshaping steps. (a) Normalized remaining distortion δ_i. (b) Normalized imposed vertical displacement u_2. 101
5.9 Distortion evolution during reshaping (simulation results). (a) Remaining distortion δ_i. (b) Imposed vertical displacement u_2 for each reshaping step. 102
5.10 Model Order Reduction strategies for reshaping. a) Sequential model (implemented) and b) Feedback model (future work). 102

List of Tables

2.1 Thermo-plasticity model for quenching simulation. 21
2.2 Quenching model validation. Quenching process conditions from [52]. 22
2.3 Elasto-plastic model with kinematic hardening for bending straightening simulation 25
2.4 Chaboche's material model parameters for AA7010 [36]. All units are in MPa except for ν, b and γ_i which are dimensionless. 26

3.1 Final displacement for a given stroke y_s during reshaping configurations P1 and P5: comparison between the non-linear (FEM) and linear unloading path (LU). 44
3.2 Calculation of the offset Δy_s and error estimation for the applied stroke y_s^{opt}. 47
3.3 Distortion reduction and error estimation after reshaping. 49

4.1 Bending straightening process model: inputs, parameters and outputs. Adapted from [50, 112] 73
4.2 Parameters values for the three-point bending operation 75

5.1 Reshaping simulation set-up 87
5.2 Rollers positions during multiple reshaping steps 87
5.3 Error estimation set-up for the second reshaping step 97
5.4 Required operations as a function of waves number n 100

Abstract

Computer simulation is acknowledged as the third branch of Science. From the seminal work of Turner et al. (1956) [111] on Finite Elements, impressive improvements have been made in terms of software and hardware, so that, nowadays, there is no engineering device (in the broad sense of the word) that is not subjected to any kind of simulation. However, in the same way as there is a gap between theory and practice, at an industrial level there are still problems where, at the moment, numerical simulations are not used and instead, a hand-craft approach is applied. The mitigation of distortion in large aluminium forgings is one of these problems.

Post-machining distortion is an open problem that affects every single large thick-walled aluminium forging assembled on an aircraft. The origin of distortion is the presence of residual stresses (RS) developed along the manufacturing chain, especially after the heat treatment of quenching. When machining takes places, it causes a redistribution at an internal level as the previous equilibrium state is broken by the material removal action. At a theoretical level, if the RS in a part are known in advance, a proper machining sequence could be planned with the aim to mitigate or counteract a warped geometry. This strategy is already implemented for parts machined from rolled plates, where RS can be considered as constant along the longitudinal direction [38]. However, for forgings, RS are a function of the geometry and, as a result, a complex three-dimensional stress field is present. Important research efforts are done in order to predict RS numerically for forgings but still, the deterministic nature of numerical simulations are not able to capture the variable behaviour of distortions. At the moment, the current research direction looks at the distortion problem as something to avoid upwards in the manufacturing chain, it means, focusing the efforts in the steps before or during machining at latest. In the present thesis, we opted to follow the opposite direction, which means, how to proceed and handle distortion once it has arisen. To perform this task, the problem was

first studied by conventional Finite Element Method (FEM), and then, by applying a non-intrusive Model Order Reduction (ROM) technique called Sparse Subspace Learning (SSL) [14].

The content of this thesis is structured as follows. In chapter 1 we introduce the distortion problem, followed by the definition and interconnection of the three main actors: residual stresses, distortion and reshaping. Then, a review of the available reshaping techniques is provided and finally, the challenges and perspectives for reshaping simulation are discussed. Chapter 2 presents two numerical models devoted to determine the residual stresses after quenching and plastic bending, respectively as the heat treatment is considered as the main source of residual stresses in aluminium forgings and the latter corresponds to the selected reshaping operation to be studied in this thesis. After its validation, both models are applied in the following chapters and they provide the reference solution to our problem. In chapter 3, we introduce the *reshaping diagrams* as a tool to assist the bending straightening operation. In addition, the *residual stress free* hypothesis is presented as an alternative to study the reshaping problem. This approach uses the distorted geometry as the main input to simulate the reshaping step by considering the part without residual stresses. Then, in chapter 4, a multiparametric study of bending straightening is provided with the aid of the SSL, so that the reshaping diagrams can be generalized for a previously defined set of parameters. Finally, as reshaping is an iterative and sequential procedure, in chapter 5, two consecutive bending straightening operations are simulated. Different reshaping strategies are studied and a methodology is provided to tackle in a more systematic way the open problem of reshaping.

Résumé

La simulation numérique est reconnue comme étant la troisième branche de la science. À partir des travaux fondateurs de Turner et al. (1956) [111] sur les éléments finis, des améliorations impressionnantes ont été apportées en termes de software et de hardware, de sorte qu'aujourd'hui, il n'existe plus aucun dispositif d'ingénierie (au sens large du terme) qui ne soit pas transcrit par une quelconque simulation. Cependant, tout comme il existe un fossé entre théorie et pratique, il existe encore des problèmes au niveau industriel où, pour le moment, les simulations numériques n'ont pas encore pris la place des approches artisanales. L'atténuation de la distorsion dans les grandes pièces forgées en aluminium est l'un des exemples.

La distorsion post-usinage est un problème ouvert qui affecte chaque grande pièce forgée en aluminium à paroi épaisse assemblée sur un avion. Cette distorsion provient de la présence de contraintes résiduelles (RS) développées tout au long de la chaîne de fabrication, en particulier après traitement thermique par trempe. Lorsque l'usinage a lieu, il provoque une redistribution à un niveau interne car l'état d'équilibre précédent est rompu par l'action d'enlèvement de matière. Au niveau théorique, si les RS d'une pièce sont connues à l'avance, une séquence d'usinage appropriée pourrait être planifiée dans le but d'atténuer ou de contrecarrer une géométrie déformée. Cette stratégie est déjà mise en œuvre pour les pièces usinées à partir de tôles laminées, où la RS peut être considérée comme constante dans la direction longitudinale [38]. Cependant, pour les pièces forgées, les RS sont fonction de la géométrie et, par conséquent, un champ de contrainte tridimensionnel complexe est présent. D'importants efforts de recherche sont réalisés afin de prédire numériquement les RS pour les pièces forgées, mais la nature déterministe des simulations numériques ne permet toujours pas de saisir le comportement variable des déformations. Pour l'instant, l'orientation actuelle de la recherche considère le problème des distorsions comme quelque chose à éviter depuis le début de la chaîne

de fabrication, c'est-à-dire en concentrant les efforts dans les étapes précédentes, oú au plus tard pendant l'usinage. Dans la présente thèse, nous avons choisi de suivre la direction opposée, c'est-à-dire comment procéder et gérer la distorsion une fois qu'elle est apparue. Pour réaliser cette tâche, le problème a d'abord été étudié par la méthode classique des éléments finis (FEM), et par la suite en appliquant une technique non intrusive de réduction de l'ordre des modèles (ROM) appelée "Sparse Subspace Learning" (SSL) [14].

Le contenu de cette thèse est structuré comme suit. Dans le chapitre 1 le problème de la distorsion sera introduit, suivi de la définition et de l'interconnexion des trois acteurs principaux : les contraintes résiduelles, la distorsion et le redressage. Les techniques de redressage seront ensuite passées en revue pour finalement examiner les défis et les perspectives de la simulation du redressage. Le chapitre 2 présente deux modèles numériques consacrés à la détermination des contraintes résiduelles après la trempe et le pliage plastique, le traitement thermique étant considéré comme la principale source de contraintes résiduelles dans les pièces forgées en aluminium. C'est dans ce cadre (origine majoritairement thermique des contraintes résiduelles) que sera étudiée l'opération de redressage sélectionnée dans cette thèse. Après leurs validations, les deux modèles sont appliqués dans les chapitres suivants où ils constitueront la solution de référence du problème. Dans le chapitre 3, les *diagrammes de mise en forme* sont présentés comme un outil d'aide à l'opération de redressement par flexion. En outre, l'hypothèse *reste sans contrainte résiduelle* est présentée comme une alternative pour étudier le problème de redressage. Cette approche utilise la géométrie déformée comme entrée principale permettant de simuler l'étape de redressage en considérant la pièce sans contraintes résiduelles. Le chapitre 4 montrera une étude multiparamétrique du redressement par flexion à l'aide du SSL. Les diagrammes de redressage seront généralisés pour un ensemble de paramètres préalablement définis. Le redressage étant une procédure itérative et séquentielle, le chapitre 5 explicitera la simulation de deux opérations consécutives de redressement par flexion. Différentes stratégies de redressage seront étudiées, et une méthodologie sera fournie pour aborder de manière plus systématique le problème ouvert du redressage.

Chapter 1

Distortions in Large Aluminum Forgings: state-of-the-art

Distortions after machining of large aluminum forgings are a recurrent problem for the aeronautical industry. These deviations from design geometry are caused by the presence of residual stresses, which are developed along the manufacturing chain. To solve this problem, a series of post-machining operations called *reshaping* are required. Despite reshaping manages to restore the correct geometry, it is highly manual and time-consuming, therefore, there is a need at an industrial level to use numerical simulation to study reshaping. The present chapter describes the problem of distortion, the operations required to mitigate these geometrical defects and the challenges associated to simulate reshaping.

Contents

1.1 Introduction 6
1.2 Distortion in the aeronautical industry: an open problem 7
1.3 Residual Stresses, Distortion and Reshaping 9
1.4 Post-machining distortion mitigation techniques 10
1.5 Reshaping simulation: challenges and perspectives . . . 13
1.6 Conclusions 16

1.1 Introduction

Large and thick-walled aluminum forgings are widely used in the aeronautical industry. The key material properties as a great strength-to-weight ratio and good formability in combination with the manufacturing process allow producing complex shapes in an economical way [53]. Additionally, when compared to other metal working processes (e.g extensive machining, welding or casting), improved material properties as grain size and orientation are obtained [69]. However, aluminum forgings show important distortions after machining due to the presence of residual stresses which are a consequence of the non-homogeneous plastic strains developed along the manufacturing chain, especially after the heat treatment of quenching [62, 87].

Such distortions are variable in nature, but the industrial process incorporates a robust post-machining stage called *reshaping*. Particularly, skilled boilermakers operate a sequence of mechanical loadings on the non-conforming part and re-establish its nominal geometry while obeying guidelines imposed by stress offices - which guarantees the produced part has still mechanical characteristics compatible with its operational role -. An example of the structural parts subjected to reshaping are the cruciform beams, located at the wing-box in an aircraft and highlighted in red in Figure 1.1. On the other hand, reshaping is a highly manual and collaborative process as multiple operators are involved to repair one single part. At the same time, the process fully depends on the experience of the boilermakers and repairing each structural part in a tailor-made manner is time-consuming. Therefore, there is a strong demand from the industry to derive operational assistance from capabilities offered by numerical simulation tools [102].

When mitigating distortion via reshaping, numerical simulations may offer huge margins for improvements such as operational assistance to boilermakers and related gains in time-cycle (optimized reshaping sequence, optimized parameters for each elementary reshaping operation), improved knowledge of actual part and related gains in safety (monitoring of actual plastic strains). However, some research efforts are required in order to migrate from the actual heuristic repairing method to a simulation-assisted operation, as reshaping simulations present challenges to be solved as the elevated computational cost of each simulation or the use of static data of traditional Finite Element Analysis (FEA), to name a few.

This chapter describes the distortions on aluminum forgings, the operations re-

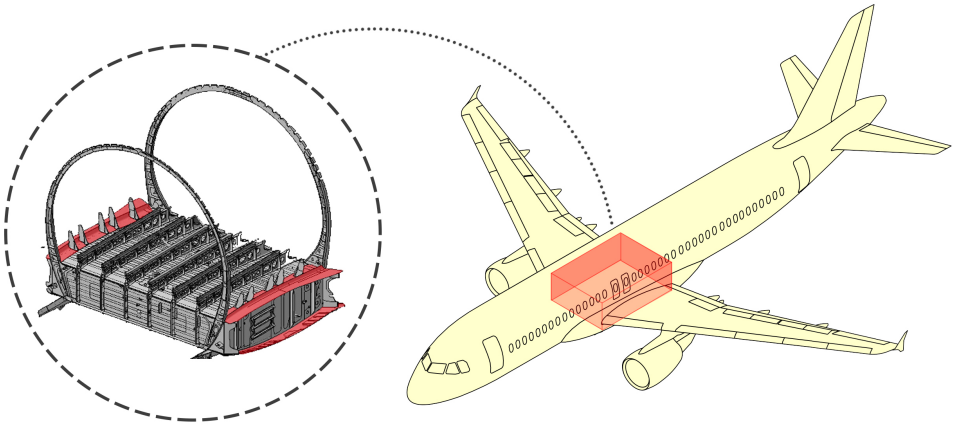

Figure 1.1: Example of aluminium forgings subjected to distortion: cruciform beams of the Airbus' A320 wing box, highlighted in red.

quired to solve this problem and the challenges associated with deploying numerical simulations at workshop level and actually help operators. The document is structured as follows: section 1.2 provides an overview of distortions as an open problem for the aeronautical industry. Then, the relation between residual stresses, distortions, and reshaping are explained in section 1.3. Next, the different reshaping operations are described in detail in section 1.4 and the challenges and perspectives to simulate reshaping are reviewed in section 1.5. Finally, in section 1.6, the obtained conclusions are presented.

1.2 Distortion in the aeronautical industry: an open problem

To the best of our knowledge, the problem of distortions in the aeronautical industry was first reported during World War II, when some difficulties were experienced with extrusions used for aircraft spars parts [43]. Then, due to the technology transfer performed after the war, the use of large forgings for light metals alloys (i.e magnesium and aluminum) was potentiated with governmental initiatives as the Air Force Heavy Press Program in the United States, which allowed the construction of forgings up to 50k tons capacity[1] [6]. Thanks to this new range of tools, the

[1]Nowadays, the biggest forging has a capacity of 80k ton and is located in China [39].

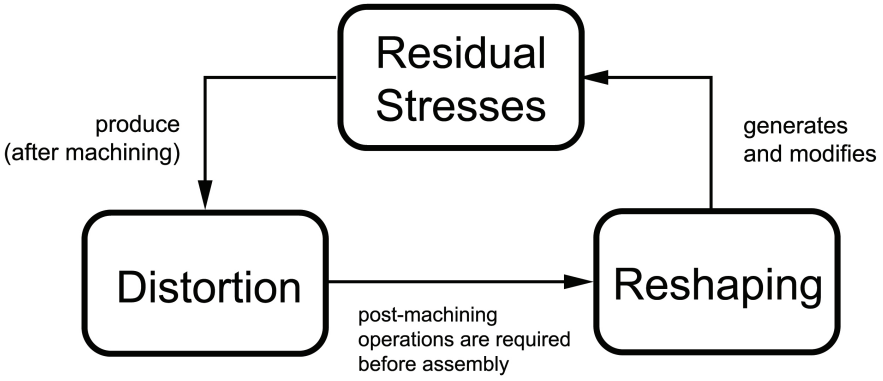

Figure 1.2: Interaction between Residual Stresses, Distortion and Reshaping.

unitization[2] of structural parts was feasible and acted as a driving force for the development of bigger aircraft with important manufacturing costs savings [8, 105]. On the other hand, as the forgings grew in size and with them their cross sections and wall thickness, the range of residual stresses developed after quenching experienced an increment too, so as the research interest to predict the residual stresses and any future distortion after machining [52, 88].

At an industrial level, different attempts have been made to minimize distortion along the manufacturing chain of heat-treated aluminum alloys components. In North America, the MAI (Metals Affordability Initiative) program [8, 62] and in Europe, the COMPACT (A COncurrent approach to Manufacturing induced Part distortion in Aerospace ComponenTs) project [87, 102, 103], focused on the understanding of residual stress and part distortion. However, both initiatives efforts were concentrated on the upstream manufacturing processes, such as quenching, stress relief, ageing, and machining, letting reshaping unattended and as a byproduct. Theoretically, if distortion is controlled or minimized, then reshaping is unnecessary. Unfortunately, a part with minimized distortions is only achieved in exceptional cases [67]. Therefore, we can state that distortion is an open problem for the industry during the last 80 years.

[2] Action to replace composite structures to single components

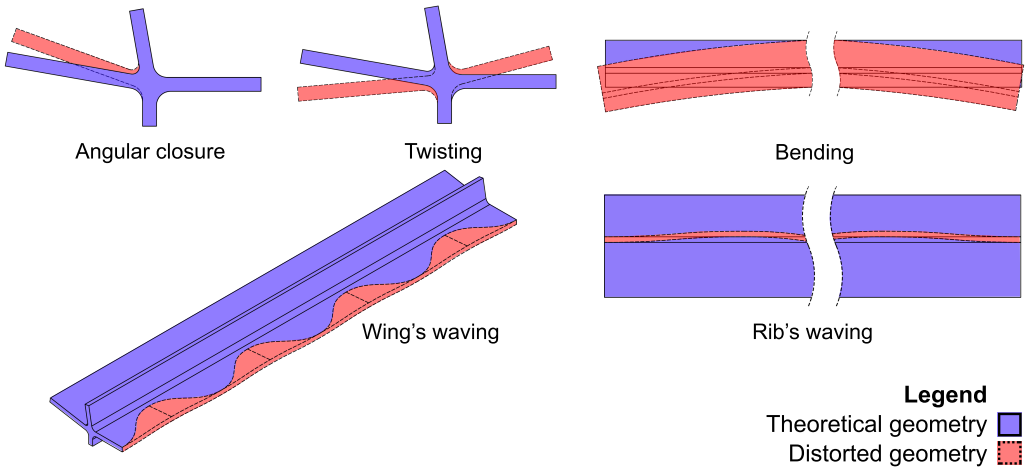

Figure 1.3: Principal types of distortion after machining in a simplified version of the Airbus' A320 cruciform beam. Adapted from [65].

1.3 Residual Stresses, Distortion and Reshaping

In the distortion mitigation problem, there are three main actors: residual stresses, distortion, and reshaping. They can be considered as the source, the problem, and the current solution, respectively. The three phenomena are coupled and mutually influence each other, as represented in Figure 1.2. In the following section, a definition for each actor is provided.

Residual stresses refer to any stress distribution, which is present in a solid in the absence of an external load or thermal gradient [95]. In a material, the residual stress distribution is a direct consequence of non-homogeneous plastic deformations arising from transformations endured during the manufacturing process. Based on its characteristic length scale, residual stresses are classified as type I, II and III, corresponding to macro stresses, intergranular stresses, and stresses at an atomic scale, respectively [114]. For distortion generation/mitigation, only residual stresses of type I are considered as this scale includes the stresses along the cross-section. This type of stresses can be induced by thermal or mechanical loading (e.g. welding and/or ultrasonic shoot penning).

Sim [102] defines distortion after machining as the shape deviation respect to the design geometry once the part is released from the fixture clamps. This problem is not caused by machining tolerance, over/under machining or dimensional inaccuracy.

In a general way, distortion can be classified in two categories: in-plane and out-of-plane. Nevertheless, more complex patterns are present in forgings parts. Marin [65] documented the principal types of distortions present on a cruciform as shown in Figure 1.3, where each type of distortion is represented in an isolated way. However, in a real part, all five types of distortions are combined simultaneously with the additional challenge that every time a new part is machined, a different magnitude of distortion is obtained.

Reshaping can be defined as the post-machining operations required to mitigate distortion. The general idea is to induce distortion on the contrary direction of the actual warped geometry to counteract the geometrical defect and restore the design geometry within a given tolerance. To perform this task, the material must be taken to the plastic regimen with the aim to induce plastic strains in the part. A detailed description of the reshaping operations is provided in the next section.

Now that the main actors are defined, it is easier to explain the whole picture of distortion. First, residual stresses appear after quenching. This heat treatment is the main source of residual stresses as the core of the part and its surface are subjected to different and strong thermal gradients. As a consequence, once the part reaches the room temperature, there is a bi-axial compression stress distribution at the surface which is counterbalanced by a three-dimensional tension state in the core [87]. However, its internal distribution evolves each time a new operation is performed in the manufacturing chain. After quenching, the part undergoes additional manufacturing stages: a stress relief process, followed by a second heat treatment called ageing, both processes aiming at minimizing residual stresses before machining. Then, during machining, the material removal breaks the equilibrium state of the current residual stresses, producing a redistribution of residual stresses. As a consequence, distortion appears. Next, each time reshaping is applied, new residual stresses are introduced to the part until the theoretical geometry is restored within the design's tolerance.

1.4 Post-machining distortion mitigation techniques

Since distortions are present after machining, it is mandatory to remove the geometrical deviations before proceeding to the assembly stage. In that way, the installation of the structural part into the corresponding sub-component is easier and the addi-

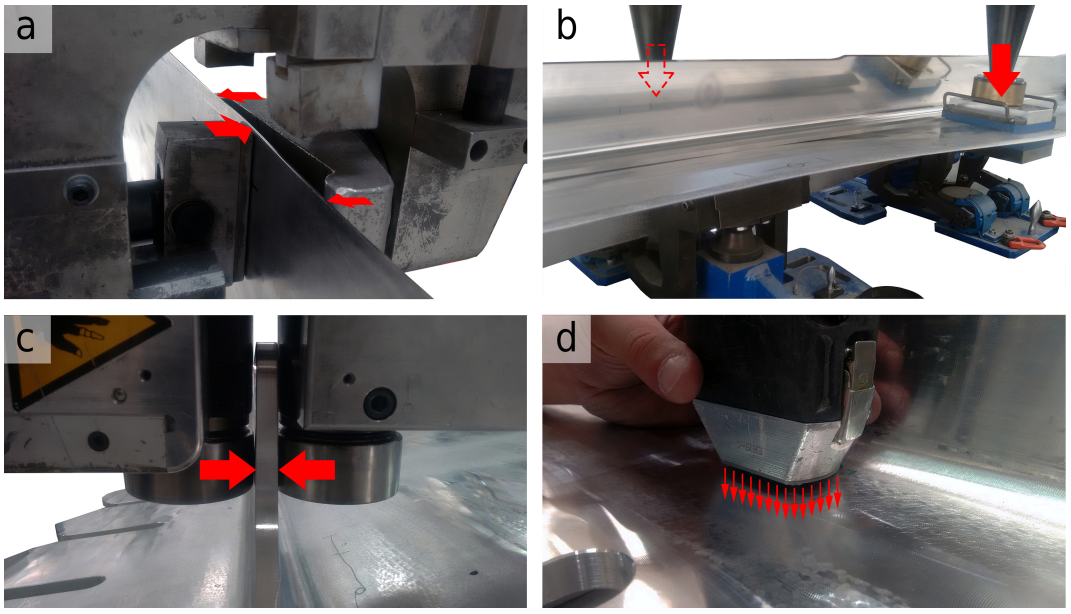

Figure 1.4: Reshaping operations used at Airbus: (a) Bending, (b) Torsion, (c) Roller burnishing and (d) Ultrasonic needle peening.

tion of excessive stresses due to adjustment into the system is avoided. To perform this task, there are four reshaping operations available: bending straightening, torsion straightening, roller burnishing, and ultrasonic needle peening, as shown in Figure 1.4.

Bending straightening is an elastic-plastic operation. Depending on the part's geometry and dimensions, it can be used to remove globally a longitudinal distortion or locally the wing's waving (see Figure 1.3). After unloading, the residual stresses along the cross-section present the so-called three zero-crossing distribution, as depicted in Figure 1.5a. From a material science point of view, bending straightening and its non-homogeneous deformation produces a rearrangement of existing residual stresses [41], causes non-homogeneous material properties, anisotropy of strength and Bauschinger effect [97].

Similar to the previous process, torsion straightening is an elastic-plastic operation too. For simple cylindrical geometries, after unloading, the residual stresses present the so-called three zero-crossing distribution, as depicted on Figure 1.5b but instead of the compression-tension stresses generated during bending, shear stresses are produced. For more complex geometries as rectangular or I sections, the mem-

brane analogy can be used [108] and it is reported that the plastic range is obtained first at the round fillets for I beams [28, 75]. This operation is used to correct any twisting distortion and as its bending counterpart, suffers from the presence of springback during unloading which has to be taken into account.

Roller burnishing is a surface finishing method that induces a plastic deformation under cold working conditions by applying pressure through a cylindrical tool [68]. In the context of reshaping, it is used to modify the distribution of residual stresses by inducing a local compressive residual stress at the surface and for our specific case, two rollers are used, as shown in Figure 1.4c. This configuration produces a symmetric residual stress distribution as depicted in Figure 1.5c. By applying this method, surface irregularities are removed. As a consequence, a smooth and shiny surface with better fatigue strength is obtained [3]. The depth of the work-hardening layer depends on the process parameters and material, but in general, it is small and varies between 0.2-1 mm [30, 68].

Ultrasonic needle peening is a special case of shot peening. Here, instead of using the traditional spheres to hit the part and induce compressive residual stresses at the surface of the component, oscillating cylindrical bars in the ultrasonic range (over 18 kHz) are employed [116]. This operation stretches plastically the area where it is applied and, in order to counterbalance this effect, it produces an S-shape residual stress profile starting with a compressive layer followed by a tension zone underneath, as represented in Figure 1.5d [95]. The method is manual, fast and easy to apply, as the tool can be easily handled by the operator. On the other hand, the area of influence of the residual stresses is smaller respect to the cross-section and usually, it is applied to a single side of the part, giving as a result an asymmetric residual stress distribution.

The corrective stage of reshaping is an iterative operation and its work-flow diagram is represented in Figure 1.6. Starting from the initial geometry, a measurement and control step is performed in order to determine the level of distortion. Based on the result, one of the four reshaping operations described before is selected. To perform one single plastic deformation step, the selected reshaping operation needs to be configured, it means, the technological parameters $\boldsymbol{\mu_i}$ (e.g position, imposed displacement, length of the application) need to be defined. This process is repeated until the part is repaired and fits into the design tolerance.

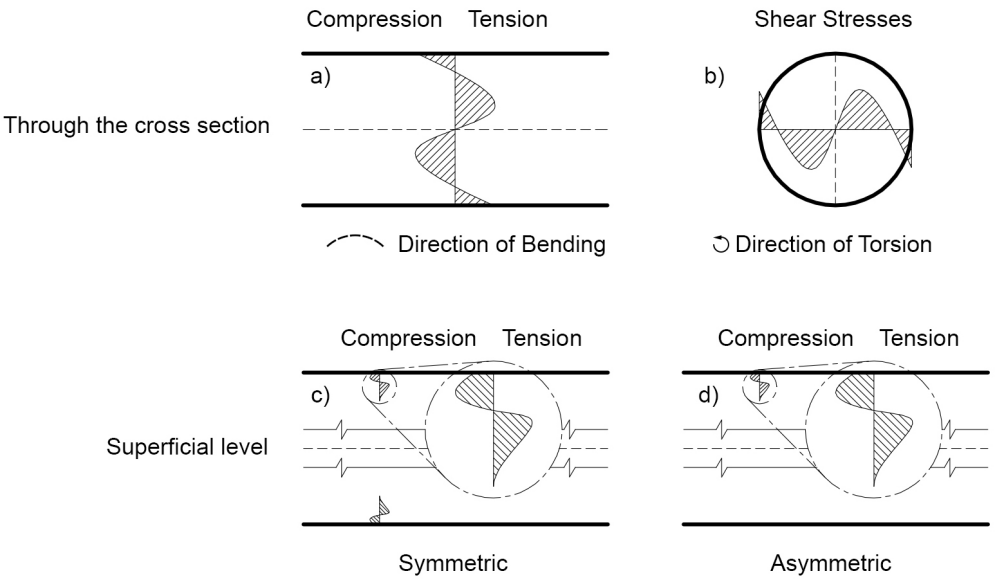

Figure 1.5: Residual stress process signature after unloading: (a) Bending, (b) Torsion, (c) Roller burnishing and (d) Ultrasonic needle peening. Adapted from [3, 43]

1.5 Reshaping simulation: challenges and perspectives

As stated before, nowadays, reshaping relies on the experience of a group of well-trained operators, the boilermakers. When introducing simulation in the process, the goal is to assist the operators and provide support during the decision-making step in order to reduce the number of operations needed to repair a part. However, from a technical point of view, reshaping simulation presents the following challenges:

- the initial distortion after machining δ_0 is unknown and, with the available state-of-the-art simulation techniques, there is a mismatch between the numerical prediction and the real distortion.
- distortions vary from one part to other (non-reproducibility), that is why reshaping cannot be standardized.
- simple 2D calculations are not able to represent properly neither the parts geometry nor the distortion phenomenon, and as a consequence, 3D simulations are required.

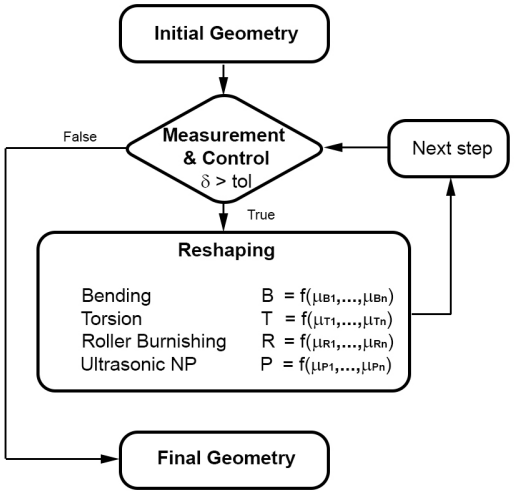

Figure 1.6: Reshaping simulation workflow diagram

- each time a new reshaping operation is performed, distortion changes and with it, the next reshaping operation and its technological parameters.
- to implement the numerical assistance in an industrial context, a real-time response is required.

The first challenge is related to an accurate prediction of residual stresses along the manufacturing chain. Theoretically, if the residual stress in a forged part is known before the machining step, it would be possible to determine the best location for the final geometry inside the blank, which minimizes any possible distortion. This approach works well for parts made from rolled plates [20, 23] due to the residual stress field is easier to determine compared to forged parts [102]. For the latter, important deviations from the numerical prediction respect to the real distortion where reported by Cerutti [19], as shown in Figure 1.7. As a consequence, any mismatch between the numerical and real initial distortion can invalidate any further reshaping simulation step.

The second limitation is due to the deterministic nature of numerical simulations. Once the solution has converged, if the algorithm is executed again, it is expected to obtain the same result (e.g. δ_0) while in reality, every time a new forged part is machined, although all the process parameters were not modified, a different

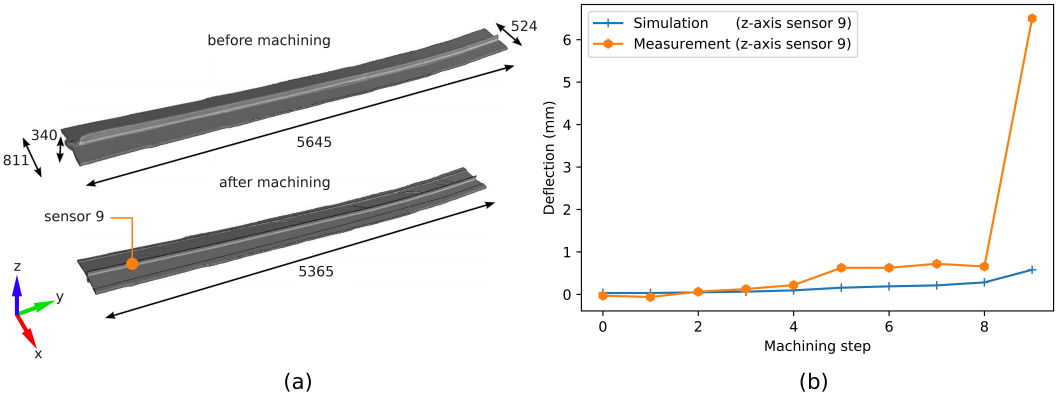

Figure 1.7: Example of distortion in a cruciform. (a) Geometry before and after machining. (b) Simulation vs measurements results. Adapted from [19].

value for δ_0 is obtained. This pattern is observed between parts of the same class and among symmetric parts (e.g left and right cruciform). Therefore, reshaping simulation needs to provide multiple possible initial distortion scenarios.

The use of 3D simulations to represent properly the distorted geometry implies the generation of numerical models with large degrees of freedom. It is a common practice to take advantage of any symmetry plane in order to simulate only one portion of the total part. Maybe the *symmetry trick* can be exploited during the first reshaping step. However, as the problem evolves and distortion gets more localized, the way each reshaping operation is applied obliges to simulate the whole structure.

About the fourth challenge, for each reshaping step i=1,2,3,..., the goal is to define the parameters associated with the operation μ_i that minimize the remaining distortion δ_i. It means that, for each reshaping step, it is required to run a multi-parametric analysis. The problem's complexity grows as previous and subsequent operations influence each other. Therefore, any error generated during a defined reshaping step will be forward propagated and can invalidate the simulation results.

In order to implement this numerical assistance tool in an industrial environment, it is required to access the simulation outputs in real-time, as the goal is to evaluate beforehand different scenarios for the reshaping step i and only then, to launch the real operation with the optimum configuration defined in advance.

Under the described scenarios, the requirement of multiple reshaping simulations

together with adaptive modelling and a real-time response suggests launching a multi-parametric analysis under a Model Order Reduction (MOR) framework. The idea for this approach is to produce a low-dimensional but accurate model in a cost-effective way which allows exploring beforehand the input space to construct a solution dictionary, known as *computational vademecum* [27].

1.6 Conclusions

Distortion of large aluminum forgings is an open problem for the aeronautical industry. Continuous research efforts are done in order to predict the residual stresses that generate this problem. However, it is important from an operational standpoint to study how to handle distortion once it has appeared. In this chapter, the required post-machining operations to mitigate distortion has been reviewed together with their associated simulation challenges. At the moment, reshaping is solved based on the empirical experience acquired for a group of well-trained operators. Now, the goal is to find a way to use advanced numerical simulations tools (e.g adaptive modelling, model order reduction) to study reshaping in a virtual environment and evaluate possible scenarios before launching the real operation. The long-term goal is to optimize the process in order to minimize the total number of reshaping operations and avoid introducing unnecessary residual stresses to the structural part.

Chapter 2

Residual stresses: selected numerical models

Residual stresses are the main cause of the post-machining distortion of large and thick-walled aluminium forgings. In the present chapter, the available numerical models for determining the residual stresses after quenching and plastic bending are introduced and validated for the case of rolled plates, taking advantage of its simple residual stress state and geometry. Both models will be used along the thesis to perform different analysis regarding bending straightening and they will be considered as the reference solution.

Contents

2.1 Introduction 18

2.2 Numerical models description and validation 19

2.2.1 Quenching simulation for residual stress prediction 19

2.2.2 Bending straightening simulation 24

2.3 Conclusions 27

2.1 Introduction

Aluminium forgings undergo a multiple-step manufacturing process to produce the final aeronautical component. We describe here a typical manufacturing sequence, although others are of course possible. First, forged blanks are typically produced on hydraulic presses with hot closed-dies [40]. The process continues with a solution heat treatment (SHT) followed by quenching, which is required to improve the mechanical properties of the material. As a counterpart, the quenching step is the main responsible for the creation of residual stresses due to the strong thermal gradients between the surface and the core of the part. Bi-axial compression stress state develops at the surface, counterbalanced by a three-dimensional tension state in the core [87]. After quenching, the components usually undergo a stress relief process (e.g. compression), followed by an ageing treatment, to reach the peak yield stress. Then, machining is used to obtain the final geometry from the blank. During this step, material removal breaks the stress equilibrium, producing a redistribution of residual stresses (RS) and, consequently, shape distortions [62, 89].

For the available reshaping operations discussed in chapter 1, in this thesis, we focus on the bending straightening operation only, which essentially consists in applying a load in the opposite direction to observed distortions. Bending straightening is an iterative loading-unloading process, where, for a given initial distortion, the operator has to guess: i) where to place the supports; ii) where to apply the bending load; and iii) how much loading needs to be applied to minimize distortion.

Diverse authors have proposed to use numerical simulation as a means to anticipate the resulting shape after a correction step. The idea is that, from the knowledge of the full residual state field prior to reshaping, it should be possible to simulate the correction steps. As residual stresses cannot be systematically measured in an industrial context, lots of efforts have been devoted to derive numerical models that are able to estimate them [52, 87]. These models require simulating, either wholly or in part, the multi-step manufacturing process. We shall refer to this approach throughout the thesis as the *sequential approach*, as depicted in Figure 2.1. Although the sequential approach can provide insightful results when good knowledge on both process conditions and material behaviour are available, most often, significant mismatch between numerical predictions and experimental observations is reported, e.g. [19]. Assessing how uncertainties propagate through the different manufacturing steps (i.e. from quenching to machining) is key to keep a high confidence level

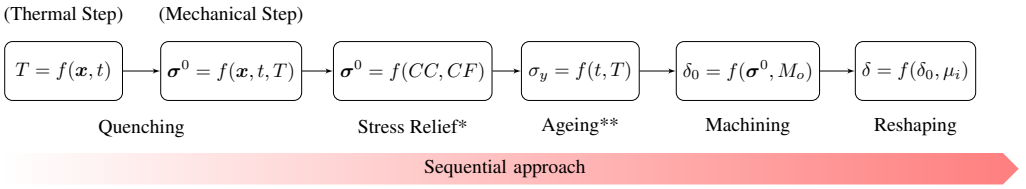

Figure 2.1: Residual stresses simulation by using the sequential approach (*not included and **included but not simulated).

on the predictions from sequential models [62, 118].

The chapter is organized as follows. In section 2.2, we present numerical models for residual stress prediction and bending straightening simulation, and validate them against available data in the literature. Then, some conclusions are provided in section 2.3.

2.2 Numerical models description and validation

In this section we present and validate numerical models for residual stress prediction and bending straightening. While aluminium forgings present a complex three-dimensional residual stress state [87, 102, 119], the residual stresses are well known for rolled plates and dominated by the longitudinal stresses within the thickness [19, 52, 78]. Experimental data on forged parts is scarce, given the difficulty of measuring complex 3D residual stress fields. Therefore, the numerical models presented in this section are validated against data for rolled plates, and then used in subsequent sections as a means to produce reference results in forged parts.

For the implementation, we rely on a well-known and extensively-used software package, Abaqus [106], based on the finite element method. We therefore provide a synthetic description of the models, making use of summarizing tables, and put more emphasis on the validation part.

2.2.1 Quenching simulation for residual stress prediction

The residual stresses generated after the heat treatment of quenching can be simulated as a sequentially coupled thermo-plasticity problem [52, 104]. The problem is divided into two computational steps: the heat transfer step and the mechani-

cal step. For the heat transfer step, the heat conduction equation is solved first. Once the temperature evolution in time is known, it is used as an input for the mechanical problem, which is affected via thermal expansion and the temperature-dependent constitutive model. By solving the mechanical step, the residual stress state is computed.

2.2.1.1 Thermo-plasticity modelling

The thermo-plasticity model used for quenching simulation is synthetically presented in Table 2.1. To this end, we consider a body that occupies an open bounded domain $\Omega \subset \mathbb{R}^{d\leq 3}$. Its boundary is denoted by $\partial\Omega$. We suppose that the part is at temperature T_0 (temperature of the solution heat treatment) at an initial time $t = 0$, when it is submerged into a liquid at a predefined temperature $T_\infty \ll T_0$ for a fast cooling during a time interval of interest $t \in [0, T_{\text{final}}]$. Heat transfer from the part to the surrounding liquid through the part's boundary $\partial\Omega$ is modelled as a convective boundary condition with a heat transfer coefficient denoted by h. By $T := T(\boldsymbol{x}, t)$, we denote the temperature evolution at a point $\boldsymbol{x} \in \Omega$ and time $t \in [0, T_{\text{final}}]$.

Once the heat transfer step is solved, the resulting temperature field is introduced in the mechanical step as a predefined field. As a consequence, volumetric strains are generated by the effect of thermal expansion. The strain tensor $\boldsymbol{\varepsilon}$ decomposed as the sum of an elastic component $\boldsymbol{\varepsilon}^e$, a plastic component $\boldsymbol{\varepsilon}^p$ and a thermal component $\boldsymbol{\varepsilon}^{th}$. Classical J_2 plasticity with Ramberg-Osgood [83] isotropic hardening is implemented.

2.2.1.2 Application to a rolled plate

In order to validate the model for residual stress prediction, we simulate a case from the literature for which residual stresses are available, see [78]. Specifically, we apply the model described in section 2.2.1.1 to a rolled plate data of 760×760×77.9 mm. The plate is oriented such that the x, y and z axis are parallel to the longitudinal (L), longitudinal-transverse (LT) and short transverse (ST) directions, respectively. Based on the symmetry present in all directions, only 1/8 of the geometry is simulated.

The quenching process conditions are summarized in Table 2.2. The rest of the modelling parameters given in Table 2.1 (i.e. ρ, C_p, κ, h, α, E, ν, σ_{y0}, k and n)

Table 2.1: Thermo-plasticity model for quenching simulation.

Thermal step modelling
Energy balance: $\rho C_p \frac{\partial T}{\partial t} + \nabla \cdot \boldsymbol{q} = 0$, together with Fourier's law for the heat flux $\boldsymbol{q} = -\kappa \nabla T$, in $\Omega \times (0, T_{\text{final}}]$.
Initial condition: $T = T_0$ at $\Omega \times \{0\}$.
Surrounding's predefined temperature: T_∞.
Convective boundary condition: $-\kappa \nabla T \cdot \boldsymbol{n} = h(T - T_\infty)$ on $\partial\Omega \times (0, T_{\text{final}}]$.
ρ, C_p, κ are the material's mass density, specific heat capacity and thermal conductivity, respectively. h is the heat transfer coefficient. These are taken as a function of the temperature.
$\boldsymbol{n}$ is the outward unit normal to $\partial\Omega$.
Mechanical step modelling
Momentum balance equation: $\boldsymbol{\nabla} \cdot \boldsymbol{\sigma} = \boldsymbol{0}$ in $\Omega \times (0, T_{\text{final}}]$.
Strain decomposition: $\boldsymbol{\varepsilon} = \boldsymbol{\varepsilon}^e + \boldsymbol{\varepsilon}^p + \boldsymbol{\varepsilon}^{th}$.
Hooke's law: $\boldsymbol{\varepsilon}^e = \frac{1}{2\mu}\left(\mathsf{I} - \frac{\nu}{1+\nu}\boldsymbol{I} \otimes \boldsymbol{I}\right) : \boldsymbol{\sigma}$ with $\mu = \frac{E}{2(1+\nu)}$, where I denotes the symmetric part of the fourth order identity tensor and $\boldsymbol{I}$ is the second order identity tensor.
Thermal strain increment: $\Delta\varepsilon_{ij}^{th} = \alpha \delta_{ij} \Delta T$, where δ_{ij} is the Kronecker delta.
Yield surface: $f(\boldsymbol{\sigma}) = \bar{\sigma}(\boldsymbol{\sigma}) - \sigma_y$, where $\bar{\sigma}(\boldsymbol{\sigma}) = \sqrt{3\,J_2}$, $J_2 = \frac{1}{2}\boldsymbol{s} : \boldsymbol{s}$ and $\boldsymbol{s} = \boldsymbol{\sigma} - \frac{1}{3}\text{tr}(\boldsymbol{\sigma})\,\boldsymbol{I}$. On the other hand, σ_y is the yield stress.
Ramberg-Osgood isotropic hardening: $\sigma_y = \sigma_{y_0} + k\,(\bar{\varepsilon}^p)^n$, with the effective plastic strain as $\bar{\varepsilon}^p = \int_0^t \sqrt{\frac{2}{3}\dot{\boldsymbol{\varepsilon}}^p : \dot{\boldsymbol{\varepsilon}}^p}\, dt$.
Flow rule: $\dot{\boldsymbol{\varepsilon}}^p = \dot{\gamma}\frac{\partial f}{\partial \boldsymbol{\sigma}} = \dot{\gamma}\boldsymbol{N}$ with $\boldsymbol{N} = \sqrt{\frac{3}{2}}\frac{\boldsymbol{s}}{\|\boldsymbol{s}\|}$.
E and ν are the Young's modulus and the Poisson's coefficient, respectively. α is the thermal expansion coefficient and σ_{y_0}, k and n are the Ramberg-Osgood model parameters. These are taken as a function of the temperature.

were taken from [52]. As most of them are temperature-dependent, we do not report them here for the sake of brevity.

Concerning the numerical model, the plate was meshed with 64,000 8-node linear hexahedron elements, with 40 elements in the through-thickness (ST) direction. The total number of nodes was 68,921. Abaqus element types are DC3D8 for the heat transfer analysis and C3D8R for the mechanical step. Figure 2.2 depicts the geometry, boundary conditions and mesh of the numerical model.

Table 2.2: Quenching model validation. Quenching process conditions from [52].

Parameters			
Initial temperature	T_0	467	$°C$
Quenching temperature (cold water)	T_∞	20	$°C$
Quenching time	T_{final}	500	s

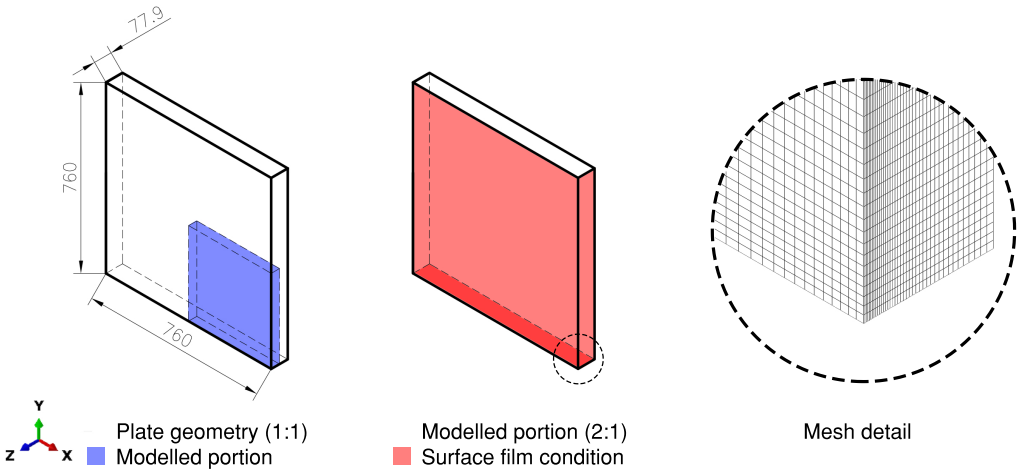

Figure 2.2: Left: plate geometry with indication of the modelled portion. Center: in red, boundaries to which a mixed-type boundary condition is applied (adiabatic conditions applied on the symmetry planes). Right: detail of the mesh.

2.2.1.3 Validation of the residual stress prediction

With the aim to validate the model, the longitudinal residual stresses σ_{11} at the center of the plate ($x = L/2$, $y = LT/2$) are compared against experimental measures. As explained in section 2.2.1.1, the temperature evolution as a function of time is the first outcome before obtaining the residual stresses during quenching. The strong thermal gradient between the core and the surface of the part is depicted in Figure 2.3a for the initial 30 seconds of simulation. This is the source for the non-homogeneous plastic strains which produce residual stresses. Once thermal equilibrium is obtained, Figure 2.3b shows σ_{11} along the thickness (z axis). We see that numerical predictions are in good agreement with experimental results, particularly in the internal area, whereas some border effect is observed near the surface. As a limitation, it should be noted that the model is not able to capture the local

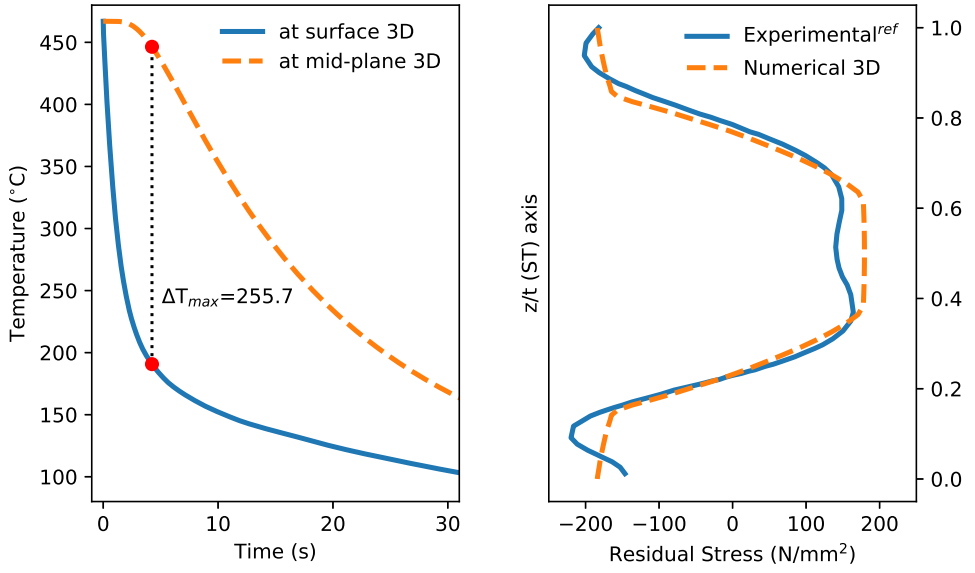

(a) (b)

Figure 2.3: Quenching simulation results at the center of the plate ($x = L/2$, $y = LT/2$): (a) Temperature evolution as a function of time; (b) Longitudinal residual stresses σ_{11} along the thickness (short transverse direction) and validated against results from [78].

minima observed in the center of the plate, which is caused by an inhomogeneity of mechanical properties through-thickness [34, 110] and produces in the 7XXX rolled plates the so called W-shape pattern of longitudinal yield strength through the ST direction [22].

For further assessment, Figure 2.4 shows a view on the 3D residual stress field. The RS pattern depends on the part's geometry and the thermal gradients generated during quenching [87]. As the model works under an isotropic material hypothesis, the stress components σ_{11} and σ_{22} are equal as they have the same dimension. In addition, they can be assumed as constant if the edge effects are neglected, which goes in line with the plane strain hypothesis used in some 2D models found in the literature [52, 78]. However, with a 2D model we would not be able to study forged geometries and their complex stress states.

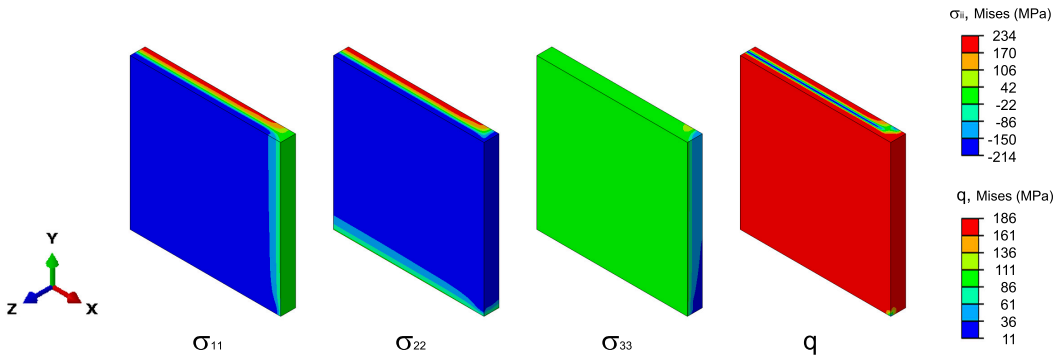

Figure 2.4: Simulation results: 3D residual stress field in a rolled plate after quenching.

2.2.2 Bending straightening simulation

In this section, we consider a part with an internal residual stress field, coming either from the literature (in simple hot rolled parts mainly), from the quenching simulation model presented in section 2.2.1.1, or from any subsequent operation, such as stress relief or machining. In general, it is convenient to assume that at the outset of the simulation the part is stressed by some initial residual stresses, $\boldsymbol{\sigma}_0$. Considering that mechanical state, the objective is to develop a numerical model for bending straightening simulation.

2.2.2.1 Elasto-plasticity modelling

Bending straightening is an iterative procedure where the loading-unloading pattern can be considered as a cyclic behaviour. Therefore, it is crucial to take kinematic hardening into account for the accuracy of the results. To this end, we use the Chaboche model [21, 76], which is synthetically presented in Table 2.3 together with the momentum balance equation, which has to be satisfied at each loading step.

Remark 2.1 (*On the material modelling*). A temperature-dependent version of the Chaboche model could have been used in section 2.2.1.1 for residual stress prediction after quenching. However, this kind of model is far more complex to characterize than the Ramberg-Osgood model, which in addition, proved to be accurate enough to capture the main mechanisms in residual stress creation.

Table 2.3: Elasto-plastic model with kinematic hardening for bending straightening simulation

Momentum balance equation: $\boldsymbol{\nabla} \cdot (\boldsymbol{\sigma} - \boldsymbol{\sigma}_0) = \mathbf{0}$ in Ω, where $\boldsymbol{\sigma}_0$ is the initial residual stress field.
Strain decomposition: $\boldsymbol{\varepsilon} = \boldsymbol{\varepsilon}^e + \boldsymbol{\varepsilon}^p$.
Hooke's law: $\boldsymbol{\varepsilon}^e = \frac{1}{2\mu}\left(\mathsf{I} - \frac{\nu}{1+\nu}\boldsymbol{I} \otimes \boldsymbol{I}\right) : \boldsymbol{\sigma}$ with $\mu = \frac{E}{2(1+\nu)}$, where I denotes the symmetric part of the fourth order identity tensor and $\boldsymbol{I}$ is the second order identity tensor.
Yield surface: $f(\boldsymbol{\sigma}, \boldsymbol{X}, R) = \bar{\sigma}(\boldsymbol{\sigma} - \boldsymbol{X}) - R - \sigma_{y0}$, where $\bar{\sigma} = \sqrt{3J_2}$, $J_2 = \frac{1}{2}(\boldsymbol{s} - \boldsymbol{X}) : (\boldsymbol{s} - \boldsymbol{X})$ and $\boldsymbol{s} = \boldsymbol{\sigma} - \frac{1}{3}\mathrm{tr}(\boldsymbol{\sigma})\boldsymbol{I}$.
Kinematic hardening rule: $\boldsymbol{X} = \sum_{i=1}^{m} \boldsymbol{X}_i$ where $d\boldsymbol{X}_i = \frac{2}{3}C_i d\boldsymbol{\varepsilon}^p - \gamma_i \boldsymbol{X}_i d\bar{\varepsilon}^p$, with the effective plastic strain as $\bar{\varepsilon}^p = \int_0^t \sqrt{\frac{2}{3}\dot{\boldsymbol{\varepsilon}}^p : \dot{\boldsymbol{\varepsilon}}^p}\, dt$.
Isotropic hardening rule: $dR = b(Q - R)\, d\bar{\varepsilon}^p$.
Flow rule: $\dot{\boldsymbol{\varepsilon}}^p = \dot{\gamma}\frac{\partial f}{\partial \boldsymbol{\sigma}} = \dot{\gamma}\boldsymbol{N}$ with $\boldsymbol{N} = \frac{3}{2}\frac{\boldsymbol{s}-\boldsymbol{X}}{\bar{\sigma}}$.
E and ν are the Young's modulus and the Poisson's coefficient, respectively. σ_{y0} is the initial yield stress and b, Q, C_i and γ_i material parameters of the Chaboche model [21].

Another important aspect that needs to be included in the numerical model is the interaction between the actuator that applies the load and the part, as well as the interaction between the part and the supports. The exact geometry of both the actuator and the supports depends on the experimental setup, and therefore a more precise description will be given in section 2.2.2.2. These are included in the model as rigid (undeformable) bodies. A Coulomb's frictional contact is considered between the actuator or the supports and the part. A penalty formulation is used for the numerical solution of the model. [106].

2.2.2.2 Application to a four-point bending setup

In order to validate the model presented in section 2.2.2.1, a four-point bending experiment was carried out. The geometry of the tested sample (machined from a hot rolled plate) as well as the experimental setup are shown in Figure 2.5.

The beam was plastically deformed by applying three cycles of loading and unloading. The amplitude of the cycles is ±9.5 mm, imposed by the hydraulic press, as a controlled displacement. Strain is recorded by two gauges placed at the top and bottom faces, labelled as J1 and J2, respectively. The sensors are located at

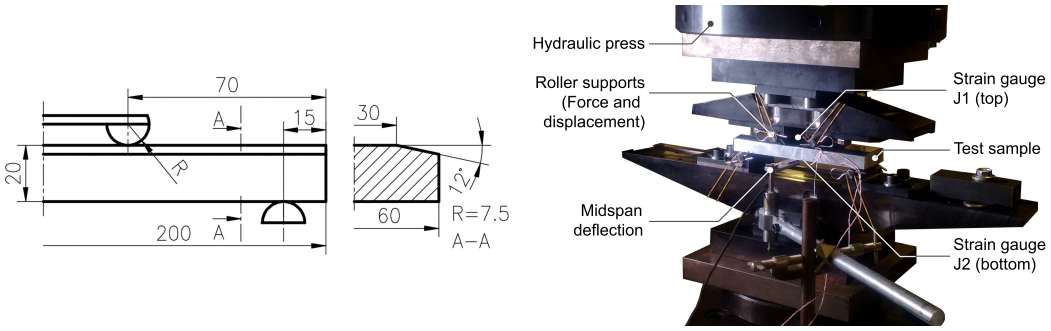

(a) Geometry of the sample (b) Experimental setup

Figure 2.5: Four-point bending experiment for the validation of the bending straightening model

Table 2.4: Chaboche's material model parameters for AA7010 [36]. All units are in MPa except for ν, b and γ_i which are dimensionless.

E	σ_y	ν	Q	b	C_1
73000	390	0.3	-145.7	239.4	38973.6
C_2	C_3	γ_1	γ_2	γ_3	
195910	3298.1	275.5	3134.6	23.4	

the intersection of both longitudinal and transverse symmetry planes of the beam. In addition, displacements are recorded at two locations: at the mid-span of the beam and at the location where the force is applied. The force data acquisition is done by the hydraulic press head. In order to ensure repeatability, the experiment is performed in two samples, labelled as L1 and L2.

Concerning the numerical model, the plate was meshed with 56000 eight-node linear hexahedron elements (type C3D8R) and 64539 nodes. A Coulomb's friction coefficient $\mu = 0.05$ was considered between the tool and the sample [55]. The material is an aluminium alloy AA7010, previously characterized by Airbus Central Research and Technology [36]. Material parameters are summarized in Table 2.4. The backstress tensor $\boldsymbol{X}$ in the Chaboche's model is described with three terms, i.e. $m = 3$, see Table 2.3.

Finally, as discussed above, it is essential to have good knowledge on the residual

stress field. As the tested sample is a rolled plate in a temper designation Txx51, meaning stress relief by stretching, it is expected to have a well-known residual stress profile, in the range of ±30 MPa [88, 102]. The residual stress profile reported in [78] was considered in the simulation.

2.2.2.3 Validation of the bending straightening model

As a means to validate the simulation model, we use force versus strain measures generated during reshaping. Figure 2.6a presents a comparison of the experimental measures at gauge J1, for both specimens L1 and L2, against the numerical prediction. Figure 2.6b presents essentially the same results but at gauge J2. We first observe a very good repeatability between specimens L1 and L2, whose results match almost perfectly. Most importantly, a good agreement between the numerical results and experimental measures is observed in all cases.

2.3 Conclusions

From a numerical point of view, when it comes to determine the residual stresses between a rolled plate and a forge after quenching, the only difference at an input level is its geometry. In this chapter, we took advantage of this abstraction to present a numerical model to estimate the residual stresses after quenching for a rolled plate. The model was validated with a case available in the literature. Following the same line, a Chaboche material model was tested experimentally for plastic bending. By combining both models, we have the required tools to generate numerically a post-machining distortion in a forge and simulate the reshaping operation of bending straightening.

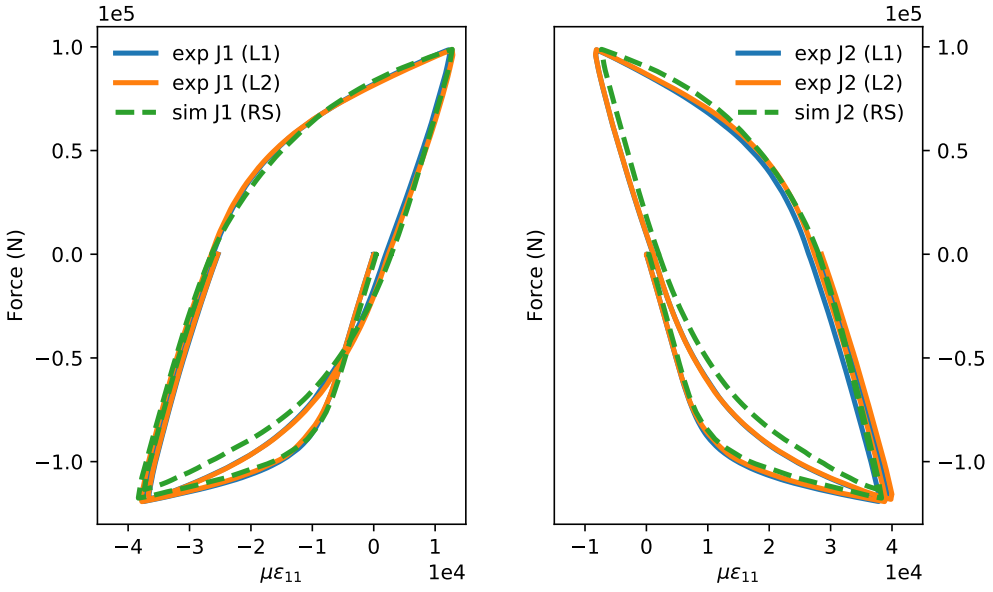

(a) (b)

Figure 2.6: Validation of the bending straightening simulation model via strain versus force measures: comparison of the simulation results (dashed line) and the experimental measures (solid line) for two specimens labelled L1 and L2. (a) Comparison for strain gauge J1 (located at top) and (b) Comparison for strain gauge J2 (located at bottom).

Chapter 3

Reshaping diagrams for bending straightening

In this chapter, we are concerned with the development of efficient computer simulation tools to assist operators in bending straightening, which is one of the most common reshaping operations. Our approach is based on the computation of reshaping diagrams, a tool that allows selecting a nearly optimal bending load to be applied in order to minimize distortion. Most importantly, we show that the reshaping diagram needs not to account for the residual stress field, as its only effect is to shift of the reshaping diagram by some offset. That is, the overall behaviour including a realistic 3D residual stress field in a forged part can be retrieved by shifting the *residual stress free* reshaping diagram by the appropriate offset. Finally, we propose a strategy in order to identify the offset on-the-fly during the reshaping operation using simple force-displacement measures.

Contents

3.1 Introduction **31**

3.2 Numerical study of forged parts **32**

3.2.1 Residual stress after quenching 33

3.2.2 Residual stresses after machining 34

3.2.3 Reshaping diagrams for bending straightening 37

3.2.4 Parametric study of the reshaping diagram 39

3.3 Residual stress free diagrams for simulation-assisted reshaping 41
3.3.1 Linear unloading path in the force-displacement diagram . 43
3.3.2 Reshaping offset calibration 46
3.4 Conclusions 48

3.1 Introduction

In this chapter, we deviate from the sequential approach and propose an alternative route to simulate bending straightening of forged components. We first introduce a simple tool, the reshaping diagram, which provides the remaining distortion (i.e. after unloading) as a function of the applied bending load (for fixed rollers position and residual stress field). Note that the reshaping diagram is a very convenient tool to assist the operator: once it is made available, the reshaping operation reduces to select the optimal bending load that minimizes the remaining distortion. Unfortunately, computing the reshaping diagram requires a precise knowledge on the residual stress field, which as discussed above, is not a trivial task. To overcome this issue, we propose a workaround that uses distortion (which is measurable) as the main input, instead of residual stresses. The underlying idea is that to minimize distortion we may not need a precise knowledge of the residual stress field, but only its influence on the reshaping diagram. Therefore, we compute the reshaping diagram of a distorted part without residual stresses, that is, we keep the distorted geometry after machining but suppress the residual stress field. We shall refer to this reshaping diagram throughout the entire paper as the *residual stress free* (RSF) approach (see Figure 3.1). Then, we show that the effect of the RSF hypothesis results only in a shift of the reshaping diagram. That is, the overall behaviour including a realistic 3D residual stress field in a forged part can be retrieved by shifting the original reshaping diagram by the appropriate offset. Finally, we propose a strategy in order to identify the offset on-the-fly during the reshaping operation using simple force-displacement measures. One of the main advantages of the RSF approach is that it does not require any prior knowledge on the residual stress field; it only requires information on the distorted shape, which unlike the residual stresses, can be systematically measured in an industrial environment.

This chapter is organized as follows: in section 3.2, by using the validated models previously presented in chapter 2, we create realistic 3D stress states for forged parts and compute the reference reshaping diagram by simulating the bending straightening process. The influence of various process parameters is also analysed. In section 3.3, we repeat the operation with the residual stress free hypothesis and observe that the obtained RSF reshaping diagram differs only by some offset from the reference one. In addition, we derive a simple approach to calibrate the offset on-the-fly during the reshaping operation using simple force-displacement measures. Finally,

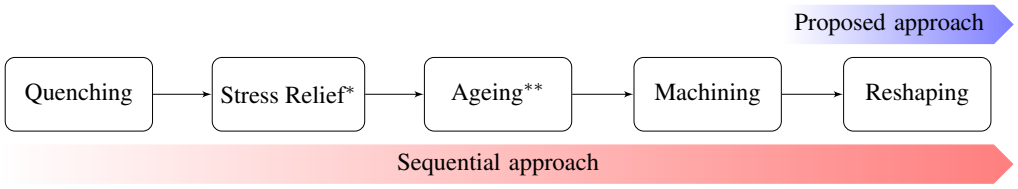

Figure 3.1: Reshaping simulation: sequential vs proposed approach (*not included and **included but not simulated).

in section 3.4, we draw some conclusions and perspectives for future work.

3.2 Numerical study of forged parts

In this section, the numerical model presented and validated in section 2.2 is applied to the study of forged parts. As a reference geometry, we consider a beam with T-shaped cross-section, a simplified version of the cruciform, but still representative in terms of the thickness or the radius of the fillets.

Figure 3.2a shows the cross section of both the T-shaped beam and the bulk from which it is machined, with their geometric dimensioning. The final geometry is obtained through milling by removing 73 % of the bulk material. As this step is done numerically, no information is provided regarding the finishing condition and cutting parameters.

An important parameter for the machining process is the so-called machining offset (M_o), depicted also in Figure 3.2a, which controls the positioning of the beam in the bulk. We shall analyse the strong influence of the machining offset on the resulting post-machining residual stress field, and by consequence, on the distortion. Figure 3.2b shows a parametrized four-point bending configuration, where several configurations are considered in terms of the distance between the supports and the distance between the loading points.

The simulation parameters are the same used in section 2.2, except for the geometry.

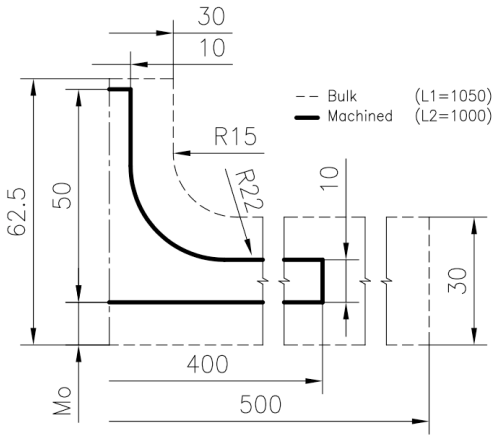

(a) Geometry definition of both the bulk and the machined part, as a function of the machining offset M_o

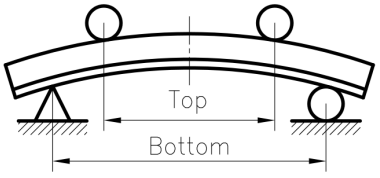

Mo (mm)	10			5		
Position ID	P1	P2	P3	P4	P5	P6
Top (mm)	300	600	300	900	900	600
Bottom (mm)	900	900	600	300	600	300

(b) Bending straightening setup and parametrization of the positioning of both top and bottom rollers

Figure 3.2: Reference geometry for the simulation of bending straightening of forged parts: a beam with T-shaped cross section

3.2.1 Residual stress after quenching

The thermo-plasticity model presented in section 2.2.1.1 is now applied to the T-shaped beam (bulk, i.e. before machining). Whereas the plate geometry in section 2.2.1.2 exhibited a nearly unidirectional (through thickness) heat conduction, the temperature field in the T-shaped beam is somewhat more complex to explain. To describe it in a simple manner, we consider control points in three main areas of the beam: the wing, the rib and the fillet. To each of these points, located on the surface, we associate an interior pairing point, with the objective of quantifying the temperature difference between the surface and the core. Figure 3.3 shows the positioning of the control points and compares the temperature evolution. Interior points are located following the normal to the outer boundary.

Temperature profiles are significantly different from one region to another, see Figure 3.3. The maximum temperature difference between internal and external control points takes place in the fillet. The curved zone is the last one to reach the thermal equilibrium, maximizing the development of non-homogeneous strains. Therefore, we can expect to have the maximum residual stresses in that region.

Figure 3.4a shows the residual stress field for the quenched bulk when the room

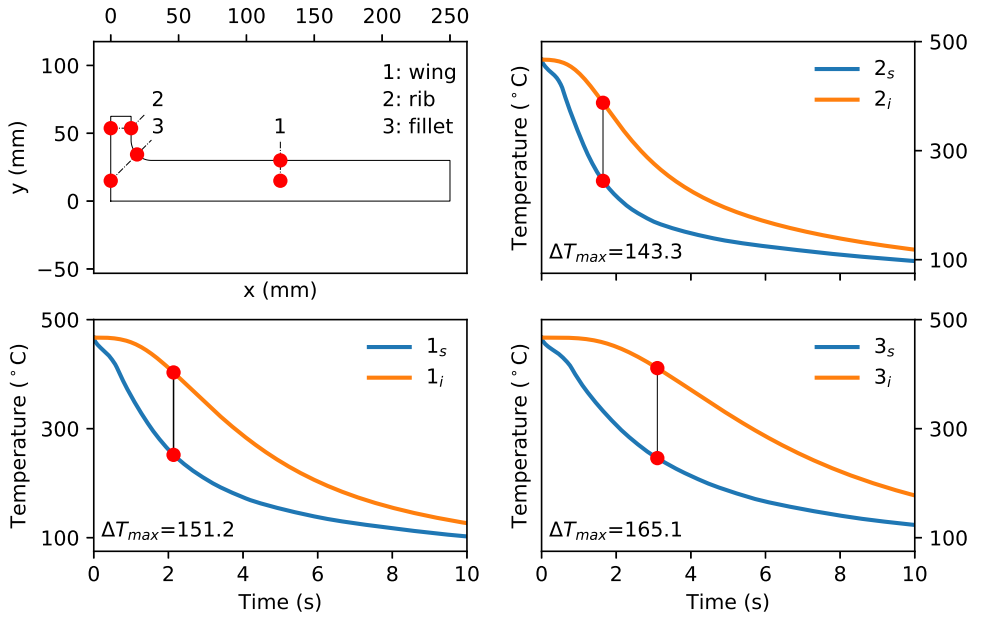

Figure 3.3: Temperature evolution in the T-shaped beam (bulk) during the first 10 seconds of simulation at the (1) wing, (2) rib and (3) fillet. The cross section corresponds to the symmetry plane $z = 0$ and the subscripts s and i refer to the surface and internal points.

temperature has been reached. As expected, the surface is subjected to compression stresses, which are equilibrated by tension stresses in the core. As the structural part is under a three-axial stress state, to know where plasticity has occurred, we use the von Mises yield criterion. As the yield stress σ_y in the as-quenched state is 162 MPa, it can be appreciated on the bottom section of Figure 3.4a, how all the elements coloured in red have plastified and how its distribution is not homogeneous across the geometry.

3.2.2 Residual stresses after machining

After quenching, machining takes place to extract the T-shaped beam from the bulk. Material removal breaks the stress equilibrium producing a redistribution of residual stresses and, consequently, shape distortions. One of the main parameters of the machining step is the machining offset (M_o), defined in the introduction of

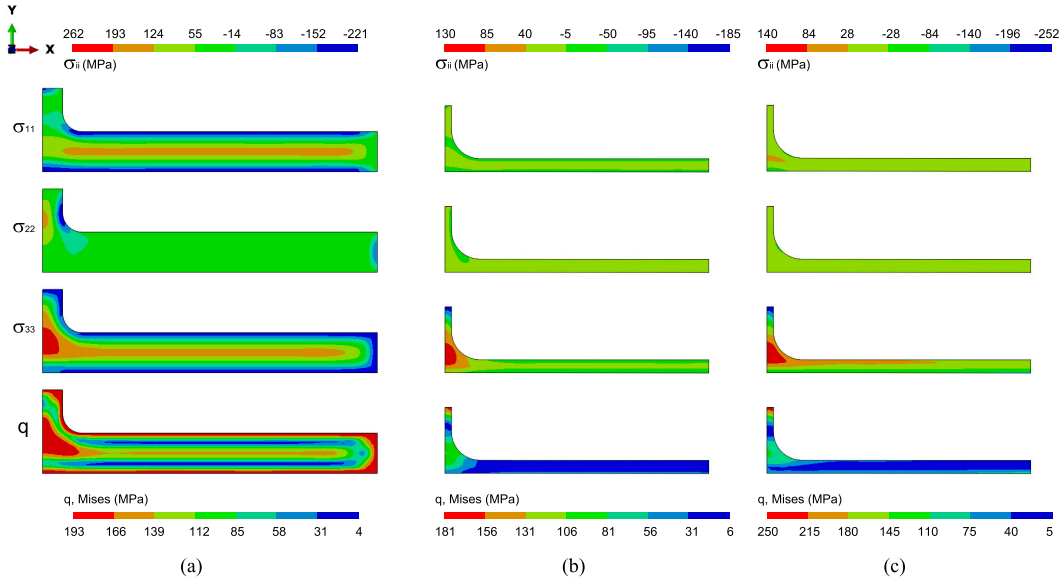

Figure 3.4: Residual stress distribution in the T-shaped beam: (a) after quenching (bulk), (b) after machining with $M_o = 10$ mm (case A) and (c) after machining with $M_o = 5$ mm (case B). All the snapshots are taken in the symmetry plane $z = 0$ and presented in the undeformed configuration.

section 3.2, which controls the positioning of the T-shaped beam inside the bulk. We should therefore expect different post-machining distortion levels depending on the choice of $M_o \in [1, 12]$ mm.

In order to provide an overall look on all possible shapes prior to reshaping, we carry out a parametric study on the effect of the machining offset.

Machining is modeled using the *death-birth* method [62], in which the material removal is simulated by deactivating the elements outside the machined geometry. The method requires to define the machined geometry as a subset in the mesh of the bulk.

Residual stresses introduced by machining have an impact in a superficial layer with a depth range of 250-300 μm [38, 59], therefore, they must be included in the distortion simulation for parts with thin wall thickness $t < 4$ mm [103]. For this class of parts, the no inclusion of machining-RS can lead to a different pattern of distortion respect to the numerical prediction [63]. As we focus on forgings where the machined components are considered as thick walled, machining RS are not

included, following the procedure described in [60]. As a consequence, the effects of clamping, cutting force and heat are not considered in the model.

As machining takes places after ageing, σ_y evolves from 162 MPa to 390 MPa (see remark 3.1). Therefore, the redistribution of bulk RS, which are the main cause of distortion [47, 102], are inside of the elastic region and it is possible to perform the machining operation in one single (deactivation) step. However, before arriving to that conclusion, the authors have considered different machining configurations, including a sequential deactivation by zones previous to obtain the final geometry and the results in terms of distortions were the same.

Remark 3.1 (*On stress relief and ageing*). Other manufacturing steps may take place after quenching and prior to the machining step, including stress relief and ageing. For simple geometries such as rolled plates and sheets, stress relief by stretching is usually carried out, whereas cold compression is preferred for forged parts [88, 91]. However, stress relief is often not possible for complex geometries [90]. Stress relief is not included in this study, as the main idea is to maximize the initial distortion caused by residual stress to place ourselves in the most adverse scenario. After the stress relief operation, the yield stress σ_y is increased via a second heat treatment called *precipitation hardening* or *ageing*. This change of material properties is caused by a blockage of dislocations or defects in the crystal lattice [99]. It is reported that ageing does not affect the residual stresses [90]. Ageing is taken into account via material modelling with an increased yield stress ($\sigma_y = 390$MPa)(Chaboche kinematic hardening).

By varying the machining offset, two types of distortion are observed: bending along the longitudinal direction, also referred to as distortion type 1, and wings closure, also referred to as distortion type 2.

Figure 3.5 shows distortion after machining, both type 1 and type 2, as a function of the machining offset. It can be seen that for lower offset values bending distortion takes predominance over wings closure, whereas the opposite is observed for higher values of the machining offset. In general, both distortions tend to become negative as machining offset increases, meaning that bending inverts and wings open instead of closing. To illustrate the behaviour, we select two specific values of the machining offset parameter, labelled as configuration A and B, which correspond to $M_o = 10$ mm and $M_o = 5$ mm, respectively. Figures 3.4b and 3.4c show the stress components for the machining cases A and B, respectively. Note that significantly different stress distributions are obtained by modifying M_o only.

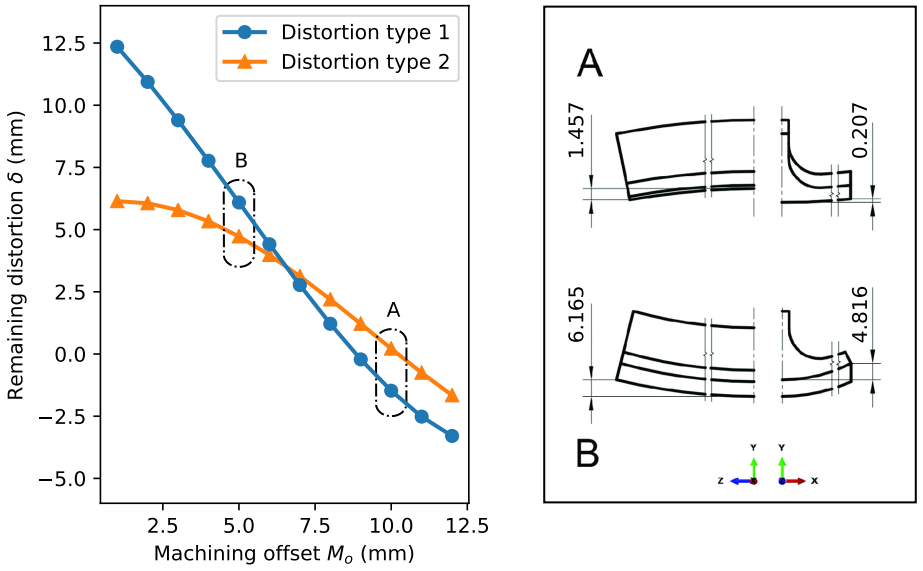

(a) (b)

Figure 3.5: T shaped beam model. (a) Distortion after machining as a function of machining offset M_o. (b) Distorted shape for case A ($M_o = 10$ mm) and case B ($M_o = 5$ mm).

3.2.3 Reshaping diagrams for bending straightening

We shall now concentrate on distortion of type 1, the only one that bending straightening can deal with. We measure distortion relative to the longitudinal axis of the part. Let $\mathbf{z}$ and $\mathbf{z}_{\text{nom}}$ be the coordinates of longitudinal axis of the distorted and the nominal (undistorted) part, respectively. It is implicit that $\mathbf{z}$ is measured in the deformed state. Let $\mathbf{n}$ be the unit normal in the bending plane to the longitudinal axis at $\mathbf{z}_{\text{nom}}$. Distortion of type 1 is using a peak-to-peak amplitude measure:

$$\delta = \max(d) - \min(d) \quad \text{with} \quad d = (\mathbf{z} - \mathbf{z}_{\text{nom}}) \cdot \mathbf{n}. \tag{3.1}$$

In the case of the T-shaped beam, the longitudinal axis of the undistorted part can be made coincident with $\mathbf{z}_{\text{nom}} \equiv \mathbf{0}$. The bending plane is the plane $z = 0$, and therefore the normal is $\mathbf{n} = (0, \pm 1, 0)$, the sign being arbitrary.

Assume a fixed machining offset, leading to an initial distortion δ_0, which is

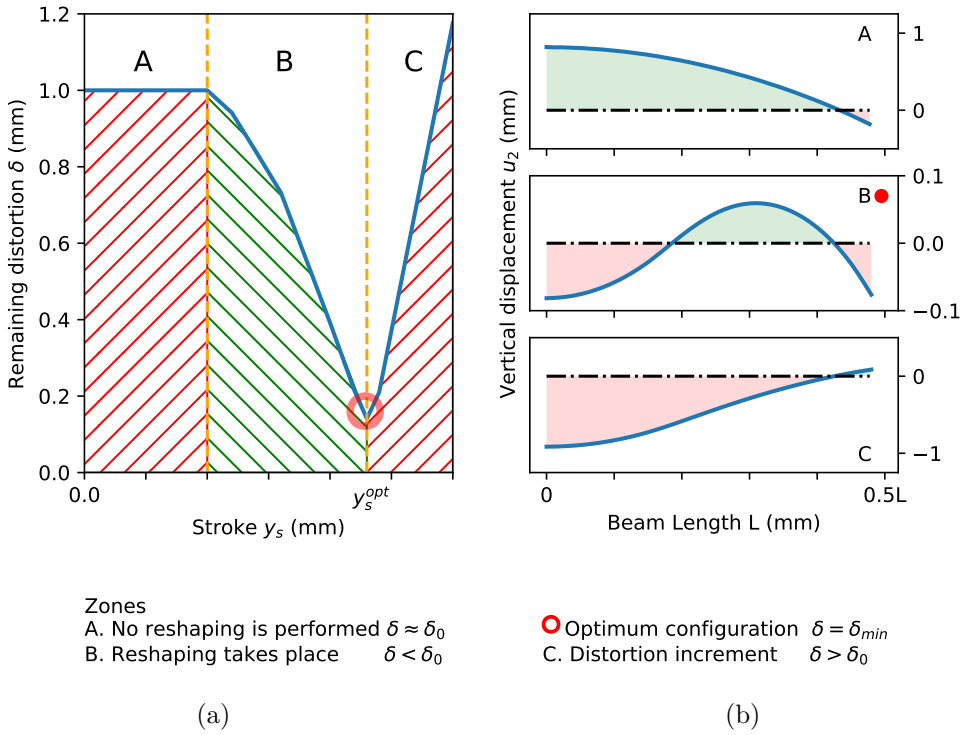

(a) (b)

Figure 3.6: Reshaping diagram (scheme). (a) The three characteristic regions of the reshaping diagram: elastic area of no repair (A), repairing area (B) and inversion area (C). (b) Shape after reshaping for values of the stroke in each reshaping region.

assumed known as it can be measured. For a given reshaping configuration (i.e. rollers positioning), the bending straightening operation consists in guessing the stroke y_s (equivalently, bending load) that should be imposed to minimize distortion after unloading. Note the parametric dependence of distortion as a function of stroke, $y_s \mapsto \delta(y_s)$. To assist operators to make their decision, we may rely on the simulation model developed in section 3.2.2. By sweeping over the range of stroke values, and carrying out a loading-unloading cycle simulation for each stroke, we obtain the *reshaping diagram* shown in Figure 3.6.

Three distinct areas can be identified. For low values of stroke (zone A), the part remains inside of the elastic domain and consequently distortion remains at its initial value, $\delta \approx \delta_0$. A reduction of the initial distortion is only possible when

plasticity takes place. Here, the new residual stresses generated during the reshaping operation counteract the previous stress state. We labelled this region as zone B in Figure 3.6, where $\delta < \delta_0$. Inside this zone, there is an optimum configuration, where distortion is minimized, (i.e. $y_s^{opt} \mapsto \delta_{\text{opt}}$). Finally, zone C comes after reaching the minimum, it is characterized by increasing distortions for higher stroke.

Figure 3.6b shows the deformed shape (longitudinal axis only) for three different values of stroke, one for each of the identified region. Specifically, the optimum is shown for zone B. The location of the bottom roller is the reference line. Green and red areas correspond to the points above and below the reference line, respectively (also, these correspond to the sign of d as defined in Eq.(3.1)).

Note that the reshaping diagram is a very convenient tool to assist the operator: once it is made available, the reshaping operation reduces to select the optimal bending load that minimizes the remaining distortion. Unfortunately, computing the reshaping diagram requires a precise knowledge on the residual stress field, which is not a trivial task. We shall discuss in section 3.3 an alternative approach based on the idea that, to minimize the distortion, we may not need a precise knowledge of the residual stress field, but only its influence on the reshaping diagram.

3.2.4 Parametric study of the reshaping diagram

The reshaping diagram in Figure 3.6 was computed for a fixed machining offset and rollers positioning. To provide further insight, in this section we consider six possible configurations by combining two values of the machining offset parameter and three rollers positioning. Each configuration is labelled as P1 to P6. The specific values for each of these is given in Figure 3.2b. Note that rollers positioning is inverted in configurations P4 to P6, compared to P1 to P3, because the deformed shape is also inverted.

Figure 3.7 shows the reshaping diagrams obtained for each of the six configurations. The same three areas described above can be distinguished. Figure 3.7a shows configurations P1 to P3, which correspond to a machining offset of $M_o = 10$ mm. Figure 3.7b shows configurations P4 to P6, which correspond to a machining offset of $M_o = 5$ mm.

One of the main conclusions that can be drawn from Figure 3.7 is that the position of the rollers has significant impact on the reshaping diagram. For instance, let us consider configurations P1 and P3. For both configurations, the internal rollers

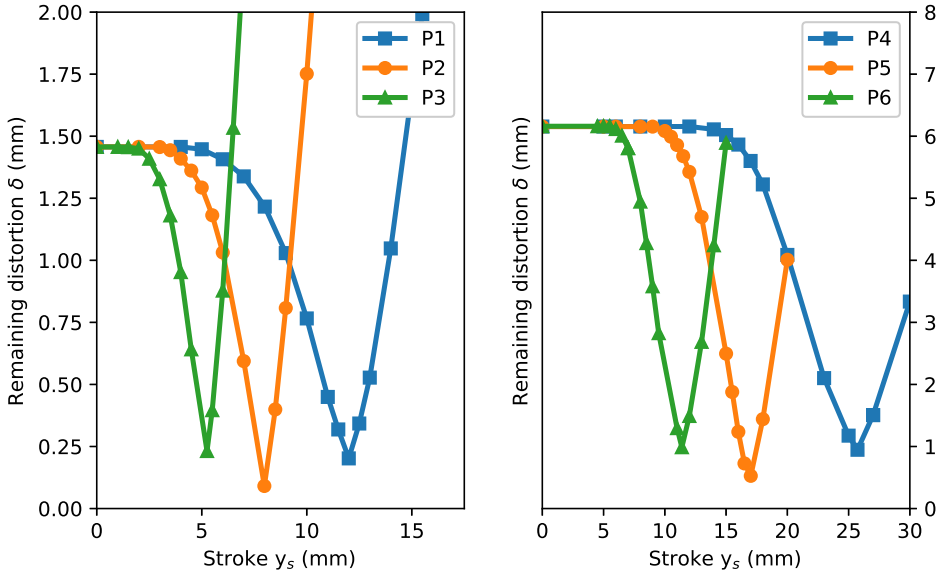

Figure 3.7: Parametric study of the reshaping diagrams for six combinations of machining offset and the rollers positioning (values given in Figure 3.2b): (a) $M_o =$ 10 mm (case A) and three rollers positioning. (b) $M_o = 5$ mm (case B) and three rollers positioning.

(loading) are positioned at 300 mm, whereas the external rollers (supports) are at 900 mm and 600 mm, respectively. Both configurations reach a similar value of optimal distortion, but the stroke to be applied is P1 almost doubles that of P3. This is to be expected, as configuration P1 is less rigid respect to P3[1]. As a consequence, P1 requires more deflection to reach plasticity. Another important effect that can be noticed is related to the sensitivity of the optimum. By sensitivity we mean

[1]For a beam, the force-displacement diagram can be used to calculate the stiffness of the structure, which is defined by the Equivalent Young's Modulus E_0 and corresponds to the slope of the curve. In a four point bending configuration, E_0 is defined as $E_0 = 24EI/\left[\left(3L^2 - 4a^2\right)a\right]$, where E, I, L and a correspond to the Young's Modulus, the inertia of the cross section, the span between external supports and the distance between one single external and internal roller, respectively. For example, if we express L and a in terms of the span of P1 (900 mm), both pair of parameters are $(L, L/3)$ for P1 and $(2L/3, L/6)$ for P3, respectively. By replacing both sets of values in the previous expression, we found that $E_{0(P1)} = 11/46E_{0(P3)}$.

the change in distortion as the optimal stroke is affected by some perturbation, i.e. $y_s^{\text{opt}} + \varepsilon \mapsto \delta_{\text{opt}} + \Delta\delta$. Clearly, the configuration P1 is less sensitive to perturbations in the stroke and therefore, in practice it should be easier to achieve. This effect becomes even clearer if the comparison is made between P4 and P5.

3.3 Residual stress free diagrams for simulation-assisted reshaping

As discussed in section 3.2.3, reshaping diagrams can be very helpful, provided that the residual stress field is known. However, at least two drawbacks can be outlined:

- Residual stress computation requires running sequential simulation models that account for all manufacturing steps prior to reshaping. Therefore, one needs to keep track of all process conditions and part history to run accurate predictions. Moreover, this process can be computationally intensive and time-consuming.
- Uncertainties linked to modelling and process conditions are likely to have a significant impact. To compute a trustworthy residual stress field, one would need to assess carefully how uncertainties propagate through the simulation chain.

To overcome these issues, we propose an alternative approach. The underlying idea is that to minimize the distortion we may not need a precise prediction of the residual stress field, but only its influence on the reshaping diagram. Let us consider the parametric study already presented in section 3.2. For each of the configurations P1 to P6, we compute the reshaping diagram of a distorted part but neglecting the residual stress field. That is, we keep the distorted geometry after machining but suppress the residual stress field. The results are shown in Figure 3.8.

From Figure 3.8 we can conclude that neglecting the residual stresses results only in a shift of the reshaping diagram: $\delta(y_s) \approx \delta_{\text{RSF}}(y_s^{\text{RSF}} + \Delta y_s)$. In other words, the overall behaviour including a realistic 3D residual stress field can be retrieved from the residual stress free diagram, provided that we are able to devise a strategy to identify the appropriate offset Δy_s.

The reshaping offset can be negative, as in Figure 3.8a, or positive, as in Figure 3.8b. To explain this behaviour, let us study the P5 configuration. Here, as the

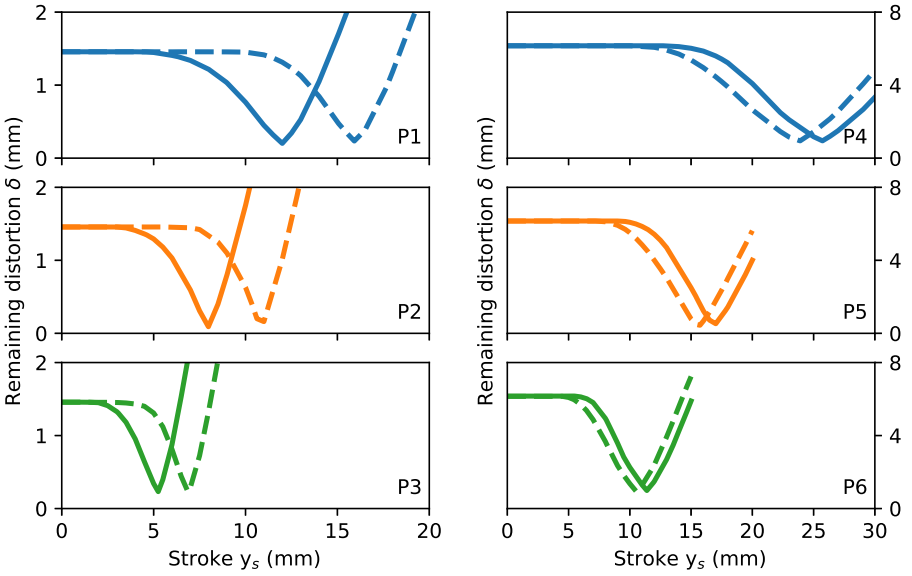

(a) (b)

Figure 3.8: Residual stress free reshaping diagrams (dashed line) against *true* reshaping diagrams that account for full 3D residual stress field (solid line), for six different reshaping configurations.

initial distortion has a U shape, bending is applied upwards and therefore, tension is induced along the rib. However, the rib is initially in compression due to the residual stresses (see $\boldsymbol{\sigma}_{33}$ in Figure 3.4c). As consequence of this inversion of stresses, more stroke needs to be applied in order to reach the yield surface, compared to the residual stress free case. As a general rule, if the stresses generated during reshaping oppose the initial residual stresses, the offset will be positive; otherwise, it will be negative.

The residual stress free approach has many advantages:

- It uses as the main input the initial distortion after machining, which unlike stresses, can be measured on a systematic basis.
- The underlying numerical model is rather simple, as it only needs to account for the bending straightening step. The computational cost is drastically reduced. See Figure 3.1 for comparison.

- Modelling involves less parameters and, therefore, limited uncertainty. Furthermore, we can deal with uncertainties via the reshaping offset, to be identified experimentally.

3.3.1 Linear unloading path in the force-displacement diagram

In this section, we introduce the linear unloading path hypothesis, which is key for offset calibration. Our goal is to calibrate the offset without actually having to perform loading-unloading cycles, which would be very impractical. The linear unloading is a simplification hypothesis to anticipate springback without actually unloading the part. The idea is to approximate the unloading path in the force-displacement diagram (which is generally non-linear) with a linear behaviour[2]. The slope for such linear unloading (sometimes referred to as the equivalent Young's modulus) is computed in the linear part of the force-displacement diagram as $\Delta F/\Delta u$, during loading and before yielding. This is a common engineering practice already well-documented in the literature [43, 54, 117].

To assess the validity of the linear unloading simplification, let us consider the rolled plate studied in section 2.2.2.2. The linear unloading hypothesis is tested at two locations: at the mid-span of the plate and at the section where the loading is applied, with an imposed stroke is $y_s = \pm\ 9.5\ mm$. Both force-displacement diagrams are represented in Figure 3.9.

A linear unloading path is represented at the final position of each cycle. Although it can be seen that the experimental unloading path follows a non-linear trajectory, for reshaping we are only interested in two points: where to stop the loading curve and the final distortion value in the part. Therefore, by using the linear approximation of the unloading path, both points can be tracked easily.

Further insight on the linear unloading hypothesis can be found in literature [117], where the authors state that when a complete unloading is performed after applying a bending moment M to a beam, if unloading does not cause reverse yielding, then the unloading process is equivalent to the elastic effect caused by applying $-M$ to the beam. Therefore, the key is to not produce reverse yielding. This phenomenon is present in metal sheet forming [9], very common in the automotive industry for instance. However, large structural elements in the aircraft industry can

[2]Not to be confused with the stress-strain diagram, where unloading is linear with slope equal to the Young's modulus.

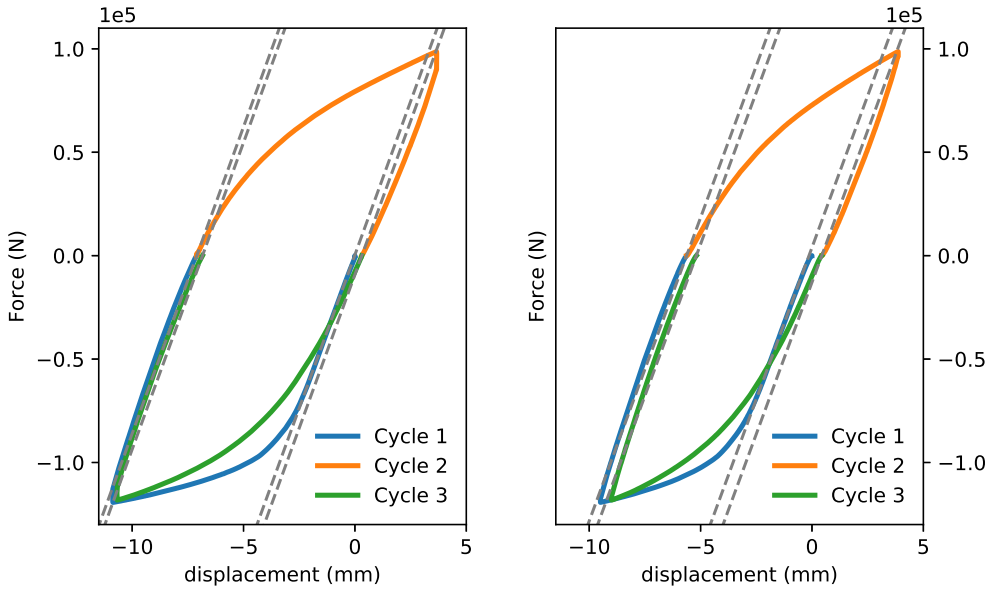

Figure 3.9: Testing the linear unloading hypothesis. Force versus displacement diagram for the rectangular rolled plate (specimen L2). Experimental curves (solid lines) vs linear unloading path (dashed lines). (a) At midspan $L = 100$ mm and (b) At the section where the load is applied $L = 70$ mm (see Figure 2.5a).

be considered as thick walled, and the levels of strain under reshaping are less likely to develop reverse yielding. Therefore, the unloading path can be approximated to a linear behaviour.

Table 3.1: Final displacement for a given stroke y_s during reshaping configurations P1 and P5: comparison between the non-linear (FEM) and linear unloading path (LU).

Parameter / Configuration	P1			P5			
Stroke y_s	12	14	16	15	17.015	20	mm
Displacement FEM	-1.280	-2.182	-3.268	3.171	5.376	8.758	mm
Displacement LU	-1.177	-2.051	-3.107	3.095	5.051	8.631	mm
Relative Error E_{rel}	8.1	6.0	4.9	2.4	6.0	1.5	%

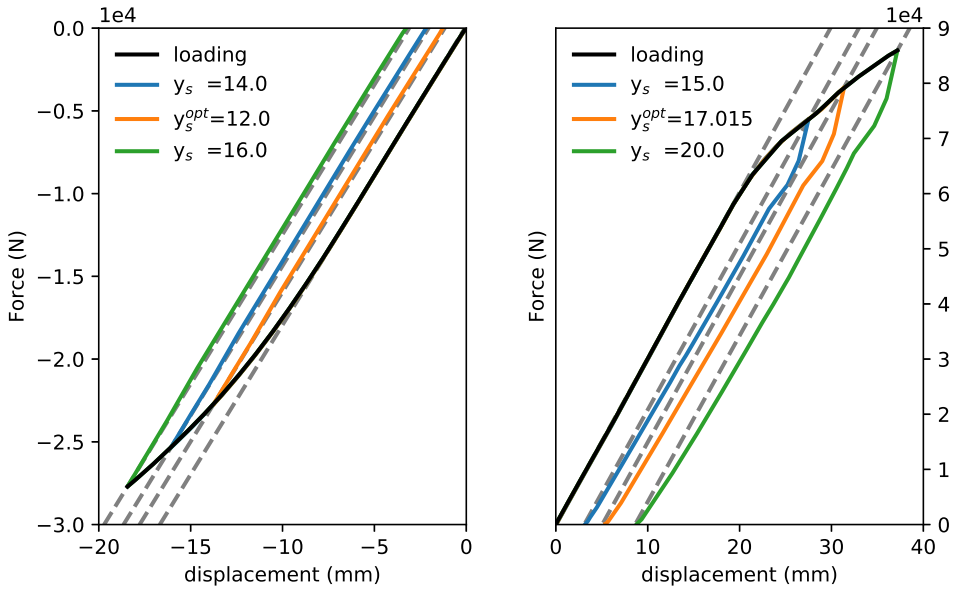

(a) (b)

Figure 3.10: T shaped beam. Force vs displacement diagram: numerical curves (solid lines) vs linear unloading path (grey dashed lines). (a) Reshaping configuration P1 (RS) and (b) Reshaping configuration P5 (RS).

To further assess the validity of the linear unloading simplification, we consider now the T-shaped beam. The force-displacement diagram is generated for reshaping configurations P1 and P5. These are represented in Figures 3.10a and 3.10b, respectively. Linear unloading is represented for different stroke values.

As it can be seen, the linear unloading path approximation is valid for both reshaping configurations. While P1 configuration follows naturally a linear path, P5 unloading is clearly non-linear. However, both the linear and the non-linear unloading path end nearly at same point. This is crucial, as the end point can be used to determine the distorted value after unloading.

In terms of relative error E_{rel}, the linear unloading hypothesis causes an error of less than 10% for the final displacement respect to the FEM result, which proves to be a good approximation for industrial applications. The corresponding values for configuration P1 and P5 are summarized in Table 3.1. Finally, if both configu-

rations are considered as the extreme values for the interval $M_o \in [5, 10]$ mm in the initial distortion diagram (see Figure 3.5a), it is expected that the linear unloading hypothesis remains valid for intermediate values as well.

3.3.2 Reshaping offset calibration

In this section, we propose a strategy, based on the linear unloading simplification, in order to calibrate the reshaping offset from experimental force-displacement measures.

Figure 3.11 summarizes the process for configurations P1 and P5. Since we do not have experimental measures, we shall assume the reshaping diagram (with residual stresses) as the ground truth for comparison.

First, we compute the reshaping diagram under a residual stress free state. This is defined as the *off-line* stage for our problem, where all the numerical simulations are performed. Now we start loading the part by increasing the stroke (controlled displacement). We also record the applied force by the press head. By applying the linear unloading simplification, we obtain an approximation of the distortion after unloading. This is depicted in green in Figure 3.11.

The actual reshaping diagram is a priori unknown, in principle, it can only be obtained by performing loading (apply stroke) then unloading (measure distortion) cycles. This trial and error procedure describes the industrial practice today and it is undesired.

Instead, we propose to use force-displacement measures, which are rather standard in bending operations, in combination with a linear unloading path hypothesis, to derive an approximation of the experimental reshaping diagram. This second step is referred as the *on-line* stage.

Once we enter the zone B of the reshaping diagram, we can start noticing the difference in response between the residual stress free diagram and the experimental approximation. As soon as the difference becomes steady, the offset can be determined. From the knowledge of the offset, the optimal stroke can be approximated as: $y_s^{\text{opt}} = y_s^{\text{opt,RSF}} + \Delta y_s$.

Following with configurations P1 and P5, Δy_s is presented in Table 3.2.As a result, the applied stroke y_s^{opt} differs to the actual optimum value $y_s^{opt,RS}$ in less than 6%. This gap is caused by the use of the linear unloading hypothesis to determine the offset. On the other hand, thanks to this hypothesis, the operator can retrieve

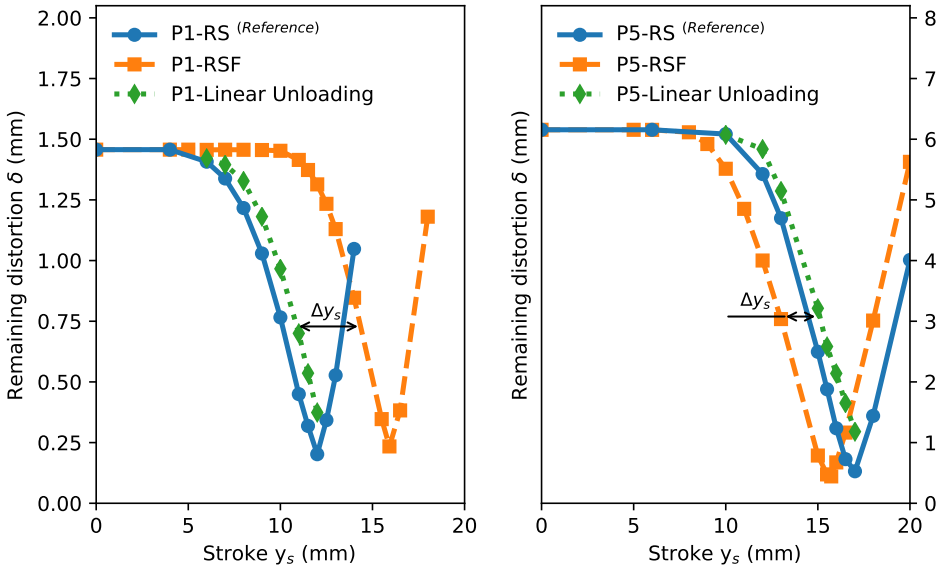

(a) (b)

Figure 3.11: T shaped beam. Remaining distortion vs Stroke diagram: Offset calculation. (a) Reshaping configuration P1 and (b) Reshaping configuration P5.

Table 3.2: Calculation of the offset Δy_s and error estimation for the applied stroke y_s^{opt}.

Parameter / Configuration	P1	P5	
Optimum stroke (RS) $y_s^{opt,RS}$	12	17.015	mm
Optimum stroke (RSF) $y_s^{opt,RSF}$	15.920	15.725	mm
Offset Δy_s	-3.498	2.158	mm
Applied stroke y_s^{opt}	12.422	17.883	mm
Relative Error E_{rel}	-3.5	-5.1	%

nearly the optimal stroke in a single guess (no unloading).

The updated RSF curve after adding the offset Δy_s is depicted in Figure 3.12 (in dashed lines). While y_s^{opt} is determined in the synthetic reshaping diagram, when used in the real system (with residual stresses), the obtained remaining distortion $\delta\left(y_s^{opt}\right)$ differs respect to the optimal value $\delta\left(y_s^{opt,RS}\right)$, as shown in the detailed

window for each Figure. To quantify the mismatch, the relative error E_{rel} respect to the distortion reduction is used. Thus, the distortion reduction is defined as the repair rate done after applying a selected value of stroke $\delta(y_s)$ respect to initial distortion in the current step $\delta|_{y_s=0}$, see Eq.(3.2). Therefore, E_{rel} is obtained by normalizing the difference between the optimal and the obtained distortion reduction respect to the optimal distortion reduction, as described in Eq.(3.3). Note that the optimal distortion reduction corresponds to the maximum reparation rate achievable in the current reshaping step. As result, an error in the range of 10-15% is obtained at the end of the process for configurations P1 and P5, respectively. All the values of the reshaping operation are summarized in Table 3.3.

$$\text{distortion reduction} = \left(1 - \frac{\delta\left(y_s\right)}{\delta|_{y_s=0}}\right) \times 100\,(\%) \tag{3.2}$$

$$E_{rel} = \left(1 - \frac{\text{Obtained distortion reduction}}{\text{Optimal distortion reduction}}\right) \times 100\,(\%) \tag{3.3}$$

To sum up, the advantage of using the proposed approach is that we can overcome the uncertainties related to the residual stresses present on the part, reduce the computational cost by neglecting the previous manufacturing steps and focus our efforts on the simulation of reshaping under the RSF hypothesis. Then, by using the LU path, it is not required to interrupt the repairing operation any more by performing any unnecessary unloading steps in order to calibrate the difference in response respect to the simulations obtained before. Now, only by tracking the force and displacement evolution during the process, it is possible to estimate an upper boundary of the remaining distortion δ as a function of the given stroke y_s. In other words, it is possible to reproduce an approximation of the reshaping diagrams with residual stresses obtained previously in Figure 3.7 to assist the operator in the task of repairing a part.

3.4 Conclusions

In this chapter, we have presented the reshaping diagrams as a tool for simulation assisted bending straightening. With this tool, it is possible to select in advance the stroke to apply in order to minimize distortion. Diagrams are generated in a two step procedure: *i*) *off-line* stage (numerical) and *ii*) *on-line* stage (experimental). The off-line stage performs the reshaping simulation by considering a distorted part free of

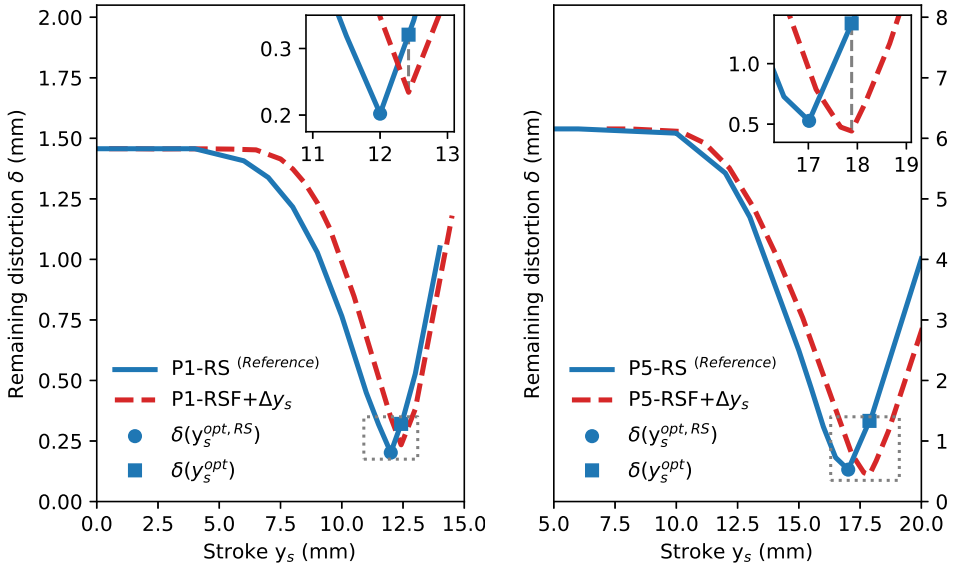

(a) (b)

Figure 3.12: T shaped beam. Reshaping diagram: optimal final distortion $\delta(y_s^{opt,RS})$ vs obtained final distortion $\delta(y_s^{opt})$. (a) Reshaping configuration P1 and (b) Reshaping configuration P5.

Table 3.3: Distortion reduction and error estimation after reshaping.

Parameter / Configuration	P1	P5	
Initial distortion δ_0	1.457	6.165	mm
Optimal final distortion (RS) $\delta(y_s^{opt,RS})$	0.202	0.527	mm
Obtained final distortion (RS) $\delta(y_s^{opt})$	0.321	1.332	mm
Optimal distortion reduction (RS)	86.1	91.5	%
Obtained distortion reduction (RS)	78.0	78.4	%
Relative Error E_{rel}	9.5	14.3	%

residual stresses and obtains the RSF-diagram. This simplification is able to describe the distortion evolution of the structure compared to the residual stress case with an offset. The on-line stage uses a linear unloading path to estimate the offset. This task is done by tracking the force and displacement while the reshaping operation in

the real part is performed. Once the offset is known, the RSF-diagram is updated and an approximation to the optimum parameters is found. The relative error expected by using the reshaping diagram is around 10%. From the computational point of view, the generation of the RSF-diagram is a very simple and inexpensive calculation that allows focusing on reshaping simulations only instead of the whole manufacturing chain, saving time from modelling and simulation. Regarding the linear unloading path to determine the offset, it avoids interrupting the loading process during reshaping. Additionally, force and displacement are quantities that can be easily obtained in a daily industrial environment. As a limitation, it should be used only for thick-walled components.

The proposed approach reduces the gap between the theoretical outputs of numerical simulations and the practical needs at industrial level. The obtained results also opens the door to study reshaping under a Reduced Order Model (ROM) framework, because it is known how to parametrize shape [58], i.e the initial distorted geometry can be introduced as an extra parameter, while the task to parametrize RS is an open field yet. The next chapter focuses on the development of a ROM for the reshaping problem with the aim to explore in a virtual environment the influence of different parameters involved during the operation.

Chapter 4

Bending straightening: a multiparametric ROM study

There is a need at an industrial level to solve the problem of post-machining distortion mitigation with the support of numerical simulation tools. Following this line, the reshaping diagram acts as a bridge between the simulations performed by the stress engineers and the operators at the shop floor, which are the responsible to repair a part. However, to fully deploy the capabilities of the reshaping diagrams in an industrial environment, it is required to explore beforehand the input parameter space to construct a solution dictionary of a reshaping diagrams family so that, the operator can obtain a real-time response based on the tailor repair's needs. Both requirements oblige to launch a multi-parametric analysis under a Model Order Reduction (MOR) framework. Although a complete reshaping process consists of a sequence of elementary operations, the present chapter focuses on bending straightening in one single reshaping step. Different process parameters are simulated by applying the Sparse Subspace Learning method (SSL). By using the MOR approach, new insights for the distortion mitigation via plastic bending can be explored that will help to understand the open problem of reshaping.

Contents

4.1 Introduction **53**

4.2 A brief state-of-the-art on model order reduction **54**

4.2.1 The need of model order reduction 54
4.2.2 Fundamentals of model order reduction 55
4.2.3 Selected MOR techniques 59
4.2.4 MOR applied to manufacturing problems 69
4.3 Multi-parametric bending straightening 71
4.3.1 Process model and parameters 72
4.3.2 Reshaping under the SSL formulation 74
4.3.3 Problem setup 74
4.4 Results and discussion 76
4.5 Conclusions 80

4.1 Introduction

In chapter 3, the influence of residual stresses for reshaping was analysed. Thanks to that, the Residual Stress Free (RSF) hypothesis was proposed, which allowed us to put aside for a moment the unknown Residual Stresses (RS) developed during the manufacturing process and invest the simulation resources on the resolution of the bending straightening operation. As a result, the the reshaping diagram was obtained and presented as a tool to assist the operator in the decision-making to select the optimum parameters to mitigate distortion. However, the construction of the reshaping diagram still suffers form two main drawbacks: *i*) the initial distortion δ_0 is a priori unknown and it needs to be provided as the main input. Consequently, without that information, the reshaping diagram can not be calculated. *ii*) The strategy followed to obtain the reshaping diagram was a manual procedure, so that multiple points were chosen in a unstructured manner in order to construct the curve. Therefore, there is a need to use a more systematic way such that the reshaping diagram generation can be scalable and automatized.

Given the described limitations, the requirement of running multiple reshaping simulations together with a real-time response suggests to launch a multiparametric analysis under a Model Order Reduction (MOR) framework [27]. A quick and a reliable simulation response are key ingredients to fulfill in order to improve the applicability of the reshaping diagrams in a shop-floor level.

Although the corrective stage of reshaping is an iterative operation, this chapter deals only with bending straightening done as a single step. This abstraction allows us to isolate the problem with the aim to understand the influence of different parameters on the reshaping operation as an essential step for ensuring a reliable repairing process. The rest of this chapter is organized as follows: in section 4.2, a brief review of the state of the art in the field of MOR is given. Here, the motivation and the fundamentals of reduced models together with five representative techniques are introduced. Special interest is given to the application of MOR to manufacturing processes and, based on the non-intrusiveness and the ability to handle the non-linearities present during reshaping, the Sparse Subspace Learning method is chosen to develop the multi-parametric study. Then, in section 4.3, the SSL formulation applied to reshaping is explained together with the problem set-up used for a T shaped beam geometry. Next, the results of the multi-parametric ROM study are analysed in section 4.4 and finally, the obtained conclusions are addressed.

4.2 A brief state-of-the-art on model order reduction

4.2.1 The need of model order reduction

Traditional mesh based discretization techniques (e.g. Finite Elements, Finite Differences, Finite Volume and Spectral Methods) have experienced an important development in the last decades in parallel to the increment on the computer resources availability and the research efforts of the numerical and scientific computing community [96]. Thanks to its applicability and broad use, Full-Order Models (FOM), also referred as High-fidelity models (HFM), are essential to design safer structures, study complex fluid phenomena and develop any type of device based on physical laws. However, in spite of the current developments, traditional techniques present the following limitations:

- *Multi-parametric analysis*: as soon as the model incorporates multiple parameters, FOM are the favourite victim of the so-called *curse of dimensionality*, a term introduced by Bellman [12], that relates an increment of number of parameters (dimensions), with an exponential growth of the computational cost required to solve the problem. Therefore, the use of brute force as a strategy to tackle this type of problems is not a feasible option.

- *Multi-scale problems*: when a model combines multiple scales, for example, the different scales available in a turbulent flow [33], the smallest length scale leads to a mesh refinement with its associated computational cost increment. A strategy to handle the macro-micro lengths is to use homogenization techniques, however, they become inefficient with the presence of time-dependency, non-linearities and multiple-parameters [1].

- *Uncertainty Quantification*: statistical treatment for parameter estimation via Monte Carlo Sampling (MCS) and its variants, requires an important amount of repetitive executions. An elevated number of simulations K are needed to obtain accurate predictions. In addition, the method presents a slow convergence rate of $1/\sqrt{K}$. When the model is expensive to evaluate, MCS applicability is limited [115]. A similar problematic is experienced for variational/sequential data assimilation or Bayesian inverse problems [64].

- *Many-query problems*: in design, control or optimization, repeated evaluations of the problem are required for different parameters values [57]. Under this

context, the use of a FOM means massive computer resources in terms of amount of CPU time and data storage, leading to an unaffordable scenario.

- *(Quasi) real-time solution*: depending on the application, different feedback rates are required. For example, for augmented reality, 25 Hz ensure the visual continuity of an image in movement, while for haptic controllers, 0.5-1 KHz are needed to provide a response in terms of force to the device [31]. In both cases, the mentioned rates represent a challenge because it means that one single simulation should be achieved in the range of milliseconds.

After describing the dimensionality problem, Bellman encourages us to seek for more advanced techniques to overcome this issue [12]. Here is when Model Order Reduction (MOR) comes into scene, as an alternative to deal efficiently with the open challenges in science and engineering [4].

4.2.2 Fundamentals of model order reduction

The underlying idea behind MOR is that, to properly describe a model, from all the available information only a little amount is relevant[1] [26]. Keeping this hint in mind, we can define MOR as the group of numerical techniques that alleviates the computational cost respect to high-fidelity methods by solving the problem in a lower dimensional space. As a result, a similar response in terms of input/output behaviour is obtained. The reduced model should meet three main requirements: *i)* to capture the principal features of the FOM, *ii)* to satisfy the accuracy in terms of error estimation and *iii)* to preserve the basic properties of the original system as consistency, stability and convergence [94]. For an historical review of the development of MOR techniques, the interested reader is referred to Schilders et. al, 2008 [96].

FOM are based on Partial Differential Equations (PDEs). They are the mathematical basis behind any physical model used in Computational Mechanics and we want to apply MOR methods to them. In a general context, we define an open bounded domain $\Omega \subset \mathbb{R}^{d\leq 3}$ and a parameter domain $\mathcal{P} \in \mathbb{R}^p$. In this setting, the physical space variable is denoted as $\boldsymbol{x} \in \Omega$ and normally, the problem is solved for a fixed set of p parameters $\boldsymbol{\mu} = [\mu_1, \ldots, \mu_p]^T \in \mathcal{P}$. When each parameter μ_i varies

[1] This notion goes in line with the Pareto principle, which states that for many events, roughly 80% of the effects come from 20% of the causes.

inside of a given interval $\mu_i \in [\mu_{i_{min}}, \mu_{i_{max}}]$, and we want to find the solution of the problem for all parameters, we refer to a *parametric PDEs* [29]. Therefore, we can describe a parametric PDE of the form:

$$\mathcal{L}u\left(\boldsymbol{x};\boldsymbol{\mu}\right) + \mathcal{N}\left(u\left(\boldsymbol{x};\boldsymbol{\mu}\right)\right) = g \tag{4.1}$$

To obtain the weak form, we multiply Equation (4.1) by a smooth test function $v \in V$ and after integrating over Ω, the result leads to the following problem formulation: given $f \in V$, find $u(\boldsymbol{x};\boldsymbol{\mu}) \in V$ such that:

$$\begin{aligned} \int_\Omega v\left(\mathcal{L}u\left(\boldsymbol{x};\boldsymbol{\mu}\right) + \mathcal{N}\left(u\left(\boldsymbol{x};\boldsymbol{\mu}\right)\right)\right) d\Omega &= \int_\Omega v g d\Omega, \ \forall v \in V \\ \langle v, \mathcal{L}u\left(\boldsymbol{x};\boldsymbol{\mu}\right)\rangle + \langle v, \mathcal{N}\left(u\left(\boldsymbol{x};\boldsymbol{\mu}\right)\right)\rangle &= \langle v, g\rangle \\ a\left(v, u;\boldsymbol{\mu}\right) &= l\left(v\right) \end{aligned} \tag{4.2}$$

where $u(\boldsymbol{x};\boldsymbol{\mu})$ corresponds to the solution Equation (4.1) and V is its associated space. $\mathcal{L} : V \times W \to X$ and $\mathcal{N} : V \times W \to X$ are linear and non-linear partial differential operators, respectively, where (V, W, X) is a triple of Banach space. $\langle \cdot\ ,\ \cdot \rangle$ denotes the inner product in $L^2(\Omega)$. Bilinear and linear operator are defined as $a(\cdot\ ,\ \cdot) : V \times V \to \mathbb{R}$ and $l(\cdot) : V \to \mathbb{R}$, respectively. The parametric dependence of the solution u is expressed by the semicolon through the formulation. Although no formally written, it is assumed that suitable boundary conditions to Equation (4.1) are prescribed.

After performing a spatial discretization, Equation (4.2) leads to a system of Ordinary Differential Equations (ODEs):

$$\boldsymbol{A}\boldsymbol{u}\left(\boldsymbol{x};\boldsymbol{\mu}\right) + f\left(\boldsymbol{u}\left(\boldsymbol{x};\boldsymbol{\mu}\right);\boldsymbol{\mu}\right) = \boldsymbol{0} \tag{4.3}$$

where the discrete state variable $\boldsymbol{u}(\boldsymbol{x};\boldsymbol{\mu}) = [u_1(\boldsymbol{x};\boldsymbol{\mu}), \ldots, u_n(\boldsymbol{x};\boldsymbol{\mu})]^T$ is referred as the *solution vector*. The matrix $\boldsymbol{A} \in \mathbb{R}^{n\times n}$ comes from the linear term $\mathcal{L}u$ whereas $f\left(\boldsymbol{u}\left(\boldsymbol{x};\boldsymbol{\mu}\right);\boldsymbol{\mu}\right) \in \mathbb{R}^n$ is the result of combining the non-linear term $\mathcal{N}(u)$ with the source term g and the prescribed boundary conditions. Please note that $f(\cdot\ ;\ \cdot)$ is non-linear too.

The resulting dimension of the full order problem for $\boldsymbol{u}(\boldsymbol{x};\boldsymbol{\mu})$ is n (i.e. $dim(\boldsymbol{u}) = n$). In MOR, by exploiting the properties of anisotropy and holomorphy, we seek for an approximation of the solution $\boldsymbol{u}(\boldsymbol{x};\boldsymbol{\mu}) \approx \boldsymbol{u}^r$ that allows the separation of the physical space $\boldsymbol{x}$ and parametric space $\boldsymbol{\mu}$, giving as a result the form:

$$\boldsymbol{u}\left(\boldsymbol{x};\boldsymbol{\mu}\right) \approx \boldsymbol{u}^r = \sum_{k=1}^{r} v_k\left(\boldsymbol{x}\right)\psi_k\left(\boldsymbol{\mu}\right) \tag{4.4}$$

where $\{v_1, \cdots, v_r\}$ are functions of $\boldsymbol{x}$ living in the solution space V and $\{\psi_1, \cdots, \psi_r\}$ are functions of $\boldsymbol{\mu}$ with values in $\mathbb{R}$ or $\mathbb{C}$. As a consequence, the following dimensionality reduction is obtained $dim(\boldsymbol{u}^r) = r \ll n$. For a deeper description of parametric PDEs and the mathematical properties used to obtain the reduced approximation, the interested reader is referred to Cohen and DeVore 2015 [29].

Thanks to the reduction in dimensionality, important savings in terms of computation cost are achieved by using the so called *off-line/on-line* strategy [2]. Within this approach, the workload is divided in two marked steps. The *off-line* stage corresponds to an exploration of the solution space by solving the full order problem in some previously defined points. We refer to these precomputed solutions as *snapshots*. The off-line stage is only performed once, it comes at an accepted computational cost and here is where the approximation basis are calculated. Then, depending on the selected MOR technique (see section 4.2.3), the solution can be reconstructed in advance, leaving to the *on-line* stage as a post-processing operation where the solution is available for any value of parameters $\boldsymbol{\mu}$, otherwise, a small system of equations must be solved each time in order to have access to the reduced model. A graphical comparison between the involved computational cost for the full and reduced order model is shown in Figure 4.1. By assuming a linear behaviour for a single computation of the parametric solution, the investment done during the off-line stage is fully recovered when the number of outputs required for the ROM is bigger than the break-even point k^* [49].

4.2.2.1 Classification of MOR

In a general way, MOR techniques can be classified attending the following criteria:

- Based on the manner the reduced problem is constructed, we can define MOR methods as two big groups:*a priori* and *a posteriori*. We refer to *a posteriori* methods when the reduced model is built only after a relatively low number of snapshots are performed and explored. On the other hand, the *a priori* methods refer to the construction of the reduced problem in a progressive manner (i.e. during the solution of the problem).

- When the reduced model is obtained by projecting the full-order problem into a subspace, we define the so-called *projection-based* methods. Alternatively, if the reduction is generated by interpolation, we classify them as *interpolation-*

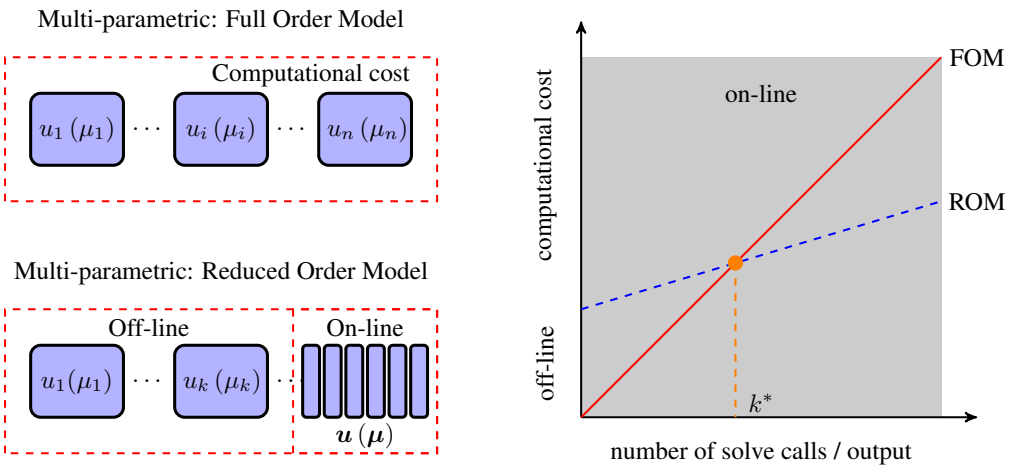

Figure 4.1: Computational cost comparison between FOM and ROM. Adapted from [49, 92]

based method. Projection-based MOR preserves the structure of the full-order problem and this property allows deriving theoretic error bounds and error estimates [13]. On the other hand, interpolation methods play an important roll as a strategy to solve efficiently non-linearities [25].

- *Intrusiveness* is referred to the coding strategy used to implement the MOR technique. A method is considered as *intrusive* when it is required to re-write the discretization of PDE's in a tailor-made manner to solve the problem. On the other hand, we talk about a *non-intrusive* method when there is no manipulation of the solver to compute the solution, i.e. a commercial FE software is used as a black-box to produce the snapshots that will be used to construct the reduced problem.

- A method can be considered *adaptive* when, while the construction of the basis functions is performed, adds a function n which depends on the $n-1$ previously obtained. The enrichment of the basis is typically performed with a greedy strategy. On the contrary, a *non-adaptive* method is one that, for a given n, selects the basis of functions of Equation (4.4), based on some knowledge of the solution. As a general rule, better results can be expected from an adaptive technique [17].

4.2.3 Selected MOR techniques

Down below, five selected MOR techniques are described. They are representative attending at the previously provided classification. For each method, a brief reference at when it was introduced is provided and emphasis is given to the way the reduction is obtained. Then, an overview of MOR applied to manufacturing process is provided and by analysing the range of applicability and limitations for each technique, a decision is made to chose the most suitable candidate to solve the problem of reshaping.

4.2.3.1 Proper Orthogonal Decomposition

The Proper Orthogonal Decomposition (POD) is an *a posteriori* model order reduction technique. It was first introduced by Lumley in 1967 [61] with the aim to find coherent structures on a turbulent flow. In statistics, POD is known as Principal Component Analysis (PCA) [113]. The main idea of the method is to perform the following decomposition:

$$\boldsymbol{u}\left(\boldsymbol{x};\boldsymbol{\mu}\right) \approx \boldsymbol{u}^r = \sum_{k=1}^{r} \alpha_k\left(\boldsymbol{\mu}\right) \Phi_k\left(\boldsymbol{x}\right) = \boldsymbol{\Phi}_r \boldsymbol{\alpha} \tag{4.5}$$

where $\Phi_k(\boldsymbol{x})$ and $\alpha_k(\boldsymbol{\mu})$ correspond to the POD basis, normally referred as *spatial modes*, and the parameters coefficients, respectively.

The method starts with the sampling of the parametric space. This task is done by taking m snapshots of the full-order problem. If each snapshot is stored as a column vector of size $1 \times n$ and grouped side by side, the snapshot matrix $\mathbf{S}$ of size $m \times n$ is obtained. In order to normalize the data, it is a common practice to update each column of $\mathbf{S}$ by removing the mean value of that column [24].

The second step consists on the basis generation. It is calculated after performing a Singular Value Decomposition (SVD) over the snapshot matrix, so that $\mathbf{S} = \mathbf{L}\boldsymbol{\Sigma}\mathbf{R}^T$. The resulting POD basis corresponds to a low-rank approximation of $\boldsymbol{\Sigma}$ and it is formed by the orthonormal set $\boldsymbol{\Phi}_r = \{\Phi_1 \cdots \Phi_r\}$ (with $r \leq m \ll n$), which is composed by the squared of the most energetic eigenvalues of $\boldsymbol{\Sigma}$ placed in decreasing order (i.e $\Phi_i = \sigma_i^2$).

With the obtained basis, a POD subspace is generated, which is defined as $S_{POD} \coloneqq \text{span}\{\Phi_{1 \leq i \leq r}\} \subset V$, and its dimension is $\dim\left(S_{POD}\right) = r \ll \dim\left(V\right)$. Finally, the parameters coefficients $\alpha_k(\boldsymbol{\mu})$ are calculated by performing a Galerkin

projection of the full-order problem into S_{POD}. In that way, the reduced model is fully defined.

$$\sum_{k=1}^{r} a\left(\Phi_j, \Phi_k; \boldsymbol{\mu}\right) \alpha_k\left(\boldsymbol{\mu}\right) = l\left(\Phi_j\right), \ \forall \Phi_j \in S_{POD} \tag{4.6}$$

POD is a popular method in the MOR community. It has been successfully applied to viscoelastic fluids [48], structural mechanics [16], design of magneto resonance imaging scanners [98] and control problems [10, 84]. However, the method presents three main drawbacks: *i)* to explore the parametric space, POD does not define any strategy, therefore, this step relies on the experience of the person who is performing the study. *ii)* the POD basis can only capture the behaviour present in the snapshots. If there is a lack of information during the sampling step, the basis generated will not be accurate enough to provide a good approximation of the problem. *iii)* Although POD is the standard method to handle non-linear problems, as all MOR projection-based techniques, the computational savings that could be gained with an equivalent linear problem, in terms of size reduction, are lost. In order to explain this drawback, lets apply the Galerkin projection of the POD basis $\boldsymbol{\Phi}_r$ to Equation (4.3) and replace the field of interest by the POD approximation of Equation (4.5). As a result, the following linear and non-linear terms are obtained:

$$\underbrace{\boldsymbol{\Phi}_r^T \boldsymbol{A} \boldsymbol{\Phi}_r \boldsymbol{\alpha}}_{\text{linear}} + \underbrace{\boldsymbol{\Phi}_r^T f\left(\boldsymbol{\Phi}_r \boldsymbol{\alpha}\right)}_{\text{non-linear}} = \mathbf{0} \tag{4.7}$$

While a fully reduction of the linear term is possible by pre-computing $\boldsymbol{A}_r = \boldsymbol{\Phi}_r^T \boldsymbol{A} \boldsymbol{\Phi}_r$ only (as represented in Figure 4.2a), for the non-linear term, the high dimensionality remains inside of the reduced model. This problem is caused by the evaluation of the non-linear term in the low dimensional embedded space. In other words, each time the parameters coefficient $\alpha_k(\boldsymbol{\mu})$ is updated, a re-evaluation of the non-linear term $f(\boldsymbol{\Phi}_r \boldsymbol{\alpha})$ and the inner product with $\boldsymbol{\Phi}_r^T$ is required too, as shown in Figure 4.2b.

4.2.3.2 Reduced Basis

The Reduced Basis (RB) Method is a *adaptive projection-based* MOR technique for parametric problems. The current framework was formally developed by Prud'homme et al., 2002 [79]. The method tackles the sampling limitation of POD by proposing

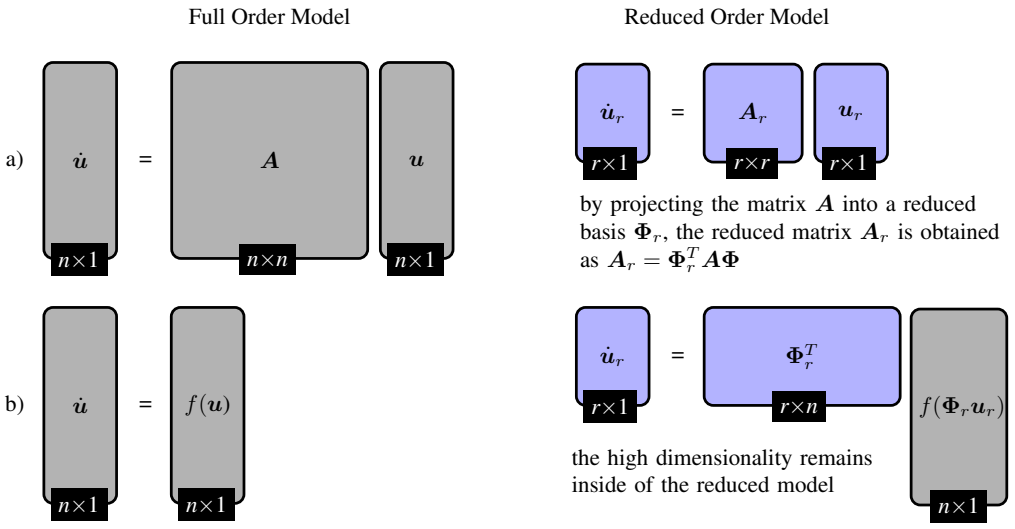

Figure 4.2: Projection based Model Order Reduction applied to linear (a) and non-linear (b) problems. Adapted from [13]

an iterative strategy based on a posteriori error estimator [81]. In that way, instead of evaluating n_s snapshots to extract only N modes and construct the projection base, such that $N \leq n_s$, RB selects exactly N sampling points with the aim to compute its snapshots and build the projection subspace efficiently.

The main assumption of the method is that the parametric solution manifold $\mathcal{M}$, defined as the set of solutions generated when the input parameters $\boldsymbol{\mu}$ are varied along the whole parameter domain $\mathcal{P}$, $\mathcal{M} = \{\boldsymbol{u}(\boldsymbol{x};\boldsymbol{\mu})|\boldsymbol{\mu} \in \mathcal{P}\}$, can be approximated by a Petrov-Galerkin projection into a low N-dimensional space V_N, the so called *Reduced Basis* space.

In a glance, the method is done in the following form: during the off-line stage, the greedy sampling strategy and the construction of the RB are performed iteratively. Then, the reduced model is obtained by calculating an algebraic system in the on-line stage allowing a fast evaluation of any parameter value $\boldsymbol{\mu} \in \mathcal{P}$.

The problem separability, referred as *affine*, is based on the parameter dependence and it is expressed for the bilinear form $a(\cdot\,,\cdot)$ and the linear form $l(\cdot)$ of

Equation (4.2) as:

$$a\left(u,v;\boldsymbol{\mu}\right)=\sum_{q=1}^{Q}\sigma^{q}\left(\boldsymbol{\mu}\right)a^{q}\left(u,v\right),\ \forall u,v\in V,\ \boldsymbol{\mu}\in\mathcal{P} \tag{4.8}$$

$$l\left(v;\boldsymbol{\mu}\right)=\sum_{q=1}^{Q}\sigma^{q}\left(\boldsymbol{\mu}\right)l^{q}\left(v\right),\ \forall v\in V,\ \boldsymbol{\mu}\in\mathcal{P} \tag{4.9}$$

where $\sigma^q : \mathcal{P} \to \mathbb{R}$ and $q = 1, \ldots, Q$ are parameter-dependent functions and $a^q : V \times V \to \mathbb{R}$ and $l^q : V \to \mathbb{R}$ are parameter-independent forms.

The (weak) greddy algorithm is applied over a prescribed parameters training set $S_{train} \subset \mathcal{P}$ to construct iteratively the projection subspace. For example, in a generic iteration n i.e. $1 \leq n \leq N-1$ with a given sample set $S_n = \{\boldsymbol{\mu}_1, \ldots, \boldsymbol{\mu}_n\}$, and its associated Lagrangian reduced basis $\boldsymbol{\zeta}_n = \{\zeta_1, \ldots, \zeta_n\}$, that generates the subspace $V_n = \text{span}\{\zeta_{1 \leq i \leq n}\}$, a new basis is added by fulfilling an optimally criterion based on the *a-posteriori error estimator* $\Delta_n(\boldsymbol{\mu})$. This feature is used to approximate the error $\|u(\boldsymbol{\mu}) - u_n(\boldsymbol{\mu})\|$ and it allows choosing carefully the next sampling point $\boldsymbol{\mu}_{n+1}$ by solving:

$$\boldsymbol{\mu}_{n+1} = \arg \max_{\boldsymbol{\mu} \in S_{train}} \Delta_n\left(\boldsymbol{\mu}\right) \tag{4.10}$$

In other words, the retained snapshot at each step corresponds to the worst approximation performed by the current RB solution obtained at V_n. As a consequence, the generated basis is hierarchical (i.e. $\boldsymbol{\zeta}_n \subset \boldsymbol{\zeta}_m$, for $n \leq m$). The evaluation of the a posteriori error estimator is considered cheap in terms of computational cost. In addition, the greedy procedure is relatively fast as only N high-dimensional snapshot are calculated, instead of the pre-computing the whole parametric sampling set, as done by POD.

Once the N-dimensional reduced basis is obtained, the solution approximation $u_N(\boldsymbol{x};\boldsymbol{\mu}) \in V_N$ is computed as the following linear combination:

$$u_N\left(\boldsymbol{x};\boldsymbol{\mu}\right)=\sum_{i=1}^{N}u_{N_i}\left(\boldsymbol{x};\boldsymbol{\mu}\right)\zeta_i \tag{4.11}$$

where $\boldsymbol{u}_N(\boldsymbol{x};\boldsymbol{\mu}) = [u_{N_1}(\boldsymbol{x};\boldsymbol{\mu}), \ldots, u_{N_N}(\boldsymbol{x};\boldsymbol{\mu})] \in \mathbb{R}^N$ corresponds to the RB coefficients. These coefficients are unknown and they are calculated by solving the N equations after imposing N independent conditions. In that way, the ROM is fully defined.

Regarding the parameter training set S_{train}, it should be noticed that its selection is non-trivial. On one hand, the subset should be small enough so that the greedy algorithm remains effective. On the other hand, the sample should be large enough to represent properly the parametric domain in order to avoid missing relevant information. In practice, a Monte Carlo sampling is chosen so that S_{train} can fulfil a trade-off between both conditions [81].

The RB formulation is well suited for parametric linear, coercive and affinely decomposed cases (e.g. elliptic and parabolic problems) [73]. In the presence of simple non-linearities, as nonlinear advection or nonlinear diffusion problems, is needed to rewrite the equations as a multi-linear form. However, in the presence of general non-linearities, the Empirical Interpolation Method (EIM) or its discrete version, the Discrete Empirical Interpolation Method (DEIM) are required to circumvent the problem by using interpolation. The DEIM method is explained below in section 4.2.3.4. For a more detailed discussion about the limitations and further directions of the RB method, the interested reader is referred to Haasdonk 2016 [49].

4.2.3.3 Proper Generalized Decomposition

The Proper Generalized Decomposition (PGD) is an *a priori* model order reduction technique, due to the construction of the reduced basis is done progressively and without previous knowldege of the solution, in contrast to the POD snapshopts. The seminal work was presented by Ammar et al., in 2006 [4] when trying to solve the high-dimensional modelling of non-Newtonian fluids. The method is based on two main ideas: *i)* the separated representation of variables, i.e. parameters, loads, geometry, even boundary conditions can be treated as separated and independent extra coordinates of the problem and *ii)* the separated problem formulation. Both ideas can be considered as a generalization of the time-space separation of the LATIN (LArge Time INcrement) method proposed by Ladevèze in 1985 [56]. As a consequence, the method approximates the field of interest as a finite sum of the product of the coordinates as:

$$\boldsymbol{u}\left(\boldsymbol{x};\boldsymbol{\mu}\right) \approx \boldsymbol{u}^r = \sum_{i=1}^{r} F_x^i\left(\boldsymbol{x}\right) \cdot F_{\mu_1}^i\left(\mu_1\right) \cdot \ldots \cdot F_{\mu_p}^i\left(\mu_p\right) \tag{4.12}$$

where the functions F_j^i, referred as the *parameters modes*, are unknown. The parameter modes can be considered as global shape functions that are not a priori

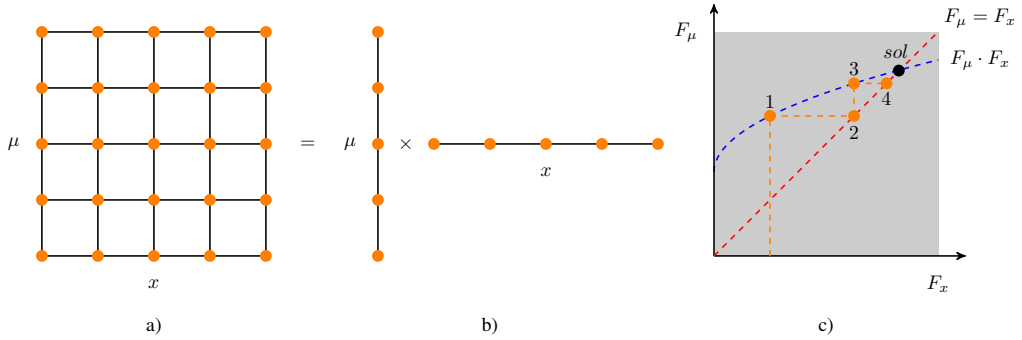

Figure 4.3: The Proper Generalized Decomposition: (a) Original problem, (b) Separated representation and (c) Fixed-point algorithm scheme.

given. Therefore, the goal of PGD is to calculate them. As a direct consequence of considering parameters as extra coordinates, the computational domain increases its dimensionality, so that, the new problem to solve is non-linear. Therefore, an algorithm such us the fixed point iteration is used to compute and construct iteratively the reduced order model.

Traditionally, the PGD formulation is explained through an example by using the Poisson's Equation (see Chinesta et al., 2014 [26] for a detailed description). However, we adopt the notation of Aguado 2015 [2] due to be generic and more didactic to explain the method. In addition, a graphical representation of the main ingredients of PGD is represented in Figure 4.3. For the sake of simplicity, let us consider a scalar version of Equation (4.12), where the field of interest u can be approximated as u^r by the product of two functions $(F_x^r, F_\mu^r) \in V_x \times V_\mu$. Each function F_j^i is previously defined by two functional spaces, V_x and V_μ, that describe the physical and the parametric space, respectively and satisfy the requirements described in Equation (4.2), including the boundary conditions. Therefore, the solution of our problem, written in the separated format, is expressed as:

$$u(x;\mu) \approx u^r = \sum_{i=1}^{r} F_x^i(x) F_\mu^i(\mu) \tag{4.13}$$

To calculate the unknown function pair (F_x^r, F_μ^r), the following finite dimensional

approximation spaces are considered:

$$V_x \coloneqq span\left\{v_x^i = \frac{F_x^i}{||F_x^i||}\right\} \text{ and } V_\mu \coloneqq span\left\{v_\mu^i = \frac{F_\mu^i}{||F_\mu^i||}\right\} \text{ for } 1 \leq i \leq r \quad (4.14)$$

where $||\cdot|| \coloneqq \langle \cdot\ ,\ \cdot \rangle^{\frac{1}{2}}$ refers to the L^2 norm and v_j^i corresponds to the normalized version of F_j^i. The tensor product of both functional spaces defines the space $V \coloneqq V_x \otimes V_\mu$. From V, the following subset S_r, named as the approximation space, is determined:

$$S_r = \left\{ v \in V : v = \sum_{i=1}^{r} u^r v_x^i v_\mu^i, \text{ with } v_x^i \in V_x,\ v_\mu^i \in V_\mu \text{ and } u^r \in \mathbb{R} \right\} \quad (4.15)$$

In PGD, S_r is generated in a progressive manner, following the relation $S_r = S_{r-1} + S_1$ for $r \geq 2$. As a consequence, the successive approximated spaces are nested, i.e. $S_{r-1} \subset S_r$.

Under the assumption that S_r has been previously built, so that u^r is known. Then, the PGD algorithm aims to compute the pair $(F_x, F_\mu) \in V_x \times V_\mu$ that fulfils for every $v \in V$:

$$a\left(F_x F_\mu, v\right) = l\left(v\right) - a\left(u^r, v\right) \quad (4.16)$$

The right-hand-side of Equation (4.16) defines the residual of PGD while computing the pair (F_x, F_μ) involves solving a non-linear problem. For this later task, the fixed point algorithm is applied in the following form:

1. Under the assumption of F_μ is known, F_x is updated.
2. Now that F_x is computed, F_μ is updated.
3. Return to point 1 until:
   - the maximum number of iteration is reached, $i = i_{max}$.
   - the convergence criterion is less than the user specified tolerance ε_1.

$$|| \left(v_x v_\mu\right)_i - \left(v_x v_\mu\right)_{i-1} || < \varepsilon_1 \quad (4.17)$$

Due to the iterative nature of PGD, the solution accuracy is incremented when more parametric modes are included in the solution. In this sense, we can classify PGD as an *adaptive* method and in the case of $r \to \infty$, then $u^r \to u$.

When compared to a FOM, for a problem with d dimensions (parameters) and n nodes in each dimension, the computational cost is proportional to the total number of degrees of freedom n^d. In contrast, by using the separated representation, PGD is able to reduce the computational complexity during the off-line phase to $r \times d \times n$ computations, where r is the number of unknown modes to be determined. Then, during the on-line phase, the solution for any choice of parameters is particularized on-the-fly without solving any additional algebraic system [2, 94]

Regarding the PGD applicability, by considering the parameters as extra coordinates, new possibilities were opened in different fields, such as resolution of high-dimensional stochastic problems [72], simulation of haptic devices [71], real-time control of thermal processes [2], design of metamaterials [100], coupled magneto-mechanical analysis [11], just to name a few. For a more detailed analysis, the interested reader is referred to Chinesta et al, 2013 [27] and the references therein.

As a drawback, it should be point out that PGD is an *intrusive* method. Therefore, it is required to rewrite the problem in terms of the product decomposition of functions F_i^j. This detail acts as a barrier of entry for using the method in a daily basis of an industrial environment as implementing PGD in general, implies an important coding effort [32]. Another important issue is regarding the efficient treatment of non-linear problems, where the non-linear term (either a coefficient or a differential operator) must be written in the separated representation format and then, evaluated at each step. During this iterative procedure, due to the projective nature of PGD, all the computational savings of the method are lost [2].

4.2.3.4 Discrete Empirical Interpolation Method

The Discrete Empirical Interpolation Method (DEIM), is *a posteriori* and *interpolation-based* model order reduction technique, developed by Chaturantabut and Sorensen [25]. This technique aims to overcome the drawbacks related to the approximation of non-linear problems when POD is used. The two main ideas of DEIM are: *i*) an interpolating basis is computed from a collection of snapshots of the non-linear term and *ii*) a set of indices defines the non-linear components to be simulated [93].

In order to explain the DEIM formulation, we designate a non-linear function $f : \mathbb{R}^n \to \mathbb{R}^n$, (e.g. the non-linear term in Equation 4.3). Then, after providing a collection of n_s snapshot samples of $f(\,\cdot\,)$, the snapshot matrix $\mathbf{F}$ is built as $\mathbf{F} = [f_1(\boldsymbol{\mu}), \cdots, f_{n_s}(\boldsymbol{\mu})]$, where $f_i(\boldsymbol{\mu}) = f(u_i(\boldsymbol{x};\boldsymbol{\mu});\boldsymbol{\mu}))$.

Then, the DEIM *basis* $\mathbf{U} \in \mathbb{R}^{n \times m}$ is computed by performing a low-rank approximation of $\mathbf{F}$. This step is done by calculating first a SVD and then retaining only the m left singular values (i.e. the top m singular values).

From $\mathbf{U}$, m different rows are selected in order to define the *selection operator* $\mathbf{P} = [e_{p_1} \cdots e_{p_m}] \in \mathbb{R}^{n \times m}$, where e_{p_i} refers to the p_i-th column of the $n \times n$ identity matrix $\mathbf{I}$ and are defined by a greedy algorithm [25].

Then, the DEIM *projector* is defined as:

$$\mathbb{P} = \mathbf{U} \left(\boldsymbol{P}^T \mathbf{U} \right)^{-1} \boldsymbol{P}^T \tag{4.18}$$

In that way, the DEIM approximation of $f(\,\cdot\,)$ is

$$\hat{f}\,(\,\cdot\,) = \mathbb{P} f\,(\,\cdot\,) \tag{4.19}$$

Once $\mathbf{U}$ and $\mathbf{P}$ has been determined, the reduced model is obtained by replacing $f(\,\cdot\,)$ by $\hat{f}(\,\cdot\,)$, where the DEIM approximation of the non-linear function is evaluated in the form $\boldsymbol{u}(\,\cdot\,) = \boldsymbol{\Phi}_r \boldsymbol{u}_r(\,\cdot\,)$. Then, the result is projected into the reduced base $\boldsymbol{\Phi}_r \in \mathbb{R}^{n \times r}$ (see section 4.2.3.1).

$$\begin{aligned} f_r\left(\boldsymbol{u}\left(\boldsymbol{x};\boldsymbol{\mu}\right);\boldsymbol{\mu}\right) &= \boldsymbol{\Phi}_r^T \hat{f}\left(\boldsymbol{\Phi}_r \boldsymbol{u}_r\left(\boldsymbol{x};\boldsymbol{\mu}\right);\boldsymbol{\mu}\right) \\ &= \boldsymbol{\Phi}_r^T \boldsymbol{U} \left(\boldsymbol{P}^T \boldsymbol{U} \right)^{-1} \boldsymbol{P}^T f\left(\boldsymbol{\Phi}_r \boldsymbol{u}_r\left(\boldsymbol{x};\boldsymbol{\mu}\right);\boldsymbol{\mu}\right) \\ &= \underbrace{\boldsymbol{\Phi}_r^T \boldsymbol{U} \left(\boldsymbol{P}^T \boldsymbol{U} \right)^{-1}}_{\text{precomputed:} r \times m} \underbrace{f\left(\boldsymbol{P}^T \boldsymbol{\Phi}_r \boldsymbol{u}_r\left(\boldsymbol{x};\boldsymbol{\mu}\right);\boldsymbol{\mu}\right)}_{m \times 1} \end{aligned} \tag{4.20}$$

During the off-line stage the matrices $(\boldsymbol{\Phi}_r^T \mathbf{U})$ and the factorization $\mathbf{P}^T \mathbf{U}$ are precomputed. Then, in the on-line stage, instead of evaluating the non-linear function, only $m \leq n$ selected number of terms will be evaluated at the indices that determine the columns of the selection operator $\mathbf{P}$.

DEIM leads to a non-linear ROM that can be evaluated efficiently. The method has been successfully applied to shape optimization [5], reservoir modeling [44] and viscoplasticity [45]. However, when the number of snapshot required to construct the basis $\boldsymbol{U}$ is important ($n_s \to n$) or the terms needed to define $\boldsymbol{P}$ are increased ($m \to n$), the computational gains are lost [93].

4.2.3.5 Sparse Subspace Learning (SSL)

Sparse Subspace Learning (SSL) is a *non-intrusive* model order reduction technique, suitable for multi-parametric studies and non-linear analysis. The method was proposed by Borzaacchiello and Aguado [14] and exploits the sparsity of the solution

with respect to the parameters in order to build a parametric solution from the computation of only few wisely chosen snapshots.

Given a field of interest $\boldsymbol{u}(\boldsymbol{x})$ for a defined set of parameters $\boldsymbol{\mu}$, by using the separated variable representation under the SSL formulation, it can be written as:

$$\boldsymbol{u}\left(\boldsymbol{x};\boldsymbol{\mu}\right) \approx \boldsymbol{u}^{r} = \sum_{i=0}^{k} \alpha_i\left(\boldsymbol{x}\right) \psi_i\left(\boldsymbol{\mu}\right) \tag{4.21}$$

where $\alpha(\boldsymbol{x})$ and $\psi(\boldsymbol{\mu})$ are defined as the *surpluses* and *parametric functions*, respectively. The parametric functions $\psi(\boldsymbol{\mu})$ act as the shape function. They are known, define the hierarchical basis and correspond to the Lagrangian polynomials, while the surpluses functions $\alpha(\boldsymbol{x})$ need to be determined. They are calculated as a linear combination of sampling or measurements evaluated at the *collocation points* $\mathcal{P}_n = \{\mu_0, \mu_1, ..., \mu_n\}$.

For a unidimensional parametric problem, the collocation points are the extreme of the *n-th* Chebyshev polynomials of the first kind, $T_n(\mu)$ and are referred as Gauss-Chebyshev-Lobatto points (GCL) too. To obtain them, it is required to solve the following equation:

$$T_n\left(\mu\right) = cos\left(\frac{\pi i}{n}\right) \quad i = 0, ..., n \tag{4.22}$$

In order to handle a multidimensional parametric problem, first, each parameter is treated as the unidimensional case described before and then, the *Smolyak rule* is introduced with the aim of constructing the sparse grid to be used during sampling. To put into perspective the advantage of the sparse sampling respect to the full sampling based on the tensor product, for a 2 parameters problem and a selected hierarchy level $k = 5$, the full sampling requires $33^2 = 1089$ points, while the sparse sampling only needs 177 points, providing a reduction of 83.7% in terms of computational cost.

Once the sampling points are defined, the simulations are launched in a commercial FE software (e.g Abaqus, Ansys). The field of interest $\boldsymbol{u}\left(\boldsymbol{x};\boldsymbol{\mu}\right)$ is known at each collocation point and for our case, it is considered as the reference solution. With this available information, the corresponding surplus functions are determined as the difference between the exact and the approximated solution at the hierarchy level $(k-1)$, as expressed in the following expression:

$$\alpha_i\left(\boldsymbol{x}\right) = \boldsymbol{u}\left(\boldsymbol{x};\mu_i\right) - \boldsymbol{u}^{k-1}\left(\boldsymbol{x};\mu_i\right) \tag{4.23}$$

4.2.4 MOR applied to manufacturing problems

In this section, a brief collection of MOR problems applied to manufacturing is presented. Before proceeding, let us introduce the specific challenges that must face the simulation of this kind of problems:

- Geometric complexity: complex and evolving geometries are produced.
- Multi-physics problem: several physics involved on the same domain with non-linear material laws and coupled models.
- Pronounced localization of deformation.
- Transfer of data: if multiple simulation packages are used.
- Real-time solving capability: if simulation wants to be implemented at the shop-floor level.

At the moment, standard simulation techniques as Finite Element Methods (FEM), are used by the industry but they can be considered as rigid due to the use of static data. However, to overcome the limitations described before, MOR is presented as a proven useful alternative, based on the following examples presented below.

With the aim to study the plasticity, as the one experienced in any forming processes, Nasri et al. [70] proposed a separated representation of the elastic-plastic problem by applying POD at each incremental step to the force vector in the general problem $\boldsymbol{K}\boldsymbol{u} = \boldsymbol{F}$, where each term corresponds to the stiffness matrix, the displacement and force vector, respectively. This is an example of how the presence of non-linearities obliges to reconstruct the original approximation space to evaluate the non-linear term, as depicted on Figure 4.2b.

On the field of distortion after machining, Poulhaon et al. [77] studied the problem in two steps by using POD. First, an off-line reduced basis of admissible geometrical changes is generated numerically and complemented via experiments. Then, an on-line prediction of distortion during machining is performed. This analysis can help to modify in advance the tool path during machining and to plan future post-machining operations to mitigate distortion. However, this work is focused to parts machined from aluminium rolled plates, where the residual stress field can be

considered as constant along the part, in contrast to the complex three dimensional residual state present in forged parts.

Distortion is not an exclusive phenomenon of forgings. It is a recurrent problem in welding and additive manufacturing too. For both cases, the dimensional inaccuracies are a consequence of the rapid heating and cooling of the deposited material, which experiences a non-uniform local shrinkage, giving place to the development of residual stresses. In the framework of MOR, Sikstrom et al. [101] used a reduced model to control the process of tungsten arc welding while Canales et al. [18] developed a mixed formulation of MOR with GFEM to study friction-stir welding. On the other hand, Quaranta et al. [80] proposed a simplified parametric model based on PGD to compensate distortion in additive manufacturing. In the cited works, all the efforts are focused on predicting distortions before they are produced. However, to the best of our knowledge, no previous attempt has been made to apply MOR techniques to study the post-machining operations required to mitigate distortions once the geometrical mismatches were arising.

During bending straightening, the springback phenomenon is present. Therefore, the concept of *shape manifold*, introduced by Raghavan et al. [82], has some potential. The idea refers to generate all possible post-springback admissible shapes by building a reduced-order shape-space. The MOR is done through a combination of POD and Diffuse Approximation with the aim to find the optimum design point. Although the presented case study was applied to a 2D sheet problem, a furhter development is required to use the concept in 3D geometries as for the case of forgings.

Contact is another main issue to consider, as it is present in any manufacturing process (e.g. stress relief and reshaping). Giacoma [46] presented an iterative SVD algorithm, which provides a quasi-optimal bases to solve a contact problem with LATIN-PGD. The algorithm was applied to a 2D quasi-static contact problem with an isotropic hardening model, and as a consequence, Bauschinger effect is not included.

Despite MOR has reached a maturity level for linear problems and well-established projection-based techniques are available, PCA, RB and PGD can not be used them to study reshaping, as the problem involves strong non-linear phenomena (e.g geometrical non-linearity and plasticity). In case they are applied, all the computational savings are lost as the tangent stiffness matrix of the full-order problem is required

to be reconstructed [32].

On the other hand, to tackle the non-linearities, it is a standard practice to combine POD with DEIM [13]. However, in order to apply DEIM, it is required to have snapshots of the non-linear function. When plasticity is present, the snapshots must be taken from the internal forces, which involves to have a base in terms of stresses with the form $\boldsymbol{\sigma}(\boldsymbol{\chi}_i) = \sum_k \boldsymbol{\psi}_k(\boldsymbol{\chi}_i)\boldsymbol{\alpha}_k$, where $\boldsymbol{\chi}_i$ are the interpolation points, $\boldsymbol{\psi}_k$ is the DEIM base and $\boldsymbol{\alpha}_k$ are the coefficients to find. In addition, another potential drawbacks for DEIM are: *i*) The tangent (Jacobian) matrix does not have to be symmetric, and from the algorithmic point of view, this detail represents a problem; *ii*) It is an intrusive method ; *iii*) The problem we want to solve does not have only plasticity, it has also large deformations and contact. At the moment, there is no available intrusive method that allows to deal with all these complexities simultaneously in a robust way.

Regarding the SSL, its non-intrusiveness is a key factor for any industrial application as it allows to use the current FE commercial software available in the company without any extra investment in terms of money or code development. In addition, the method has been successfully applied to sheet metal forming, allowing to study the friction relation between the tool and the part in a virtual environment [15].

In this work, we want to explore the use of novel MOR techniques to study the non-linear problem of reshaping. Therefore, the SSL is the selected method to study bending straightening thanks its non-intrusiveness and the capability to handle the non-linearities present during the process.

4.3 Multi-parametric bending straightening

The interest to develop a ROM of bending straightening is twofold. First, the model can provide a detailed information of the process to the manufacturing team in a cost-effective way and second, to reduce the gap between the theory and practical approach used at the shop-floor level. It is expected that, by using the ROM, both teams can be able to explore in an early stage the repairing process and select optimal process configuration.

Once the MOR method was chosen, the next step is to define the different parameters involved to model bending straightening and select the most representative.

Then, the model is described by using the SSL formulation. Finally, the problem setup is defined before launching the battery of simulations required to solve the multi-parametric analysis.

4.3.1 Process model and parameters

The mechanics behind bending straightening for simple geometries can be described by plastic bending theory. Early attempts to outline the behaviour of a beam above its yield point for a rectangular cross section were done by Timoshenko [109], where the typical residual stress after unloading, known as the three-cross-zero profile, is explained. However, plastic bending involves more complex phenomena and effects, as initial imperfections, previous residual stresses and strain-hardening. Following this line, Iványi [51] studied the effect of strain hardening in the plastic behaviour of beams by using moment-deflection curves and shown an accuracy increment respect to a perfect plastic material model. On the other hand, an analytical solution to the plastic bending problem was proposed by Štock and Halilovič [107] for the simplified case of a rectangular cross section with no strain hardening. The previous results show that plastic bending for complex geometries, as is the case for bending straightening, must be treated numerically.

Following the strategy proposed by Hardt et al [50], the modelling of bending straightening is divided in two stages. First, plastic bending is represented by a *process model*, where the goal is to simulate as close as possible the process with its respective inputs, parameters and outputs, as represented in Figure 4.4a. Here is where the ROM is constructed. However, the model is only able to provide the final displacements after unloading, therefore, the second stage, called *process simulation* is needed to go from displacements to distortion. This stage includes a measurement program to define distortion and a control algorithm to cope the design specifications, as shown in Figure 4.4b. In our case, the second step is performed as a postprocess of the ROM.

Focusing on the process model, bending straightening is strongly related to the constitutive material material model and must include the considered geometry to repair along with the effects of the machine. Therefore, three main groups of parameters can be defined: *i*) the material properties, *ii*) the part geometry and *iii*) the machine conditions. A summary of all possible parameters, inputs and outputs for the process model is provided in Table 4.1. Here it can be seen that, although

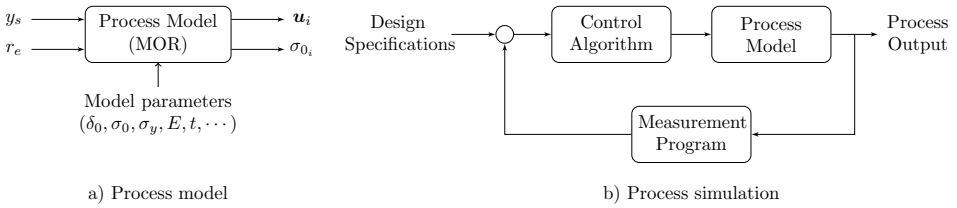

Figure 4.4: Bending straightening. a) Process model and b) process simulation. Adapted from [50].

Table 4.1: Bending straightening process model: inputs, parameters and outputs. Adapted from [50, 112]

Parameters	Inputs	Outputs
Material properties	For each bending step	Displacements (after unloading) $\boldsymbol{u}_i$
- Young's Modulus E	- Internal roller r_i	Current residual stresses σ_{0i}
- Poisson's ratio $\boldsymbol{\nu}$	- External roller r_e	
- Yield stress $\boldsymbol{\sigma_y}$	- Stroke y_s	
- Initial residual stress σ_0		
- Strain hardening		
Part geometry		
- Cross-section		
- Initial distortion δ_0		
Machine conditions		
- Punch geometry radius		
- Friction coefficient μ		
- Machine stiffness		

the mechanics behind plastic bending is simple, the quantity of involved parameters explains the complexity of the process and the challenge, from the numerical point of view, to run a multi-parametric simulation.

In this study, we are mainly concerned with the effect of the initial distortion δ_0 in reshaping, therefore, from all the possible process model parameters, only δ_0 is selected. In addition, the stroke y_s and the external roller r_e, that corresponds to the inputs of the process model, complete the set of variables to perform the multi-parametric analysis. Note that, while in chapter 3 we explored the four points bending configuration to solve the reshaping problem, from now on, we switch to

the three points bending arrangement, which can bee seen as a particularization of the former setup. This decision has been taken to limit the process input from three (stroke y_s, internal and external rollers positions, r_i and r_e, respectively) to the pair (y_s, r_e) only as r_i is already fixed at the beam's mid span. As a consequence, the T beam cross section after machining and the machine conditions are fixed too. In addition, it is assumed that the material properties of the forge are constant. Regarding the latter assumption, two possible further candidates to explore its effects in the post-machining distortion are the yield stress σ_y and the Young's Modulus E, following the findings reported about the variability of the mechanical properties of aluminum [37, 86].

4.3.2 Reshaping under the SSL formulation

For bending straightening, we are interested in determining the final shape of a part after performing a cycle of loading and unloading. Therefore, the displacement field $\boldsymbol{u}(\boldsymbol{x})$ for a given set of parameters $\boldsymbol{\mu}$ is our field of interest $\boldsymbol{u}(\boldsymbol{x}; \boldsymbol{\mu})$.

For the three-point bending straightening operation, the set of parameters $\boldsymbol{\mu}$ is composed by the initial distortion δ_0, the position of the external roller r_e and the imposed vertical displacement y_s. For our problem, each parameter is considered as a dimension.

$$\boldsymbol{\mu} = (\delta_0, r_e, y_s) \tag{4.24}$$

When the solution $\boldsymbol{u}(\boldsymbol{x}; \boldsymbol{\mu})$ is reconstructed for all the parametric domain, the remaining distortion δ can be found as a post-processing operation and it is defined as:

$$\delta(\boldsymbol{\mu}) = \max_{\boldsymbol{x}} \left[\boldsymbol{u}(\boldsymbol{x}; \boldsymbol{\mu})\right] - \min_{\boldsymbol{x}} \left[\boldsymbol{u}(\boldsymbol{x}; \boldsymbol{\mu})\right] \tag{4.25}$$

However, for all the possible reshaping configurations, we are mainly interested to know the optimum stroke y_s^{opt} that, for a fixed set of parameters (δ_0, r_e) will minimize the remaining distortion δ in the structural part.

$$y_s^{opt} = \arg\min_{y_s} \left[\delta(\delta_0, r_e, y_s)\right] \tag{4.26}$$

4.3.3 Problem setup

To study the three-point bending operation, the T shaped beam previously defined in chapter 3 is used, as shown in Figure 4.5. Regarding the material definition

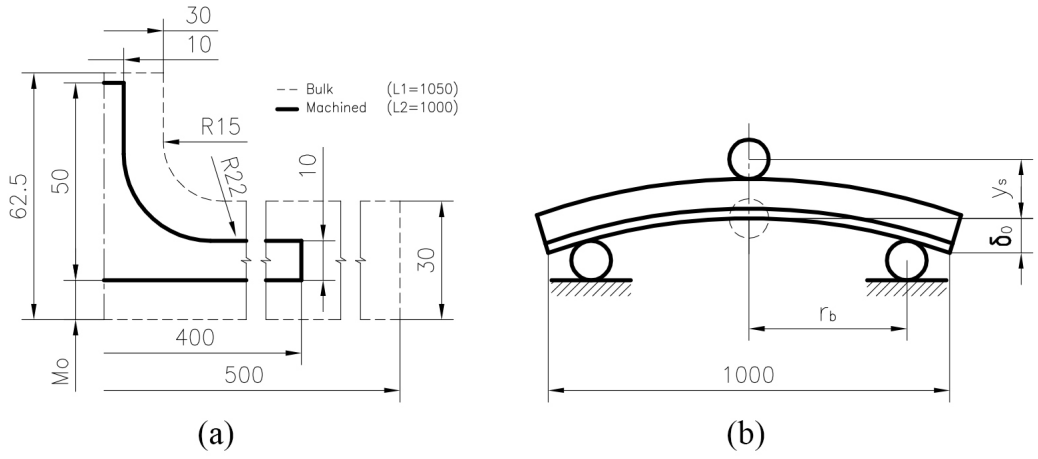

Figure 4.5: T shaped beam. a) Geometry definition and b) Parameters representation for three-point bending straightening.

Table 4.2: Parameters values for the three-point bending operation

Parameter ID	Description	μ_{min}	μ_{max}	
1	Initial distortion δ_0	-15	0	mm
2	External roller position r_e	100	485	mm
3	Imposed vertical displacement y_s	5	30	mm

and model, the configuration is the same used as in chapter 2. For the following study, the parameters to be explored are available in Table 4.2 with is minimum and maximum values μ_{min} and μ_{max}, respectively.

Based on the results obtained in chapter 3, it was observed that the main distortion experienced by the forged part was in its longitudinal direction (referred as distortion type 1). Respect to the wings closure (distortion type 2), no repair effects were experienced after applying bending straightening. Therefore, the selected strategy to include δ_0 as an extra parameter was to consider the beam subjected to pure bending, working under a fictitious moment M in both extremes so that, the amplitude of the vertical displacements in the section $x = \frac{1}{2}L$ is given by the elastic response of the structure $\delta_0 = -\frac{ML^2}{8EI}$, where L, E and I correspond to the beam's span length, the Young's Modulus and the inertia of the cross section, respectively. This strategy is graphically represented in Figure 4.6 and its implementation

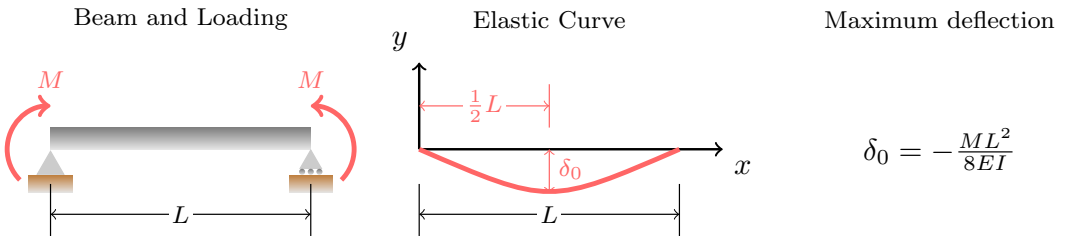

Figure 4.6: Parametrization of initial distortion δ_0 as a function of fictitious moment M.

is described in a pseudo-code style in Algorithm 1.

Of course other strategies of shape parametrization are possible. For example, if experimental measurements are available, the initial warped geometry can be parametrized by statistical means. Lauzeral et. al, [58] combined statistical shape analysis (SSA) with PCA to automatically generate shape-parametric models of tissues and organs from medical images. This work opens the door to update the theoretical CAD geometry with real data that is available at the shop floor. Additionally, this strategy could be a way to explore and tackle the nature variability of post-machining distortion.

Finally, a Python script was developed in order to run the 123 Abaqus simulations. This is the quantity of snapshoots required to explore the parametric input space under the SSL method for a hierarchy level $k = 3$. A summary of the work-flow is given by Algorithm 2.

4.4 Results and discussion

Before proceeding to present the results, a graphical comparison between the full sampling strategy and the performed sparse sampling is shown in Figure 4.7. Here, it can be seen how prohibitive that can be the task to explore a parametric space if the full sampling is selected. Hereafter, the first 8 snapshots of the parametric bending straightening are represented in Figure 4.8. They corresponds to the extreme values of each parameter, located at each corner of the parametric space (see Figure 4.7b). They are the solution for a hierarchy level $k = 0$ and are used to reconstruct the displacement field $\boldsymbol{u}(\boldsymbol{x}; \boldsymbol{\mu})$.

The reshaping diagram, from a multi-parametric point of view, is the result of a

Algorithm 1 Initial distortion generation

procedure INITIALDISTORTION.PY
    problem setup ← geometry, material properties and BC
    load ← initial distortion δ_0
    input file ← job generation
    output database ← job execution *from input file*:
    $\boldsymbol{x}_0$ ← undistorted geometry
from output database:
    $\boldsymbol{u}_0$ ← displacement
write distorted input file (RSF):
    $\boldsymbol{x} \leftarrow \boldsymbol{x}_0 + \boldsymbol{u}$.
end procedure

Algorithm 2 Reshaping simulation SSL

procedure RESHAPING3D.PY
pre-processing:
    $\boldsymbol{\mu}$ ← parameters interval
    k ← hierarchy level
    p_n ← collocation points
    $\boldsymbol{\mu}_{sim}$ ← Smolyak Rule
snapshoots:
    for $i \leq len(\boldsymbol{\mu}_{sim})$ **do**
        Initial distortion generation
        Reshaping simulation
    end for
post-processing:
    $\boldsymbol{u}(\boldsymbol{x}; \boldsymbol{\mu})$ ← displacement field reconstruction
    $\delta(\boldsymbol{\mu})$ ← reshaping diagram generation.
    y_s^{opt} ← optimum parameters.
end procedure

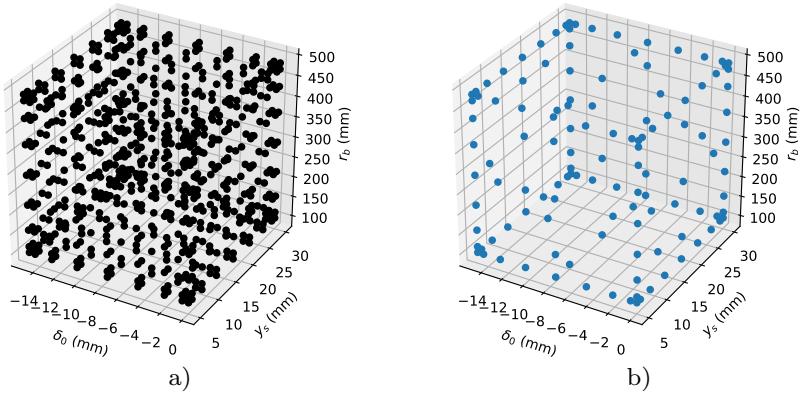

Figure 4.7: Exploration of the parametric space for a hierarchy level $k = 3$. a) Full sampling ($9^3 = 729$ points) vs b) Sparse sampling (123 points).

particularized solution where the pair (δ_0, r_e) is previously defined and y_s is set free. In order to generalize the problem, the next step is to set free a pair of parameters (e.g δ_0 and y_s), giving, as a result, a response surface. With the aim to explore the obtained multi-parametric solution, instead of using a 3D representation, a 2D plot together with level curves are used to describe if the remaining distortion δ will decrease or increase for a fixed external roller position r_e, as can be appreciated in Figure 4.9.

Effect of the initial distortion δ_0***:*** In the previous chapter, it has been proved that reshaping can be studied by using as a main input δ_0 under a Residual Stress Free hypothesis (RSF). This approach was used in order to generate numerically the warped geometry. By including δ_0 as a parameter, the problem of not knowing its magnitude beforehand is overcome. In that way, the reshaping problem is solved numerically for all the interval of initial distortions and once the part is machined, the operator only needs to access to the solution dictionary and select a distorted geometry closer to the experimental result.

Effect of the external roller position r_e***:*** Once the initial distortion δ_0 is known, the next step is to select the reshaping operation. For the three-point bending

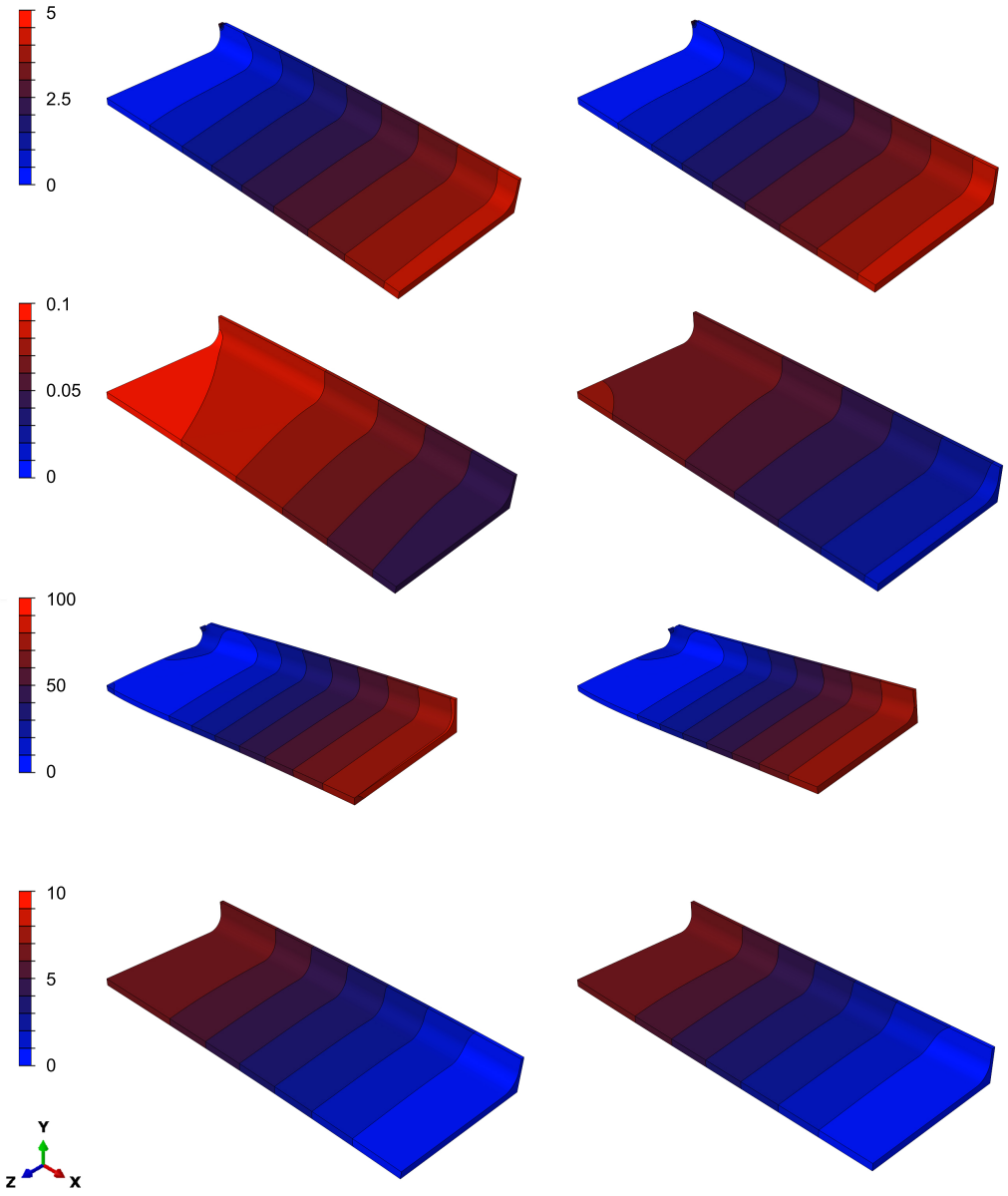

Figure 4.8: First 8 shapshots of the displacement field $\boldsymbol{u}(\boldsymbol{x};\boldsymbol{\mu})$. From left to right $\delta_0 = [-15, 0]$. From top to bottom the pair (y_s, r_e) are (5, 100), (5, 485), (30, 100) and (30, 485), respectively.

operation, the internal roller (top) is fixed and located at the middle of the beam

while the external rollers (bottom) need to be placed. The position of the external roller is defined by the parameter r_e and it defines the slope of the response surface that relates the remaining distortion δ with δ_0 and y_s.

A value of r_e closer to the top roller produces a difficult reshaping operation to control, as it is expected to have a quick change of the remaining distortion δ during bending. On the other hand, a value of r_e away from the top roller generates the opposite behavior with a progressive variation of δ. In the performed parametric study, the selected value of r_e particularizes a page of the solution dictionary.

Effect of the imposed vertical displacement y_s***:*** For a fixed initial distortion and a selected bottom roller position, the three-point bending operation is completed when a vertical displacement y_s is imposed at the internal roller. The magnitude of y_s needs to be defined in order to minimize the remaining distortion δ. The response surface obtained for a fixed r_e shows that reshaping is more difficult to be performed for smaller values of δ_0 as the required stroke y_s only to induce plasticity in the cross section is bigger than δ_0. On the other hand, for a bigger magnitude of δ_0, it is expected to have more margin to find the stroke that minimizes δ.

Visualization of results: The multi-parametric analysis produces data in a dimensional space of size $n = 3$. In order to visualize the results, an user graphical interface (GUI) was developed so that, the evaluation of the parameters associated to the reshaping operation can be done in almost real-time. A GUI's screenshot is shown in Figure 4.10. The environment is divided in 5 parts where the user can explore the influence of each parameter in a virtual environment.

4.5 Conclusions

The industry is willing to have new tools to solve problems that nowadays are treated in an empirical way. Reshaping of large thick structural parts is an example of how MOR can be applied to an open problem, especially the SSL, allows to perform a multi-parametric study to test different *what-if* scenarios in a cost-effective way and, thanks to its non-intrusiveness, acts as a bridge to join MOR with the available third-party FEM solutions.

For the case of bending straightening, the initial distortion δ_0 is the starting point

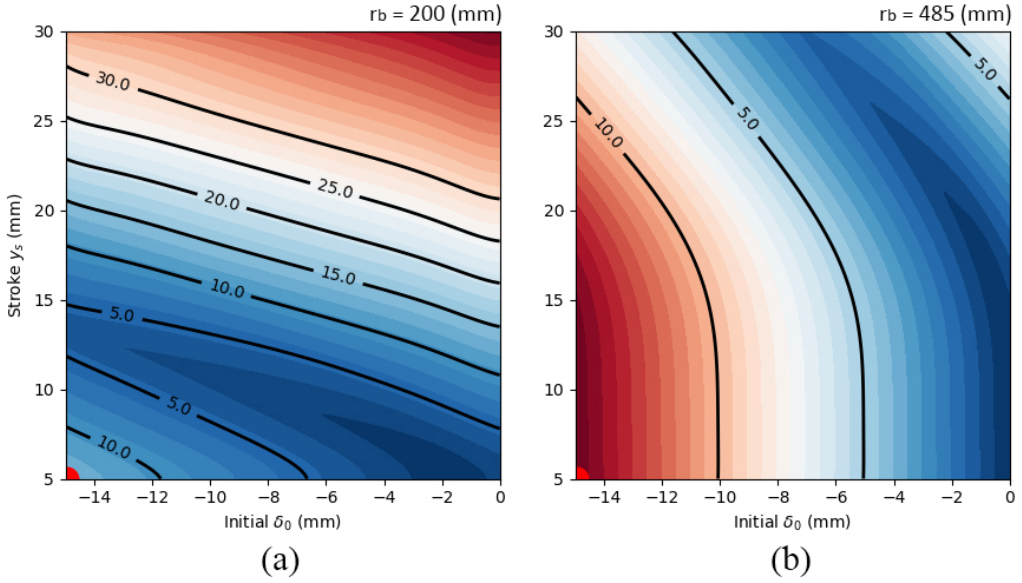

Figure 4.9: Response surface: Remaining distortion δ. Solution selection as a function of r_e. a) $r_e = 200$(mm) and b) $r_e = 485$(mm).

for reshaping and it determines the setup for the technological parameters r_e and y_s. Additionally, the problem of not knowing beforehand the value of δ_0 is overcome by including it as a parameter. Then, thanks to the SSL, this reshaping operation can be studied in a virtual environment before launching the real process.

In the next chapter, we will analyse how to chain multiple reshaping operations. However, future work is needed to include material properties as extra parameters. As expected, the computational cost for the numerical analysis will increase. Again, here it resides the importance of studying reshaping with MOR techniques.

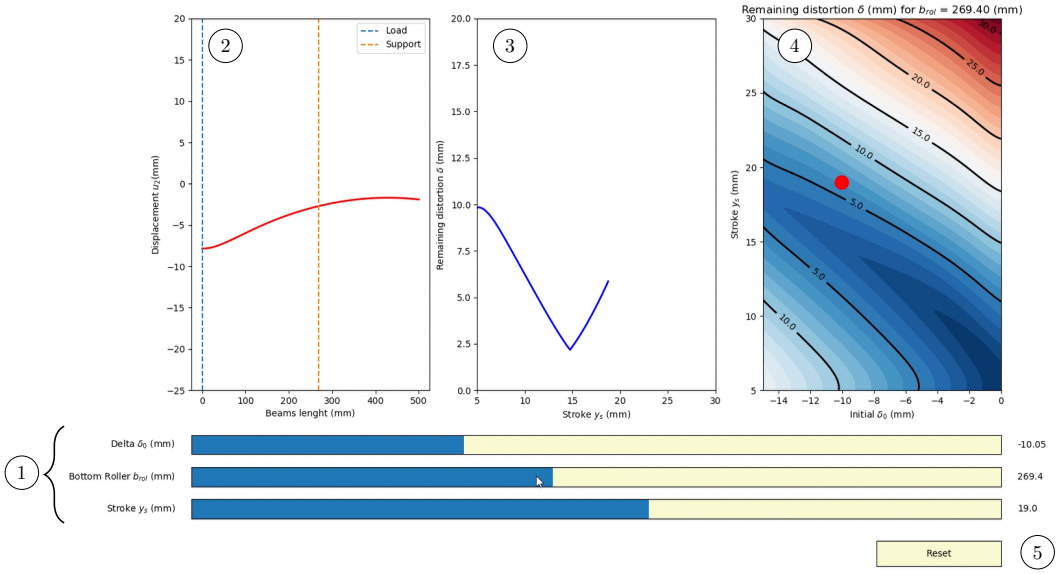

Figure 4.10: GUI for results' visualization: 1) Parameters selection, 2) Beam's geometry after unloading, 3) Reshaping diagram generation, 4) Page selection of the solution dictionary, 5) Reset button

Chapter 5

Evaluation of multiple reshaping operations via MOR

Reshaping is an iterative process where at each step, it is intended to reduce distortion until the resulting geometry fits inside the design tolerance. However, as the process evolves, the warped geometry changes, and with it, the process parameters need to be adjusted accordingly. From the simulation point of view, this continued evolution in the process represents a challenge as the boundary conditions are different and the associated technical parameters (e.g. roller positions and stroke) need to be recalculated. In this chapter, two consecutive bending straightening steps are simulated within a Model Order Reduction framework. The goal is to evaluate different strategies for successive reshaping operations and to find the best available sequence of operations to repair the part. Finally, a methodology is proposed to simulate consecutive reshaping steps.

Contents

5.1 Introduction 85

5.2 Multiple bending straightening operations 85

5.2.1 Problem setup 85

5.3 Reference solution: RS for multiple operations 87

5.3.1 First step 87

5.3.2 Second step 88

5.4 Proposed approach: RSF hypothesis for multiple operations 89
5.4.1 First step 90
5.4.2 Second step 90
5.5 Reshaping as a root-finding problem 95
5.5.1 First step: Error estimation 96
5.5.2 Second step: Error estimation 96
5.6 Process signature 98
5.7 Conclusions 100

5.1 Introduction

Reshaping is an iterative process where at each step, it is intended to reduce distortion until the resulting geometry fits inside the design tolerance. However, as the process evolves, the warped geometry changes, and with it, the process parameters need to be adjusted accordingly. From the simulation point of view, this continued evolution in the process represents a challenge as the boundary conditions are different and the associated technical parameters (e.g. roller positions and stroke) need to be recalculated.

The approach followed in chapters 3 and 4 was to consider the reshaping operation of bending straightening for one single step only. This idealization allowed us to study the influence of residual stresses and their technological parameters independently. Now that the process is well known, in this chapter, two consecutive bending straightening steps are simulated within a Model Order Reduction framework. The goal is to determine the best available sequence of operations to repair the part.

The chapter is organized as follows: in section 5.2, the problem setup for running two consecutive reshaping operations is presented. To perform this task, the distortion definition is rewritten in terms of local distortion, which provides more flexibility to define when to stop the process. Then, in section 5.3, the problem is first solved for bending straightening with RS. The obtained results are used as a reference solution to validate the RSF hypothesis applied to consecutive operations. To this end, in section 5.4, the comparison is done again by using the reshaping diagrams. Then, in section 5.5, the reshaping problem is presented as a root-finding problem. This new criteria is used to provide an error estimation of the MOR solution. Next, in section 5.6, the idea of *process signature* is introduced as a qualitative criterion to evaluate multiple reshaping operations, before launching the simulation of the selected configuration. As exemplification, two complete reshaping cycles are performed. Finally, the obtained conclusions are drawn.

5.2 Multiple bending straightening operations

5.2.1 Problem setup

The initial distortion δ_0 is generated numerically, following the procedure described in chapter 3. In order to obtain the warped geometry, a machining offset $M_o = 5$

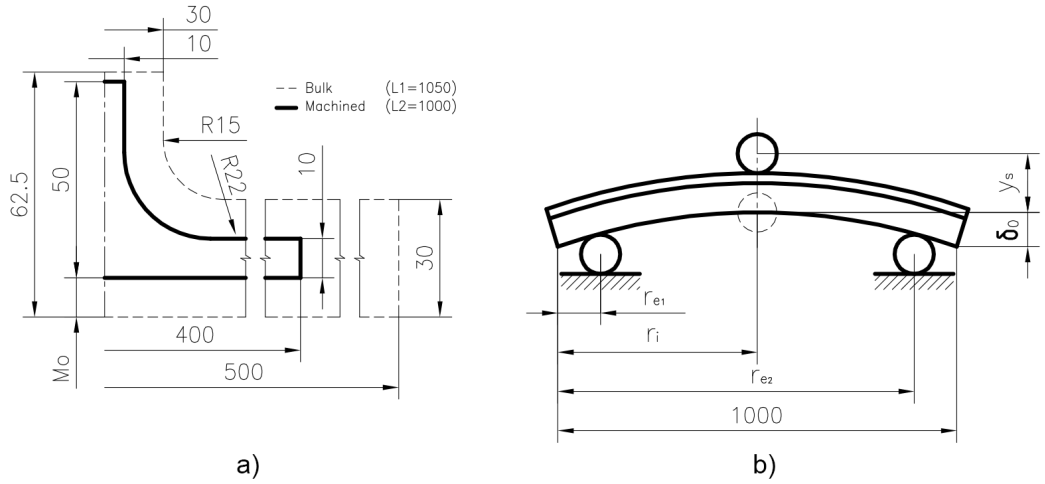

Figure 5.1: T shaped beam. a) Cross section geometry and b) Reshaping set-up

mm is used, which generates a convex shape with an initial distortion δ_0 = -6.165 mm. This configuration was chosen as it provides an initial distortion three times bigger that the structural criteria of $\frac{L}{500}$, where L corresponds to the beam's length [42]. As in previous chapters, a T-shaped beam is used as a simplified version of the cruciform beam. Its geometry is represented in Figure 5.1.

For the present study, the parameter to explore is the stroke y_s and its interval is provided in Table 5.1. As the distortion will evolve along the process, it is required to scale the interval of y_s. In order to perform this task, a coefficient ζ is included and it depends on the portion of the beam that is under repair as:

$$\zeta = \begin{cases} 1.0 & \text{if the entire beam is repaired} \\ 0.25 & \text{if one half of the beam is repaired} \end{cases}$$

Regarding the location of the external and internal rollers, r_e and r_i, respectively, they are not included as parameters, as they are calculated as functions of the remaining distortion δ_i. The values used for each reshaping steps are given in Table 5.2.

In order to analyse the evolution of distortion for multiple bending operations, it is required to update the definition of the remaining distortion, so that it is feasible to track its evolution in a local manner. This requirement has arisen due to the fact that the following reshaping operations can be applied to different portions of

Table 5.1: Reshaping simulation set-up

Description	Parameter	Comments
Machining offset M_o	5 (mm)	Used to generate distortion
Imposed vertical stroke y_s	(0-40)*ζ (mm)	Parameter to explore
Friction coefficient μ	0.05 (-)	Rollers are rigid surfaces
Rollers position	variable	See values in Table 5.2

Table 5.2: Rollers positions during multiple reshaping steps

Step	r_i	r_{e1}	r_{e2}	Units
1	0	-485	485	mm
2-Symmetric	0	-268.35	268.35	mm
2-Non-symmetric	-268.35	-485	0	mm

the beam. To solve this problem, the remaining distortion δ is defined locally by considering just the length of the part that remains inside the external rollers r_{e1} and r_{e2}. This definition is expressed as:

$$\delta_{local}\left(\boldsymbol{\mu}\right) = \max_{\mathbf{x}}\left[\mathbf{u}\left(\mathbf{x};\boldsymbol{\mu}\right)\right] - \min_{\mathbf{x}}\left[\mathbf{u}\left(\mathbf{x};\boldsymbol{\mu}\right)\right] \text{ for } \mathbf{x} \in [r_{e1}, r_{e2}] \tag{5.1}$$

5.3 Reference solution: RS for multiple operations

In order to chain multiple bending straightening operations, we start by repeating the first reshaping simulation as the longitudinal symmetry condition might not be applied to the second reshaping step. Following the strategy developed in chapter 3, the obtained solution with residual stresses is used as the reference solution of our problem. Then, the result of the first reshaping operation is used as an input to run a second step where two possible strategies are evaluated.

5.3.1 First step

After performing the so called *sequential approach*, we start the reshaping analysis with a warped concave geometry. Then, by using the SSL developed in chapter 4

but addapted for one single parameter, the optimum stroke y_s^{opt} is found, giving a repaired geometry with a W shape as depicted in Figure 5.2a (left).

A comparison between the local and global definitions for the remaining distortion is depicted in Figure 5.2a (right). Here, it can be seen that before the optimum configuration, $\delta_{global} > \delta_{local}$. This is due to the fact that δ_{global} contains the total length of the beam, while δ_{local} depends on the location of the external rollers. As a consequence, for each definition, there is an optimum configuration and $y_s^{opt}|_{\delta_{global}} > y_s^{opt}|_{\delta_{local}}$. However, once the optimum configuration is reached for the global case, there is no difference between both definitions.

5.3.2 Second step

Once the first bending straightening step is performed, the initial convex geometry has evolved into a wavy W shape. Here two possible scenarios are available to perform the next reshaping step:

- to use the position of the maximum and minimum remaining distortion along the part to locate the internal and external rollers, respectively.
- to follow the waves pattern and subdivide the problem in two sections: left wave and right wave.

By choosing the first option, the longitudinal symmetry is conserved. However, the pattern of the convex wave (available during the first step) now has changed to a concave one, which means that the reshaping operation is performed in the opposite direction respect to the previous step. Although the location of the max/min along the distorted geometry provides a visual guide to locate the rollers and perform the step, it is counter-productive to bend the part in the opposite direction respect to the first step, as the repair work performed previously is being removed. This behaviour is represented in Figure 5.3a (left).

The reshaping diagram represented in Figure 5.3a (right) evidences the importance of using the local criterion to track the evolution of distortion during the repairing operation. While δ_{local} is able to track the evolution of distortion, δ_{global} indicates that there is not a valid operation to repair the part, which is not true.

For the second option, the following reshaping step is performed at the left half of the beam. The first detail to notice is that the selected waves portion remains convex (so as the initial distortion), therefore, we can mimic the strategy followed

during the first step with the external rollers located at the ribs while the internal roller continues at the wings. This feature can be used as a criteria to select this configuration respect to the symmetric set-up. As a drawback, it should be noticed that longitudinal symmetry is not available anymore. Here lies the importance of including the whole length of the part from the beginning of the simulation process. As a consequence, there is an unavoidable incremental increase in the computational cost.

After performing the SSL simulation for this non-symmetric configuration, it was noticed that while distortion is reduced inside the left zone, the right half is subjected to important rotations as solid rigid, as depicted in Figure 5.4a (left). This is due to the fact that we are acting locally during reshaping but the new configuration after unloading affects the part globally. This behaviour was already reported by the boilermakers and it constitutes a great challenge for them because they can measure locally the zone that is subjected to reparation, but they need to keep track of the modifications at a global level after each intervention [66]. In other words, there is a portion of the part subjected to reshaping while the other half although no plastic strains are generated, it results affected. We can describe this behaviour as *repair locally, affect globally.*

5.4 Proposed approach: RSF hypothesis for multiple operations

In chapter 3, the RSF hypothesis was introduced and its validity was tested for one single step only. This simplification allowed us to set distortion as an extra parameter for our problem in order to launch the MOR analysis developed in chapter 4. Now, with the aim to generalize its applicability, we test its effects when this simplification hypothesis is applied consecutively. Under this scenario, every time a reshaping operation is done, the material is considered without RS. Again, the effects of bending straightening with RS are used as the reference solution, therefore, the analysis performed in section 5.3 is repeated, giving as a result Figures 5.2b, 5.3b and 5.4b, respectively. The results are placed below their counterpart to simplify their comparison and we will focus on the obtained reshaping diagrams to study the response between them.

5.4.1 First step

For the first bending straightening operation, the resulting reshaping diagram is depicted in Figure 5.5a. It can be seen that the RSF curve is on the left from the RS curve and the offset value between both curves is 2.46 mm, which falls in line with the results of chapter 3 (e.g. for configuration P5 the offset is 2.16 mm, as reported on Table 3.2) [1]. The initial offset is used as reference for the next steps.

5.4.2 Second step

For the symmetric set-up, the reshaping diagram shows an inversion in the offset respect to the first step so that now the RSF curve is located to the right respect to the RS case, as shown in Figure 5.5b. The resulting offset has a value of -4.39 mm, so the current offset has doubled respect to the first step (in module). This behaviour is caused by the change of orientation between the first and the second reshaping step, as described before.

Another feature to remark for the symmetric configuration is the absence of elastic behaviour (zone A) in the reshaping diagram for the RS case. It means that plastic deformations take place immediately after loading the part. This is caused as the current compression experienced during the second bending step is added to the previous compression state developed in the first step. Therefore it is easier to reach the yield surface when bending is applied two consecutive times in the central zone of the beam. While the RSF diagram can not capture this specific behaviour by definition, it is still able to represent the global shifted evolution of distortion.

Regarding the non-symmetric configuration, as the reshaping operation is applied in a sector where plasticity was not generated before (left portion of the beam), the offset keeps the same location respect to the first step as can be seen in the resulting reshaping diagram depicted in Figure 5.5c. However, it can be noticed that both diagrams come close to each other, giving as a result a reduced offset value of 0.61 mm. Taking into account that bending straightening is done manually, the task of determining an offset of this magnitude is not practical, so that, the RSF diagram can be used directly for the second reshaping step. This advantage provides another criteria to select this set-up when compared to the symmetric option.

[1] As a remark, it should be highlighted that each bending straightening operation has its own optimal configuration and therefore, its own associated offset. This is reason behind the difference of 0.3 mm between both tests.

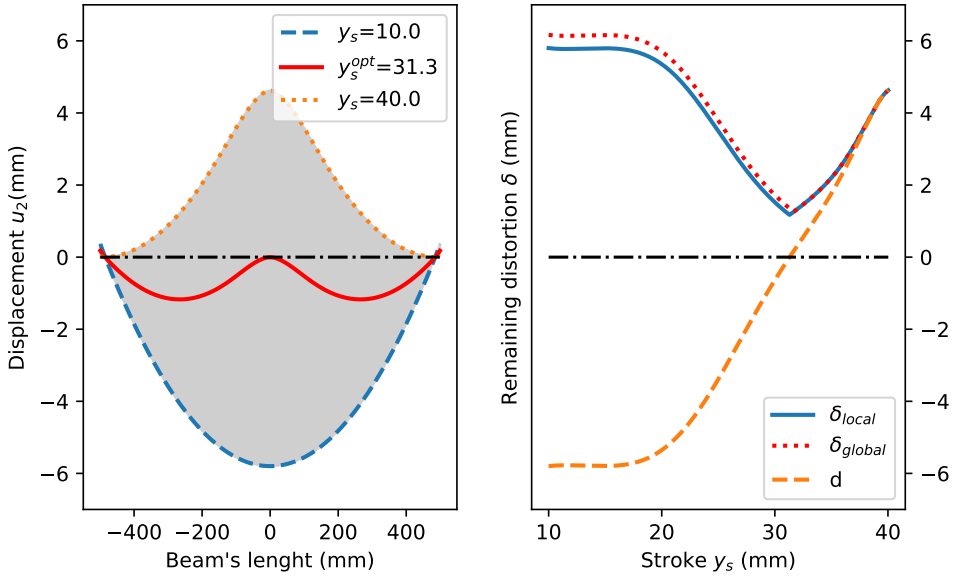

(a) RS case (reference solution)

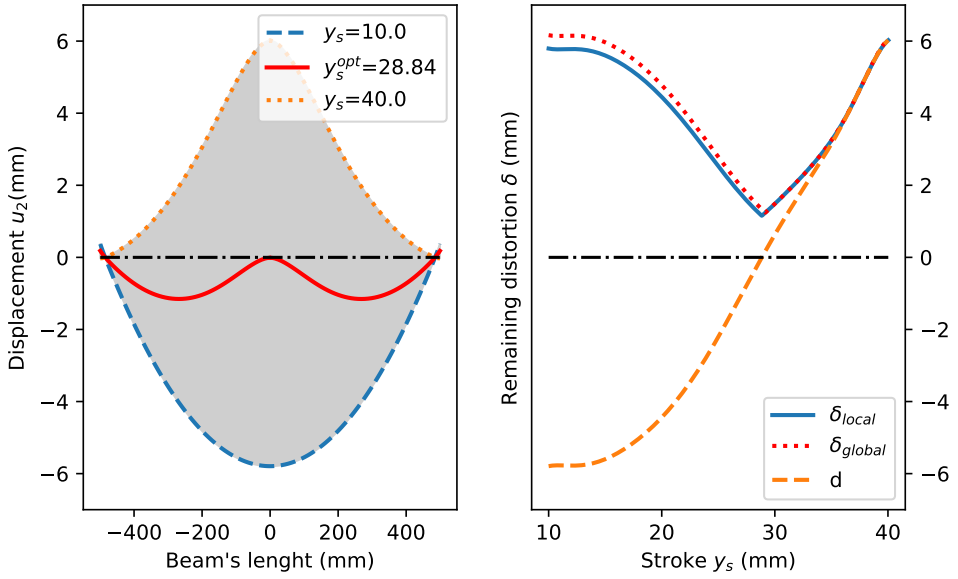

(b) RSF case

Figure 5.2: Multiple bending straightening operations: first step. Left) Reconstruction of the displacement field u_2. Right) Reshaping diagram for different criteria.

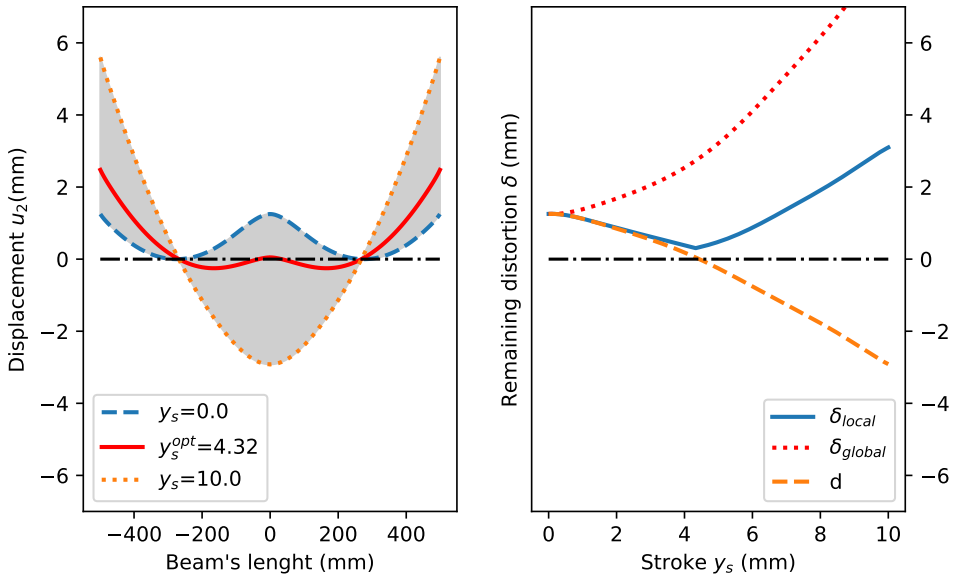

(a) RS case (reference solution)

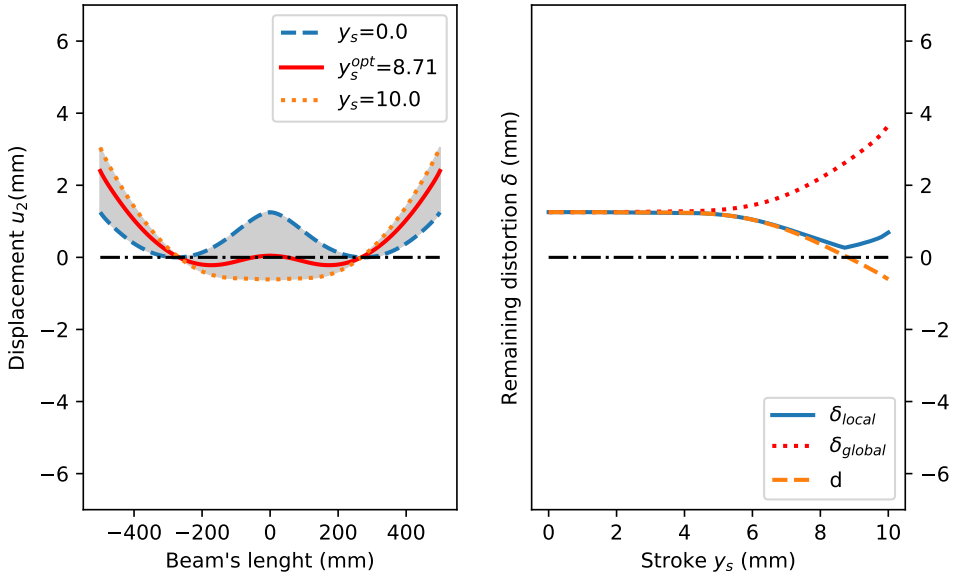

(b) RSF case

Figure 5.3: Multiple bending straightening operations: second step (symmetric configuration). Left) Reconstruction of the displacement field u_2. Right) Reshaping diagram for different criteria.

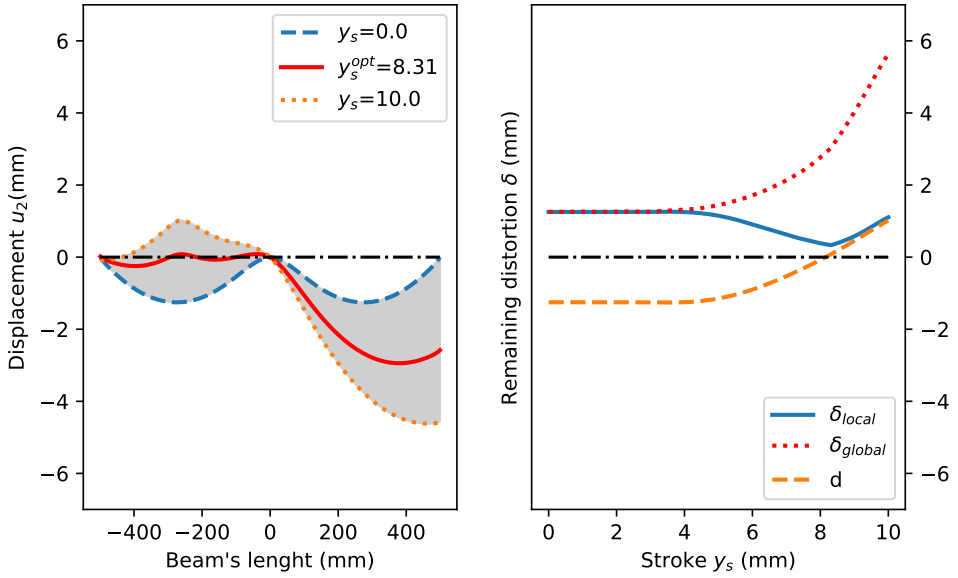

(a) RS case (reference solution)

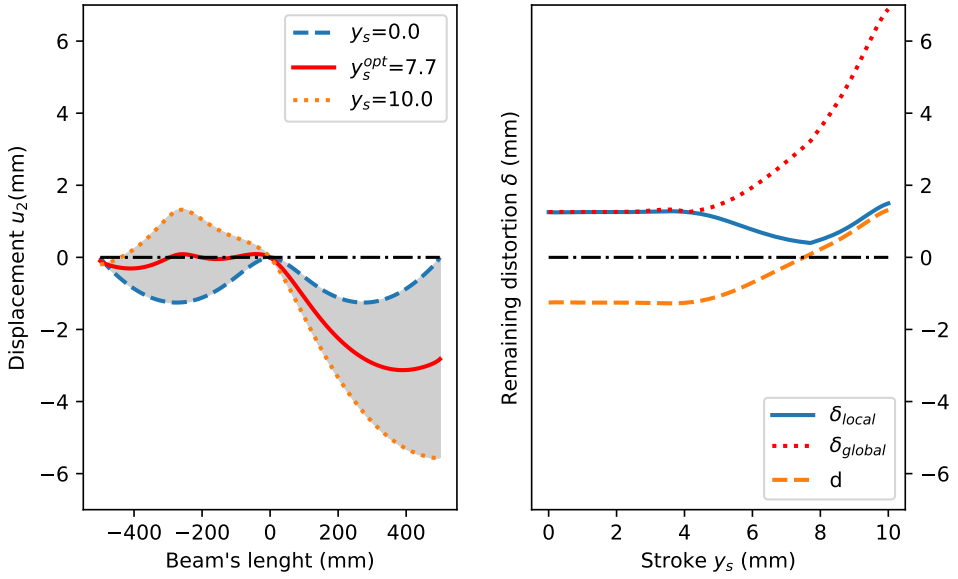

(b) RSF case

Figure 5.4: Multiple bending straightening operations: second step (non-symmetric configuration). Left) Reconstruction of the displacement field u_2. Right) Reshaping diagram for different criteria.

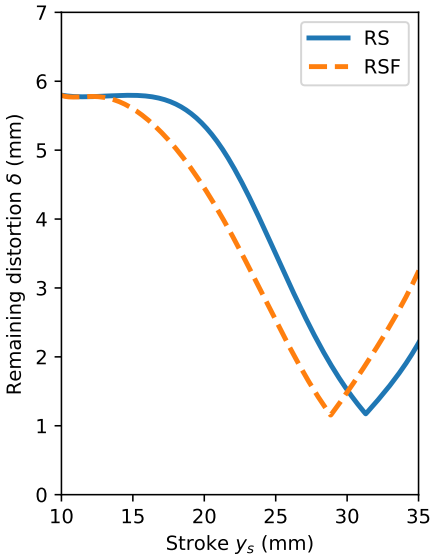

(a) Step 1: symmetric configuration

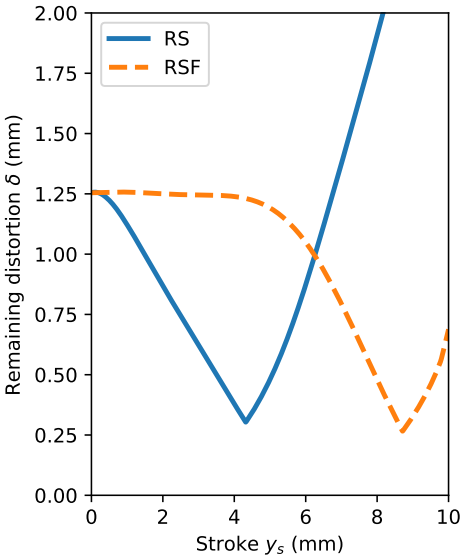

(b) Step 2: symmetric configuration

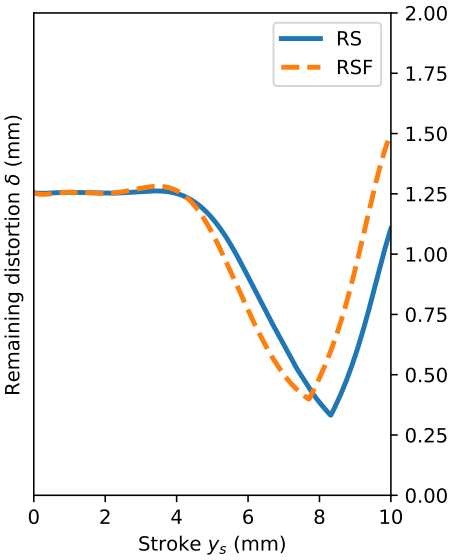

(c) Step 2: non-symmetric configuration

Figure 5.5: Reshaping diagram for consecutive reshaping steps: comparison between the curves with RS and under the RSF hypothesis.

5.5 Reshaping as a root-finding problem

Thanks to the local definition of δ introduced in section 5.2, it is possible to consider reshaping as a root-finding problem. Now, the configuration where distortion is minimized is the equivalent of finding the location where the distance d, measured from the location of where the load is applied u_l respect to the location of the support rollers u_s, is zero, as expressed in the following formula:

$$d = u_l - u_s \tag{5.2}$$

As the region where the support rollers are located acts as a locus, where the beam pivots and provides a constant reference, u_s is zero. Now, as the absolute value hidden in the definition of Equation 5.1 is no longer available, the sign of d provides information regarding the repaired geometry and when to stop the process by considering the following cases:

$$d \rightarrow \begin{cases} < 0 & \text{distortion is convex } \cup \\ = 0 & \text{distortion is minimized } \sim \\ > 0 & \text{distortion is concave } \cap \end{cases}$$

The advantage of this new criteria is that the optimum stroke is not located anymore in a kink region, providing a smooth solution, as can be seen depicted with orange dashed lines in Figures 5.2 to 5.4 (right). Additionally, from the numerical point of view, the optimum configuration can be found by applying an alternative method (e.g, the secant method) and used to compare the solution to the one provided by the SSL. By using the root-finding problem as a reference, the error of the ROM solution can be estimated, as explained in the following paragraph. As a drawback, we can state that this criterion has no physical meaning as the amplitude of the remaining wave is not considered anymore.

Once the distance criteria is defined, the Secant Method [74] is selected to solve again the reshaping problem and is used as a benchmark. A tolerance of 10^{-3} is chosen as a stop criteria, consistently with Abaqus solver tolerance for non-linear problems [106]. Then the SSL is performed for different hierarchy levels k and the optimum stroke y_s^{opt} is calculated for each case. Finally, the relative error ε_{rel} is obtained by using the following expression:

$$\varepsilon_{rel} = \frac{y_s^{opt}|_{ref} - y_s^{opt}|_{SSL}}{y_s^{opt}|_{ref}} \tag{5.3}$$

Algorithm 3 Secant method applied to reshaping

procedure RESHAPINGSECANTMETHOD.PY
    problem setup $\leftarrow x_0, x_1, y_0 = f(x_0), y_1 = f(x_1)$ and tol
    $n \coloneqq 0 \leftarrow$ initialize the problem
repeat:
    $n \coloneqq n + 1$
    $x_{n+1} \coloneqq x_n - \frac{x_n - x_{n-1}}{y_n - y_{n-1}} y_n \leftarrow$ find the next point
    $y_{n+1} \coloneqq f(x_{n+1}) \leftarrow$ evaluate the next point
until:
    $|y_{n+1}| \leq$ tol
end procedure

With the aim to keep the standard notation for the secant method described in algorithm 3, the stroke y_s corresponds to the abscissas so that the extremes of the interval to explore y_s^{min} and y_s^{max} are x_0 and x_1, respectively. On the other hand, the evaluation of function $y = f(x)$ corresponds to Equation 5.2 that is found as a post-process of the associated `.ODB` file[2] after the reshaping operation is done.

As a remark, the following error estimation analysis were performed only for the RS case, as they were used as a source to provide the geometry input for the RSF analysis presented previously.

5.5.1 First step: Error estimation

The evolution of the relative error against the hierarchy level during the first reshaping step is depicted in Figure 5.6a. Here, it can be seen that for a level $k = 3$, the error is stabilized. This hierarchy level is selected for the calculations performed. As a trade-off solution, the relative error of 10^{-2} is validated for the answer provided by the ROM.

5.5.2 Second step: Error estimation

After comparing both configurations for the second reshaping step, the non-symmetric set-up is chosen and used to run the error estimation. The analysis is performed in the following manner: as a reference solution, starting with the optimum set-up provided by the Secant Method, the SSL is launched to find the new stroke for the

[2] Abaqus result file, Abaqus Output Data Base

Table 5.3: Error estimation set-up for the second reshaping step

Description	First step	Second step
Reference solution	Secant Method	SSL
ROM solution	SSL	SSL

second reshaping step. Then, the same analysis is done but using as a starting point the configuration provided previously by the SSL. A summary of the used set-up is presented in Table 5.3. The idea is to compare the effect of an initial error in the distorted shape and how it affect the solution provided by the ROM.

The error estimation results for the second reshaping step are depicted in Figure 5.6b, where it can be seen that a hierarchy level $k = 2$ is able to reach a similar error level compared to the first step (see Figure 5.6a). Therefore, a hierarchy level $k = 3$ continues to be a good choice for the performed simulations.

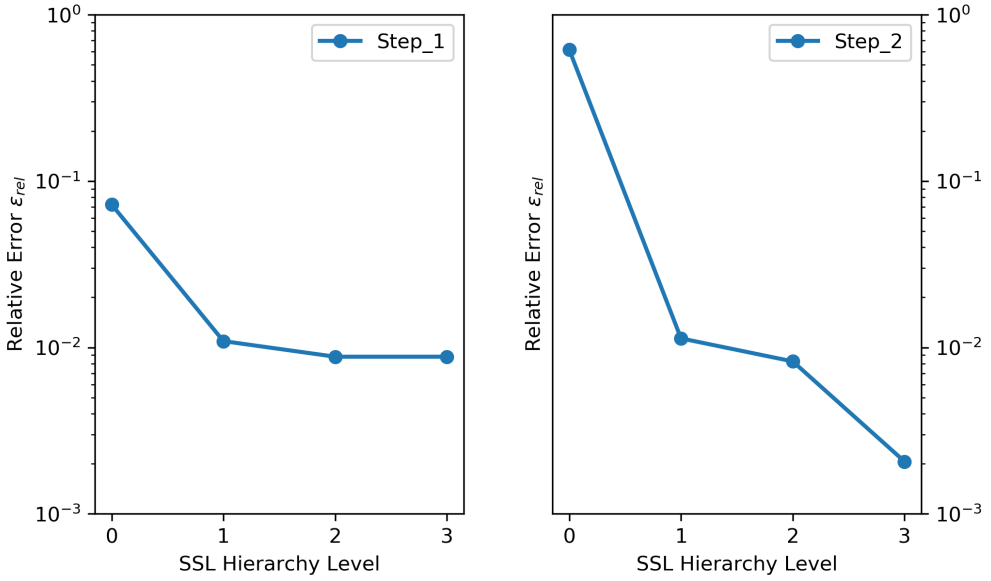

(a) Step 1

(b) Step 2 (non-symmetric)

Figure 5.6: Multiple bending straightening operations: error estimation.

5.6 Process signature

After running the simulation of the first two steps and evaluate different reshaping strategies during the second operation, we can formulate reshaping as the summation of displacement fields done after machining $u_{reshaping}$ whose goal is to compensate the initial displacement field caused by the residual stresses $u_{distortion}$, as following:

$$u_{distortion} + \sum_{i=1}^{n} u_{reshaping} \leq tol \tag{5.4}$$

In an ideal scenario, if $u_{distortion}$ could be mimic perfectly, one single operation would be sufficient to repair the part. However, when analyzing the displacement field generated in a three-point bending configuration, it can be seen that the process is only able to produce an imposed vertical displacement with a triangular shape that is driven by the rotation of the plastic hinge, located in the zone where the load is applied, as depicted in Figure 5.7. Here, it can be appreciated how the amplitude of the wave can be reached while the zones outside the triangular pattern correspond to the remaining distortion for the successive reshaping steps.

This characteristic shape of the displacement field is referred to as the *process signature* and can be used to model in a qualitative way the evolution of distortion for consecutive reshaping operations. An example of the application of this idea is represented in Figure 5.8. Here, it can be appreciated how the remaining distortion evolves along the reshaping process (Figure 5.8a) and the different displacement fields imposed at each step (Figure 5.8b). The first reshaping step is done in one single operation while to complete the second reshaping step, three operations are required. The full sequence for the second reshaping step can be described as:

- Step 2.1: The left portion of the wave is repaired. The reduction of distortion in the treated zone generates the rotation of the right half of the beam, as explained in section 5.3.2.
- Step 2.2: The right portion of the wave is repaired. Now the left half experiences the rigid solid rotation. As a consequence, a symmetric distortion pattern is obtained. At an operational level, the part needs to be repositioned as a consequence of the rotation experienced in Step 2.1.
- Step 2.3: The whole beam is repaired. If we compare the initial shape with the *temp3* geometry (see Figure 5.8a), it can be noticed that the form is closer

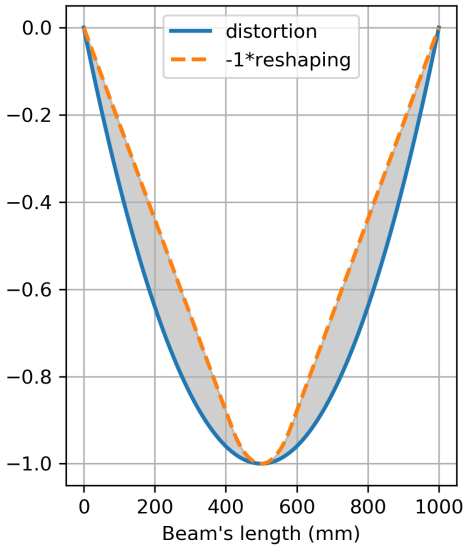

Figure 5.7: Process signature's scheme for bending straightening: comparison between a generic distorted geometry against the available imposed displacement.

to a triangular shape instead of the starting parabolic curve, therefore, it is expected to repair the part in a major degree.

The complexity of reshaping increases while the process goes along. As the remaining distortion decreases, it is more difficult to repair the part as the zone involved gets smaller too and more operations are required to migrate from a wavy shape to a triangular pattern. By analysing the sequence of reshaping operations, it is found that for each repaired wave n, $2n$ smaller waves are generated by manipulating the part with $2n - 1$ operations. A summary for all the processes up until the third bending straightening step is provided in Table 5.4.

Thanks to the *process signature* approach, it is possible to know the right sequence of operations in advance. Then, to validate the previous result, the reshaping simulations were done by applying the SSL in a sequential way. This means that, for each operation and a fixed level of hierarchy $k = 3$, 9 simulations were required before finding y_s^{opt}. Once the optimum stroke is known, an extra simulation with the optimum parameters is needed to start the next iteration. The result is shown in Figure 5.9 and a good agreement is found with respect to the qualitative model

Table 5.4: Required operations as a function of waves number n

Step	1	2	3	...	i
Waves number	1	2	4	...	n
Required operations	1	3	7	...	$2n-1$

represented in Figure 5.8.

The described approach takes as the main input the remaining distortion δ_i at step i and provides the estimation for the next reshaping step $i+1$, giving as an output δ_{i+1}, as shown in Figure 5.10a. This strategy presents the drawback that the next reshaping step cannot be launched before the new distorted geometry is known, which limits the application of the model to a few steps. As a future development, it would be interesting to explore the possibility to generate a more generic MOR that uses the idea of the *process signature*. By knowing in advance the shape and amplitude of the displacement field, a feedback loop can be included such that the generated remaining distortion δ_{i+1} is plugged in directly for the next iteration, as represented in Figure 5.10b.

5.7 Conclusions

In the present chapter, the evolution of distortion for two consecutive bending straightening operations was studied. This task was done as a direct application of the ideas presented in chapter 3 in combination with the ROM developed in 4.

With the aim to generalize the RSF hypothesis, it was tested and validated for different consecutive configurations. During the process, it was found that the complexity of the reshaping problem is incremented as the operation advances in time. Then, when the part is repaired locally, the global effects must be taken into account too.

Thanks to the Model Order Reduction approach in combination with the RSF hypothesis and the process signature idea, it was possible to isolate the effects of each reshaping step. In that way, a methodology to perform a series of bending straightening operations was proposed, where the non-symmetric configuration was chosen over the symmetric setup for the second step.

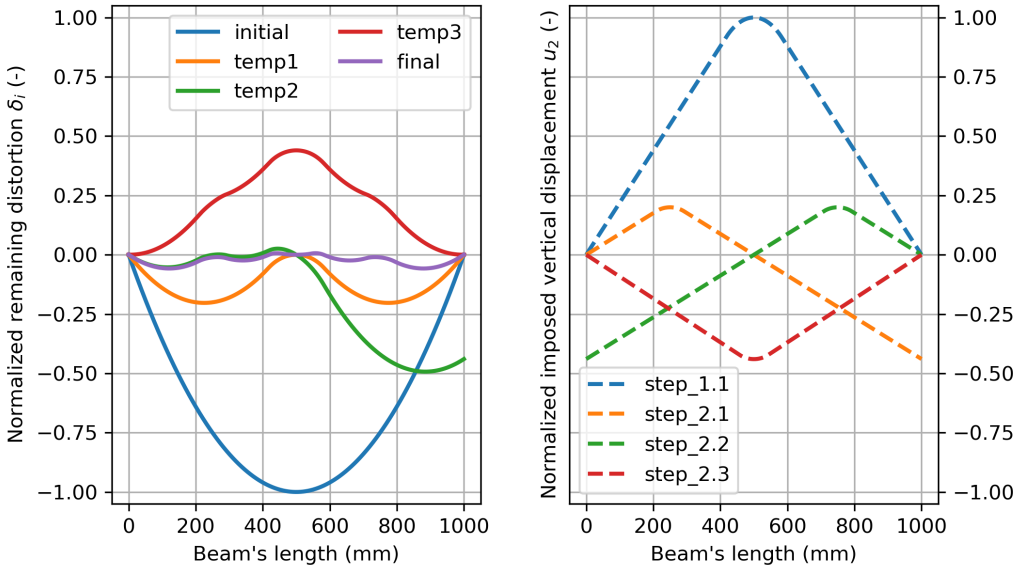

(a) (b)

Figure 5.8: Theoretical process signature for bending straightening applied to two complete reshaping steps. (a) Normalized remaining distortion δ_i. (b) Normalized imposed vertical displacement u_2.

Finally, based on the wavy pattern developed after each reshaping step, the possibility to model distortion as a sinusoidal function with n periods needs to be explored as future work. This parametrization could be useful to develop the idea of a MOR with feedback to overcome the current limitation of the presented sequential MOR.

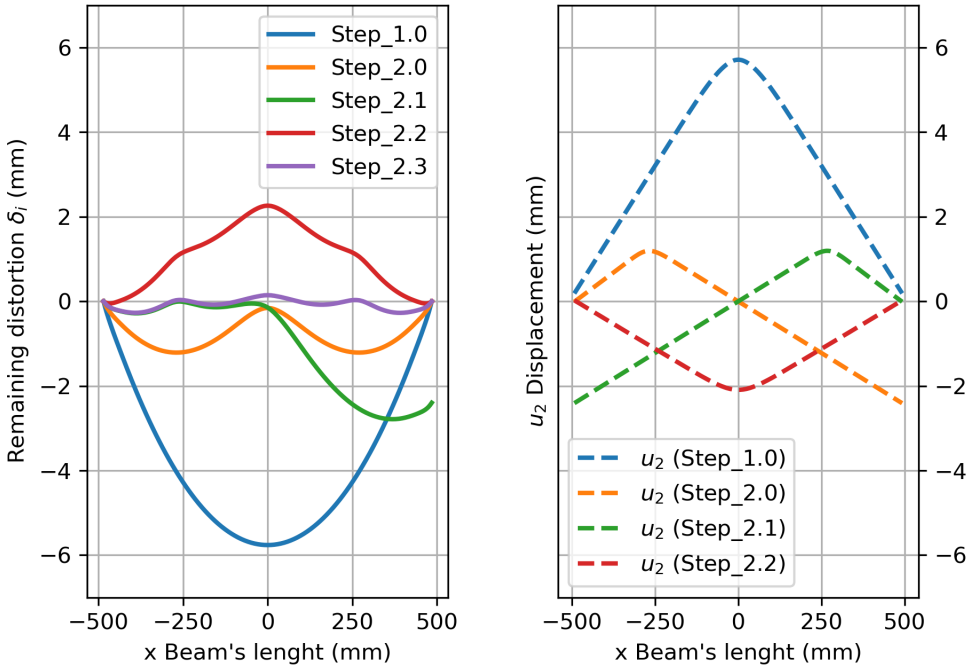

(a) (b)

Figure 5.9: Distortion evolution during reshaping (simulation results). (a) Remaining distortion δ_i. (b) Imposed vertical displacement u_2 for each reshaping step.

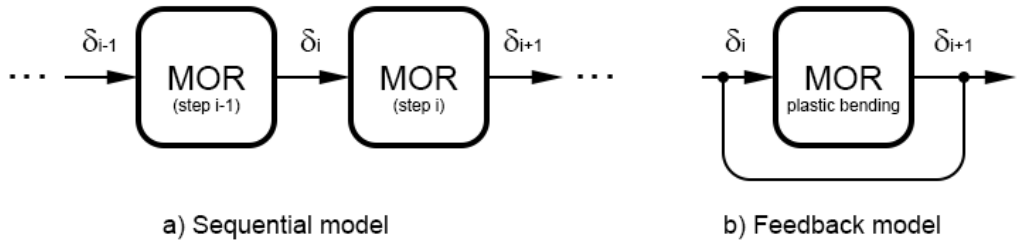

Figure 5.10: Model Order Reduction strategies for reshaping. a) Sequential model (implemented) and b) Feedback model (future work).

Conclusions and perspectives

Scientific contributions

This thesis was devoted to the numerical study of the bending straightening operation to mitigate the post-machining distortion of large aluminium forgings. The contributions of this work can be summarized by the answers given to the following research questions:

- What is the influence of residual stresses during reshaping?
- Which is the most important parameter for bending straightening?
- Which is the best reshaping strategy for multiple bending straightening operations?

To tackle the first question, in chapter 3, we introduced the reshaping diagrams. This tool allowed us to compare the behaviour of the real forge with and without residual stresses. It was found that, by neglecting the internal residual stresses (under the residual stress free hypothesis), a similar behaviour was obtained in terms of distortion mitigation with an offset. Then, to retrieve the original curve, only force-displacement measurements are required. Although reshaping is mainly driven by plastic phenomena, a history-dependent material problem [35] in nature, this simplification hypothesis allows to focus the simulation resources on the reshaping step only, instead of solving the whole manufacturing history. Up to this point, traditional Finite Element Analysis tools were used.

Regarding the multi-parametric analysis of a single bending straightening operation, discussed in chapter 4, it was shown that the initial distortion δ_0 is the main parameter for the problem, since the required stroke y_s to be applied can be fully

determined, for any previously defined roller position r_e. In addition, the generalization of the reshaping diagram in the form of a response surface allowed us to explain a paradoxal behaviour: it is more difficult to repair a smaller distortion respect to a bigger one. This behaviour, already reported by boilermakers [66], can be interpreted now as follows: when distortions are small, the required stroke to repair the part gets closer to the minimum stroke to produce plasticity, and its accurate prediction becomes sensitive to uncertainties. On the contrary, it is easier to find the optimum distortion away from the critical area, in the domain of higher strokes. The multi-parametric analysis was possible thanks to the use of the Sparse Subspace Learning Method, which proved itself as a powerful Model Order Reduction technique to be used in an industrial environment. As a remark, with the aim to enhance these results, future work is needed as all the simulations were done under the assumption of constant material properties. This analysis could provide some hints about the distortion variability.

For the different consecutive bending straightening operations, compared in chapter 5, the non-symmetric option provides more flexibility with respect to the symmetric counterpart. While the latter takes advantage of the longitudinal symmetry by keeping track of the crests and valleys developed during the first reshaping step and uses them as a criteria to place the rollers to perform the next operation, the former strategy is more practical as it follows a pattern each time a reshaping operation is done that can be summarized as *divide and conquer*. Then, in combination with the proposed *process signature* for bending straightening, it is possible to determine in advance the required sequence to repair a part. However, one limitation to this approach is that it was developed for a single initial distortion δ_0, therefore, more work is required to generalize this analysis for multiple parameters.

Future works

Although the problem of reshaping remains still open, after finishing this project, besides the previous suggested improvements, different scenarios for future works are discussed bellow.

In this thesis, from the four available reshaping operations described in chapter 1, only bending straightening was analysed, therefore, the next logical step is to test the reshaping diagrams and the residual stress free hypothesis in the other remaining

operations. Plastic torsion is a strong candidate to consider as this technique presents some similarities respect to bending straightening, e.g. the development of plastic zones in the external fibres and the important presence of spring-back phenomenon.

Another work to be done in the short-term is the generalization of the remaining distortion criteria. The rule presented in here was developed for straight geometries, however, some cruciform beams present a curvature along its longitudinal axis. Maybe the *local* definition of distortion discussed in chapter 5 could be used as a guide to obtain a repaired curved part as the sum of repaired straight segments.

When it comes to a possible application for this research, training of boilermakers is one option to explore in the mid-term. Currently, it takes 2 years to teach a technician how to properly repair a part. This constitutes an access barrier to any person interested to work in the field and an important cost as normally an experienced boilermaker supervises the learning process. In addition, while the iterative nature of reshaping acts as the drawback during the learning period, this represents an advantage when the process is virtually analysed as it is possible to track, study, and isolate the effects of one single reshaping operation. The work performed by Badias et al, [7] mixing augmented reality with Model Order Reduction techniques can be used as a guideline for this purpose.

Finally, in a long-term scenario, it must be noticed that numerical simulation is only one of the multiple ingredients needed to tackle the reshaping problem efficiently. In the daily industrial environment of Airbus, new techniques to measure the evolution of distortion in real-time are required, in order to track the repairing process from the beginning to the end. Then, this information could be used to update/enrich a reshaping simulation, following the philosophy of data assimilation techniques which are successfully applied in weather forecasting [85].

Final remarks

As a closing remark, maybe at first sight the action to *repair* something could be considered unappealing for the research community, as it can be seen as a non-added value work or the lack of interest/literature might be caused by the current notion that it is cheaper to replace something instead of investing time and effort to fix it. However, in the same way as reshaping poses a serious problem for the aeronautical industry, not only in economical terms, there is space for improvements in different

research fields, e.g. at a numerical level there is a need to study the distortion problem in a probabilistic framework with the aid of an efficient algorithm, or the demand at experimental level to develop a non-destructive technique to measure residual stresses in an industrial context. Although no final solution to the reshaping problem was proposed, it is the hope of the author to bring back interest in this field, where this work could provide a first step towards this direction.

Bibliography

[1] Abdulle, A. and Bai, Y. (2014). Reduced-order modelling numerical homogenization. *Philosophical Transactions of the Royal Society A: Mathematical, Physical and Engineering Sciences*, 372(2021). *cited on page 54*

[2] Aguado, J. V., Huerta, A., Chinesta, F., and Cueto, E. (2015). Real-time monitoring of thermal processes by reduced-order modeling. *International Journal for Numerical Methods in Engineering*, 102(5):991–1017. *cited on page 57, 64 and 66*

[3] Akkurt, A. (2011). Comparison of roller burnishing method with other hole surface finishing processes applied on aisi 304 austenitic stainless steel. *Journal of Materials Engineering and Performance*, 20(6):960–968. *cited on page ix, 12 and 13*

[4] Ammar, A., Mokdad, B., Chinesta, F., and Keunings, R. (2006). A new family of solvers for some classes of multidimensional partial differential equations encountered in kinetic theory modeling of complex fluids. *Journal of Non-Newtonian Fluid Mechanics*, 139(3):153–176. *cited on page 55 and 63*

[5] Antil, H. and Heinkenschloss, Matthias Sorensen, D. C. (2014). Application of the Discrete Empirical Interpolation Method to Reduced Order Modeling of Nonlinear and Parametric Systems. In Quarteroni, A. and Rozza, G., editors, *Reduced Order Methods for Modeling and Computational Reduction.*, chapter 4, pages 101–136. Springer Cham, ms&a 9 edition. *cited on page 67*

[6] ASME (1983). The Wyman-Gordon 50,000-Ton Forging Press. Technical report, The American Society of Mechanical Engineers (ASME). *cited on page 7*

[7] Badías, A., Alfaro, I., González, D., Chinesta, F., and Cueto, E. (2018). Reduced order modeling for physically-based augmented reality. *Computer Methods in Applied Mechanics and Engineering*, 341(1):53–70. *cited on page 105*

[8] Ball, D., Dubowski, D., and Spradlin, T. (2016). Inclusion of Forging Residual Stresses in Large Component Structural Design. In *2016 USAF Aircraft Structural Integrity Program Conference*. *cited on page 8*

[9] Banabic, D. (2010). *Sheet Metal Forming Processes: Constitutive Modelling and Numerical Simulation*. Springer. *cited on page 43*

[10] Banks, H. T., Del Rosario, R. C., and Tran, H. T. (2002). Proper orthogonal decomposition-based control of transverse beam vibrations: Experimental implementation. *IEEE Transactions on Control Systems Technology*, 10(5):717–726. *cited on page 60*

[11] Barroso, G., Gil, A. J., Ledger, P. D., Mallett, M., and Huerta, A. (2020). A regularised-adaptive Proper Generalised Decomposition implementation for coupled magneto-mechanical problems with application to MRI scanners. *Computer Methods in Applied Mechanics and Engineering*, 358:112640. *cited on page 66*

[12] Bellman, R. (1961). *Adaptive Control Processes: A Guided Tour*. Princeton University Press, New Jersey. *cited on page 54 and 55*

[13] Benner, P., Gugercin, S., and Willcox, K. (2015). A survey of projection-based model reduction methods for parametric dynamical systems. *SIAM Review*, 57(4):483–531. *cited on page xi, 58, 61 and 71*

[14] Borzacchiello, D., Aguado, J. V., and Chinesta, F. (2017a). Non-intrusive Sparse Subspace Learning for Parametrized Problems. *Archives of Computational Methods in Engineering*, pages 1–24. *cited on page 2, 4 and 67*

[15] Borzacchiello, D., Aguado, J. V., and Chinesta, F. (2017b). Reduced order modelling for efficient numerical optimisation of a hot-wall chemical vapour deposition reactor. *International Journal of Numerical Methods for Heat and Fluid Flow*, 27(7):1602–1622. *cited on page 71*

[16] Buljak, V. (2012). *Inverse Analyses with Model Reduction: Proper Orthogonal Decomposition in Structural Mechanics*, volume 53. Springer-Verlag Berlin. *cited on page 60*

[17] Canales, D. (2017). *Stratégies numériques avanées pour la simulation efficace de procédés de soudage conventionnels et non conventionnels: Une approche de réduction de modèles*. PhD thesis, Ecole Centrale de Nantes. *cited on page 58*

[18] Canales, D., Leygue, A., Chinesta, F., González, D., Cueto, E., Feulvarch, E., Bergheau, J.-M., and Huerta, A. (2016). Vademecum-based GFEM (V-GFEM): optimal enrichment for transient problems. *International*, 108:971–989. *cited on page 70*

[19] Cerutti, X. (2014). *Numerical modelling and mechanical analysis of the machining of large aeronautical parts: Machining quality improvement*. PhD thesis, Ecole Nationale Supérieure des Mines de Paris. *cited on page ix, 14, 15, 18 and 19*

[20] Cerutti, X., Mocellin, K., Hassini, S., Blaysat, B., and Duc, E. (2017). Methodology for aluminium part machining quality improvement considering mechanical properties and process conditions. *CIRP Journal of Manufacturing Science and Technology*, 18:18–38. *cited on page 14*

[21] Chaboche, J.-L. (1986). Time-independent constitutive theories for cyclic plasticity. *International Journal of Plasticity*, 2(2):149–188. *cited on page 24 and 25*

[22] Chakrabarti, D. J., Weiland, H., Cheney, B. A., and Staley, J. T. (1996). Through thickness property variations in 7050 plate. *Materials Science Forum*, 217-222(PART 2):1085–1090. *cited on page 23*

[23] Chantzis, D., Van-Der-Veen, S., Zettler, J., and Sim, W. M. (2013). An industrial workflow to minimise part distortion for machining of large monolithic components in aerospace industry. *Procedia CIRP*, 8:281–286. *cited on page 14*

[24] Chatterjee, A. (2000). An introduction to the proper orthogonal decomposition. *Current Science*, 78(7):808–817. *cited on page 59*

[25] Chaturantabut, S. and Sorensen, D. C. (2009). Nonlinear model reduction via discrete empirical interpolation. In *Proceedings of the 48h IEEE Conference on Decision and Control (CDC) held jointly with 2009 28th Chinese Control Conference*, volume 32, pages 4316–4321, Shanghai. IEEE. *cited on page 58, 66 and 67*

[26] Chinesta, F., Keunings, R., and Leygue, A. (2014). *The proper generalized decomposition for advanced numerical simulations: A primer*. Springer International Publishing, 1 edition. *cited on page 55 and 64*

[27] Chinesta, F., Leygue, A., Bordeu, F., Aguado, J. V., Cueto, E., Gonzalez, D., Alfaro, I., Ammar, A., and Huerta, A. (2013). PGD-Based Computational Vade-

mecum for Efficient Design, Optimization and Control. *Archives of Computational Methods in Engineering*, 20(1):31–59. *cited on page 16, 53 and 66*

[28] Christopherson, D. G. (1940). A Theoretical Investigation of Plastic Torsion in an I-Beam. *The Aeronautical Journal*, 44(353):425–432. *cited on page 12*

[29] Cohen, A. and Devore, R. (2015). Approximation of high-dimensional parametric PDEs. *Acta Numerica*, 24:1–159. *cited on page 56 and 57*

[30] Coules, H. E., Horne, G. C., Kabra, S., Colegrove, P., and Smith, D. J. (2017). Three-dimensional mapping of the residual stress field in a locally-rolled aluminium alloy specimen. *Journal of Manufacturing Processes*, 26:240–251. *cited on page 12*

[31] Cueto, E. and Chinesta, F. (2014). Real time simulation for computational surgery: a review. *Advanced Modeling and Simulation in Engineering Sciences*, 1(1):1–18. *cited on page 55*

[32] Cueto, E., González, D., and Alfaro, I. (2016). *Proper Generalized Decomposition: An Introduction to Computer Implementation with Matlab*. Springer. *cited on page 66 and 71*

[33] Davidson, P. (2015). *Turbulence: An Introduction for Scientists and Engineers*. Oxford University Press, Oxford, 2nd edition. *cited on page 54*

[34] De Jong, H. F. (1980). Thickness direction inhomogeneity of mechanical properties and fracture toughness as observed in aluminum 7075-T651 plate material. *Engineering Fracture Mechanics*, 13(1):175–192. *cited on page 23*

[35] de Souza Neto, E. A., Peric, D., and Owen, D. R. J. (2008). *Computational Methods for Plasticity*. Wiley. *cited on page 103*

[36] Deloison, D. and Congourdeau, F. (2016). Airbus A380 Fatigue test plan. Technical report, Airbus Central Research and Technology, Suresnes. *cited on page xiii and 26*

[37] Dokšanović, T., Džeba, I., and Markulak, D. (2017). Variability of structural aluminium alloys mechanical properties. *Structural Safety*, 67:11–26. *cited on page 74*

[38] Dreier, S., Brüning, J., and Denkena, B. (2016). Simulation based reduction of residual stress related part distortion. *Materialwissenschaft und Werkstofftechnik*, 47(8):710–717. *cited on page 1, 3 and 35*

[39] Du, J., Deng, Q., Dong, J., Xie, X., Wang, Z., Zhao, C., Chen, G., Xie, W., Luo, T., Wang, X., and Zhang, Y. (2014). Recent Progess of Manufacturing Technologies on C&W Superalloys in China. In Ott, E., Banik, A., Liu, X., Dempster, I., Heck, K., Andersson, J., Groh, J., Gabb, T., Helmink, R., and Wusatowska-Sarnek, A., editors, *8th International Symposium on Superalloy 718 and Derivatives*, pages 33–46. TMS (The Minerals, Metals & Materials Society). *cited on page 7*

[40] Dux, T. (2018). Forging of Aluminum Alloys. In Anderson, K., Weritz, J., and Kaufman, J. G., editors, *Aluminum Science and Technology*, volume 14, pages 315–335. ASM International. *cited on page 18*

[41] Ellermann, A. and Scholtes, B. (2012). Residual stress states as a result of bending and straightening processes of steels in different heat treatment conditions. *International Journal of Materials Research*, 103(1):57–65. *cited on page 11*

[42] EN-1999-1-1 (2007). Eurocode 9: Design of aluminium structures - Part 1-1: General structural rules. *cited on page 86*

[43] Forrest, G. (1954). Internal or Residual Stresses in Wrought Aluminium Alloys and their Structural Significance. *Journal of the Royal Aeronautical Society*, pages 261–276. *cited on page ix, 7, 13 and 43*

[44] Ghasemi, M., Yang, Y., Gildin, E., Efendiev, Y., and Calo, V. (2015). Fast multiscale reservoir simulations using POD-DEIM model reduction. In *SPE Reservoir Simulation Symposium 2015*, volume 2, pages 1393–1410, Houston. Society of Petroleum Engineers. *cited on page 67*

[45] Ghavamian, F., Tiso, P., and Simone, A. (2017). PODâ€“DEIM model order reduction for strain softening viscoplasticity. *Computer Methods in Applied Mechanics and Engineering*, 317:458–479. *cited on page 67*

[46] Giacoma, A., Dureisseix, D., and Gravouil, A. (2016). An efficient quasi-optimal space-time PGD application to frictional contact mechanics. *Advanced Modeling and Simulation in Engineering Sciences*, 3(1). *cited on page 70*

[47] guang Li, J. and qi Wang, S. (2017). Distortion caused by residual stresses in machining aeronautical aluminum alloy parts: recent advances. *International Journal of Advanced Manufacturing Technology*, 89(1-4):997–1012. *cited on page 36*

[48] Gutierrez-Castillo, P. and Thomases, B. (2019). Proper Orthogonal Decomposition (POD) of the flow dynamics for a viscoelastic fluid in a four-roll mill geometry at the Stokes limit. *Journal of Non-Newtonian Fluid Mechanics*, 264(September 2018):48–61. *cited on page 60*

[49] Haasdonk, B. (2016). Reduced Basis Methods for Parametrized PDEs - A Tutorial Introduction for Stationary and Instationary Problems. In Benner, P., Cohen, A., Ohlberger, M., and Willcox, K., editors, *Model Reduction and Approximation: Theory and Algorithms*. SIAM, Philadelphia. *cited on page xi, 57, 58 and 63*

[50] Hardt, D. E., Constantine, E., and Wright, A. (1992). A Model of the Sequential Bending Process for Manufacturing Simulation. *Journal of Engineering for Industry*, 114:181–187. *cited on page xi, xiii, 72 and 73*

[51] Iványi, M. (1969). Effect of strain-hardening on the elastic-plastic behaviour of beams. *Periodica Polytechnica Civil Engineering*, 13(3-4):125–130. *cited on page 72*

[52] Jeanmart, P. and Bouvaist, J. (1985). Finite element calculation and measurement of thermal stresses in quenched plates of high-strength 7075 aluminium alloy. *Materials Science and Technology*, 1(October):765–769. *cited on page xiii, 8, 18, 19, 21, 22 and 23*

[53] Kalpakjian, S. and Steven, S. (2014). *Manufacturing Processes for Engineering Materials*. 7th edition. *cited on page 6*

[54] Katoh, T., Urata, E., Nakanishi, M., and Yamazaki, K. (1991). Control for Straightening Process of Seamless Pipe. *JSME*, 34(3):427–432. *cited on page 43*

[55] Koç, M., Culp, J., and Altan, T. (2006). Prediction of residual stresses in quenched aluminum blocks and their reduction through cold working processes. *Journal of Materials Processing Technology*, 174(1-3):342–354. *cited on page 26*

[56] Ladevèze, P. (1985). Sur une famille d'algorithmes en mécanique des structures. *Comptes-rendus des séances de l'Académie des sciences. Série 2, Mécanique-physique, chimie, sciences de l'univers, sciences de la terre*, 300(2):41–44. *cited on page 63*

[57] Lassila, T., Manzoni, A., Quarteroni, A., and Rozza, G. (2014). Model Order Reduction in Fluid Dynamics: Challenges and Perspectives. In Quarteroni, A. and Rozza, G., editors, *Reduced Order Methods for Modeling and Computational Reduction*, chapter 9, pages 235–273. Springer International Publishing. *cited on page 54*

[58] Lauzeral, N., Borzacchiello, D., Kugler, M., George, D., Remond, Y., Hostettler, A., and Chinesta, F. (2019). Shape parametrization of bio-mechanical finite element models based on medical images. *Computer Methods in Biomechanics and Biomedical Engineering: Imaging & Visualization.* *cited on page 50 and 76*

[59] Lazoglu, I., Ulutan, D., Alaca, B. E., Engin, S., and Kaftanoglu, B. (2008). An enhanced analytical model for residual stress prediction in machining. *CIRP Annals - Manufacturing Technology*, 57:81–84. *cited on page 35*

[60] Liu, L., Sun, J., Chen, W., and Sun, P. (2017). Study on the machining distortion of aluminum alloy parts induced by forging residual stresses. *Proceedings of the Institution of Mechanical Engineers, Part B: Journal of Engineering Manufacture*, 231(4):618–627. *cited on page 36*

[61] Lumley, J. (1967). The structure of inhomogeneous turbulent flows. *Atmospheric Turbulence and Radio Wave Propagation.* *cited on page 59*

[62] Ma, K., Goetz, R., and Srivatsa, S. K. (2010). Modeling of Residual Stress and Machining Distortion in Aerospace Components. In Furrer, D. and Semiatin, S., editors, *Metals Process Simulation*, pages 386–407. ASM International. *cited on page 6, 8, 18, 19 and 35*

[63] Madariaga, A., Perez, I., Arrazola, P. J., Sanchez, R., Ruiz, J. J., and Rubio, F. J. (2018). Reduction of distortions in large aluminium parts by controlling machining-induced residual stresses. *International Journal of Advanced Manufacturing Technology*, 97(1-4):967–978. *cited on page 35*

[64] Manzoni, A., Pagani, S., and Lassila, T. (2016). Accurate solution of Bayesian inverse uncertainty quantification problems combining reduced basis methods and reduction error models. *SIAM-ASA Journal on Uncertainty Quantification*, 4(1):380–412. *cited on page 54*

[65] Marin, G. (2000). *Calcul et optimisation des structures mécaniques*. PhD thesis, Université Technologique Compiègne. *cited on page ix, 9 and 10*

[66] Mena, R. (2018). Reshaping operations at Airbus Operations Nantes. Technical report, Airbus SAS, Nantes. *cited on page 89 and 104*

[67] Mitze, M. (2010). Straightening heat-treated components. *Journal of Heat Treatment and Materials*, 65:110–117. *cited on page 8*

[68] Murthy, R. L. and Kotiveerachari, B. (1981). Burnishing of metallic surfaces - a review. *Precision Engineering*, 3:172–179. *cited on page 12*

[69] Narahari Prasad, S., Rambabu, P., and Eswara Prasad, N. (2017). Processing of Aerospace Metals and Alloys: Part 2 - Secondary Processing. In Prasad, N., Eswara, and Wanhill, R., editors, *Aerospace Materials and Material Technologies*, volume 2, pages 199–228. Springer Singapore. *cited on page 6*

[70] Nasri, M. A., Aguado, J. V., Ammar, A., Cueto, E., Chinesta, F., Morel, F., Robert, C., and Elarem, S. (2015). Separated representation of incremental elastoplastic simulations. *Key Engineering Materials*, 651-653:1285–1293. *cited on page 69*

[71] Niroomandi, S., González, D., Alfaro, I., Bordeu, F., Leygue, A., Cueto, E., and Chinesta, F. (2013). Real-time simulation of biological soft tissues: a PGD approach. *International Journal for Numerical Methods in Biomedical Engineering*, 29(5):586–600. *cited on page 66*

[72] Nouy, A. (2010). Proper Generalized Decompositions and Separated Representations for the Numerical Solution of High Dimensional Stochastic Problems. *Archives of Computational Methods in Engineering*, 17(4):403–434. *cited on page 66*

[73] Ohlberger, M. and Rave, S. (2016). Reduced basis methods: success, limitations and future challenges. In Ševčovič, A. and Handlovičová, D., editors, *Proceedings Of The Conference Algoritmy*, pages 1–12, Podbanské. *cited on page 63*

[74] Phillips, G. and Taylor, P. (1996). Solution of Algebraic Equations of one Variable. In *Theory and Applications of Numerical Analysis*, chapter 8, pages 196–220. Academic Press, London, second edi edition. *cited on page 95*

[75] Pi, Y. L. and Trahair, N. S. (1995). Inelastic Torsion of Steel I-Beams. *Journal of Structural Engineering*, 121(4):609–620. *cited on page 12*

[76] Portier, L., Calloch, S., Marquis, D., and Geyer, P. (2000). Ratchetting under tension-torsion loadings: Experiments and modelling. *International journal of plasticity*. *cited on page 24*

[77] Poulhaon, F., Rauch, M., Leygue, A., Hascoet, J. Y., and Chinesta, F. (2014). Online Prediction of Machining Distortion of Aeronautical Parts Caused by Re-Equilibration of Residual Stresses. *Key Engineering Materials*, 611-612:1327–1335. *cited on page 69*

[78] Prime, Michael B; Hill, M. (2002). Residual Stress, Stress Relief, and Inhomogeneity in Aluminum Plate. *Scripta Materialia*, 46:77–82. *cited on page ix, 19, 20, 23 and 27*

[79] Prud'homme, C., Rovas, D. V., Veroy, K., Machiels, L., Maday, Y., Patera, A. T., and Turinici, G. (2002). Reliable real-time solution of parametrized partial differential equations: Reduced-basis output bound methods. *Journal of Fluids Engineering, Transactions of the ASME*, 124(1):70–80. *cited on page 60*

[80] Quaranta, G., Haug, E., Louis, J., and Francisco, D. (2020). Parametric evaluation of part distortion in additive manufacturing processes. *International Journal of Material Forming*, pages 29–41. *cited on page 70*

[81] Quarteroni, A., Manzoni, A., and Negri, F. (2016). *Reduced basis methods for partial differential equations: An introduction*. *cited on page 61 and 63*

[82] Raghavan, B., Le Quilliec, G., Breitkopf, P., Rassineux, A., Roelandt, J. M., and Villon, P. (2014). Numerical assessment of springback for the deep drawing process by level set interpolation using shape manifolds. *International Journal of Material Forming*, 7(4):487–501. *cited on page 70*

[83] Ramberg, W. and Osgood, W. R. (1943). Description of stress-strain curves by three parameters. *cited on page 20*

[84] Ravindran, S. S. (1999). Proper Orthogonal Decomposition in Optimal Control of Fluids. *Office*, 36(March):1174–1186. *cited on page 60*

[85] Reichle, R. H. (2008). Data assimilation methods in the Earth sciences. *Advances in Water Resources*, 31(11):1411–1418. *cited on page 105*

[86] Robinson, J. S., Cudd, R. L., Tanner, D. A., and Dolan, G. P. (2001). Quench sensitivity and tensile property inhomogeneity in 7010 forgings. *Journal of Materials Processing Technology*, 119(1-3):261–267. *cited on page 74*

[87] Robinson, J. S., Hossain, S., Truman, C. E., Paradowska, A. M., Hughes, D. J., Wimpory, R. C., and Fox, M. E. (2010). Residual stress in 7449 aluminium alloy forgings. *Materials Science and Engineering: A*, 527(10-11):2603–2612. *cited on page 6, 8, 10, 18, 19 and 23*

[88] Robinson, J. S., Tanner, D. A., and Truman, C. E. (2014). 50th anniversary article: The origin and management of residual stress in heat-treatable aluminium alloys. *Strain*, 50(3):185–207. *cited on page 8, 27 and 36*

[89] Robinson, J. S., Tanner, D. A., Truman, C. E., and Wimpory, R. C. (2011). Measurement and Prediction of Machining Induced Redistribution of Residual Stress in the Aluminium Alloy 7449. *Experimental Mechanics*, 51(6):981–993. *cited on page 18*

[90] Robinson, J. S., Tanner, D. A., Van Petegem, S., and Evans, A. (2012). Influence of quenching and aging on residual stress in Al-Zn-Mg-Cu alloy 7449. *Materials Science and Technology*, 28(4):420–430. *cited on page 36*

[91] Robinson, J. S., Wimpory, R. C., Tanner, D. A., Mooney, B., Truman, C. E., and Panzner, T. (2018). Cold Compression of 7075 and Factors Influencing Stress Relief. *Materials Performance and Characterization*, 7(4):898–911. *cited on page 36*

[92] Rutzmoser, J. B. (2018). *Model Order Reduction for Nonlinear Structural Dynamics Simulation-free Approaches*. PhD thesis, Technischen Universität München. *cited on page xi and 58*

[93] Saibaba, A. K. (2020). Randomized Discrete Empirical Interpolation Method for Nonlinear Model Reduction. *SIAM Journal on Scientific Computing*, 42(3):A1582–A1608. *cited on page 66 and 67*

[94] Sandino, C. (2019). *Global-local separated representation based on the Proper Generalized Decomposition.* PhD thesis, Ecole Centrale de Nantes. *cited on page 55 and 66*

[95] Schijve, J. (2009). Residual Stress. In *Fatigue of Structures and Materials*, pages 89–104. *cited on page 9 and 12*

[96] Schilders, W. H., van der Vorst, H. A., and Rommes, J. (2008). *Model Order Reduction: Theory, Research Aspects and Applications.* Springer-Verlag Berlin. *cited on page 54 and 55*

[97] Schott, C., Ellermann, A., Zinn, W., and Scholtes, B. (2016). Consequences of bend straightening processes on residual stresses and strength of quenched and tempered steels. *HTM - Journal of Heat Treatment and Materials*, 71(2):75–82. *cited on page 11*

[98] Seoane, M., Ledger, P. D., Gil, A. J., Zlotnik, S., and Mallett, M. (2020). A combined reduced order-full order methodology for the solution of 3D magneto-mechanical problems with application to magnetic resonance imaging scanners. *International Journal for Numerical Methods in Engineering.* *cited on page 60*

[99] Shercliff, H. R. and Ashby, M. F. (1990). A process model for age hardening of aluminium alloys-I. The model. *Acta Metallurgica Et Materialia*, 38(10):1789–1802. *cited on page 36*

[100] Sibileau, A., García-González, A., Auricchio, F., Morganti, S., and Díez, P. (2018). Explicit parametric solutions of lattice structures with proper generalized decomposition (PGD): Applications to the design of 3D-printed architectured materials. *Computational Mechanics*, 62(4):871–891. *cited on page 66*

[101] Sikström, F., Christiansson, A. K., and Lennartson, B. (2012). Model order reduction methods applied to a welding model. *Proceedings of the Institution of Mechanical Engineers. Part I: Journal of Systems and Control Engineering*, 226(7):972–984. *cited on page 70*

[102] Sim, W. M. (2008). Challenges of residual stress and part distortion in the civil airframe industry. In *2nd International Conference on Distortion Engineering*, pages 87–94. *cited on page 6, 8, 9, 14, 19, 27 and 36*

[103] Sim, W. M. (2011). Residual Stress Engineering in Manufacture of Aerospace Structural Parts. *3rd International Conference on Distorsions Engineering*, pages 187–194. *cited on page 8 and 35*

[104] Służalec, A. (1992). *Introduction to Nonlinear Thermomechanics*. Springer-Verlag London. *cited on page 19*

[105] Smith, C. and Crowther, J. (1955). The Production of Large Forgings in Aluminium Alloys. *Journal of the Royal Aeronautical Society*, 59(537):604–612. *cited on page 8*

[106] Smith, M. (2009). *ABAQUS/Standard User's Manual, Version 6.9*. Dassault Systèmes Simulia Corp. *cited on page 19, 25 and 95*

[107] Štok, B. and Halilovič, M. (2009). Analytical solutions in elasto-plastic bending of beams with rectangular cross section. *Applied Mathematical Modelling*, 33(3):1749–1760. *cited on page 72*

[108] Timoshenko, S. (1940). *Strength of Materials: Part II Advanced Theory and Problems*. D.Van Nostran Company, Inc., 2nd edition. *cited on page 12*

[109] Timoshenko, S. (1948). *Strenght of Materials*. D.Van Nostran Company, Inc., second edition. *cited on page 72*

[110] Truszkowski, W., Krol, J., and Major, B. (1980). Inhomogeneity of Rolling Texture in fcc Metals. *Metallurgical Transactions A*, 11(May):749–758. *cited on page 23*

[111] Turner, M. J., Clough, R. W., Martin, H. C., and Topp, L. J. (1956). Stiffness and Deflection Analysis of Complex Structures. *Journal of the Aeronautical Sciences*, 23(9):805–823. *cited on page 1 and 3*

[112] Wang, M. Y. and Shabeer, S. (2000). Modeling and optimization of the sequential brakeforming processes. *Journal of Materials Processing Technology*, 102(1):153–163. *cited on page xiii and 73*

[113] Weiss, J. (2019). A Tutorial on the Proper Orthogonal Decomposition. In *AIAA Aviation Forum*, number June. *cited on page 59*

[114] Withers, P. and Bhadeshia, H. (2010). Residual stress. Part 1 â€“ Measurement techniques. *Materials Science and Technology*, 17(4):355–365. *cited on page 9*

[115] Xiu, D. (2010). *Numerical Methods for Stochastic Computations : A Spectral Method Approach*. Princeton University Press, Oxford. *cited on page 54*

[116] Yin, F., Rakita, M., Hu, S., and Han, Q. (2017). Overview of ultrasonic shot peening. *Surface Engineering*, 33(9):651–666. *cited on page 12*

[117] Yu, T. X. and chi Zhang, L. (1996). *Plastic Bending: Theory and Applications*. World Scientific. *cited on page 43*

[118] Zhang, Z., Li, L., Yang, Y., He, N., and Zhao, W. (2014). Machining distortion minimization for the manufacturing of aeronautical structure. *International Journal of Advanced Manufacturing Technology*, 73(9-12):1765–1773. *cited on page 19*

[119] Zhang, Z., Yang, Y., Li, L., Chen, B., and Tian, H. (2015). Assessment of residual stress of 7050-T7452 aluminum alloy forging using the contour method. *Materials Science and Engineering A*, 644:61–68. *cited on page 19*

Appendix A

Publications

During the development of this thesis, the following documents were published as a result of the performed research.

A.1 Journals articles

- R. Mena, J.V. Aguado, S. Guinard, A. Huerta, Reshaping diagrams for bending straightening of forged aeronautical components, *International Journal of Advanced Manufacturing Technology*, 110, 1485-1502 (2020); https://doi.org/10.1007/s00170-020-05856-z;

  Public link: HAL Id: hal-02910327 https://hal.archives-ouvertes.fr/hal-02910327

A.2 Books chapters

- R. Mena, J.V. Aguado, S. Guinard, A. Huerta, Distortions in Large Aluminum Forgings: Current Situation and Simulation Challenges, in Computation and Big Data for Transport, P. Diez et al. (eds.), Springer Nature Switzerland AG (2020); https://doi.org/10.1007/978-3-030-37752-6_14;

  Public link: HAL Id: hal-02454596 https://hal.archives-ouvertes.fr/hal-02454596

A.3 Conference proceedings

- R. Mena, J.V. Aguado, S. Guinard, A. Huerta, Post-machining distortion mitigation via bending straightening, a multiparametric ROM study, ESAFORM2019 Conference, AIP Conference Proceedings 2113, 100009 (2019); https://doi.org/10.1063/1.5112642;

  Public link: HAL Id: hal-02454607 https://hal.archives-ouvertes.fr/hal-02454607

- R. Mena, J.V. Aguado, S. Guinard, A. Huerta, Reshaping of large aeronautical structural parts: A simplified simulation approach, ESAFORM2018 Conference, AIP Conference Proceedings 1960, 090001 (2018); https://doi.org/10.1063/1.5034927;

  Public link: HAL Id: hal-02454692 https://hal.archives-ouvertes.fr/hal-02454692

- R. Mena, D. Deloison, J.V. Aguado, A. Huerta, "Influence of the residual stresses in reshaping operations of large aeronautical parts", in International Conference on Adaptative Modeling and Simulation ADMOS 2017, edited by S. Perotto and P.Díez, eds., CIMNE, 2017;

  Public link: HAL Id: hal-02454746 https://hal.archives-ouvertes.fr/hal-02454746

A.4 Technical reports

- R. Mena, Reshaping operations at Airbus Operations Nantes, Technical report, Airbus SAS, Nantes (2018);

A.5 Outreach activities

- UPC finalist in the outreach contest *My Thesis in 4 minutes* (2019);

  Public link: https://www.youtube.com/watch?v=wzr2JE6PHqw